Multi physics design and optimization of flexible matrix composite (FMC) driveshafts

PENNSTATE

1855

ETH

Eidgenössische Technische Hochschule Zürich
Swiss Federal Institute of Technology Zurich

Master Thesis

Multi Physics Design and Optimization of Flexible Matrix Composite (FMC) Driveshafts

Christoph Roos

Advisors:

Prof. Dr. Charles E. Bakis

Composites Manufacturing Technology Center, Department of Engineering Science and Mechanics, Pennsylvania State University, USA

Prof. Dr. Edoardo Mazza

Center of Mechanics, Institute for Mechanical Systems, ETH Zurich, Switzerland

Dr. Gerald Kress

Centre of Structure Technologies, Institute for Mechanical Systems, ETH Zurich, Switzerland

Reference Number (ETH): 10-046

September 21, 2010

Abstract

A continuous trend in industrial design seeks for lighter and more efficient structures. To achieve that, new materials and structural designs need to be developed. Flexible matrix composites (FMCs) consist of low modulus elastomers such as polyurethanes which are reinforced with high-stiffness continuous fibers such as carbon. This fiber-resin system is more compliant compared to typical rigid matrix composites (RMCs) and hence allows for higher design flexibility. Continuous, single-piece FMC driveshafts can be used for helicopter applications. Not only a high torsional stiffness is required, to transmit power efficiently, but also a high compliance in bending to accommodate the inevitable driveline misalignment from airframe deflections and finite manufacturing tolerances. Such FMC shafts are envisioned to replace multi-segmented metallic shafts and maintenance-intensive, heavy flexible joints currently in use.

Among the main challenges in designing FMC driveshafts is to assure that the material does not overheat and that allowables are not exceeded. The challenge is that the analysis needs to address several physical processes such as self-heating in the presence of material damping, conduction and surface convection, ply-level stresses and strains, buckling and dynamic stability of a spinning shaft. Quasi-static and dynamic temperature- and frequency-dependent material properties for a carbon-polyurethane composite are embedded within the model.

An optimization tool using a genetic algorithm approach is developed to optimize layup stacking sequence, number of plies and number of mid-span bearings for a spinning, misaligned helicopter driveshaft to obtain a minimum-weight solution. For all calculations, MATLAB R2009b is employed. Two different helicopter designs are investigated, Blackhawk and Chinook. Weight savings of more than 23% for a Blackhawk driveline are obtained when compared to the current multi-segmented metallic design. For a Chinook driveline, almost 19% of weight can be reduced by using a one-piece FMC driveshaft. In order to gain more insight into designing driveshafts, various loadings scenarios are analyzed and the effect of misalignment of the shaft is investigated. It is the first time that a self-heating analysis of a driveshaft with frequency- and temperature-dependent material properties is incorporated within a design optimization model.

Key Words: flexible matrix composite, laminate, driveshaft, helicopter, optimization

Acknowledgments

This master thesis is part of the course for the Master of Science degree in Mechanical Engineering at the Swiss Federal Institute of Technology (ETH), Zurich, Switzerland. The project was carried out at the Pennsylvania State University (Penn State), University Park, Pennsylvania, United States of America, in 2010.

I wish to thank my advisor Prof. Dr. Charles E. Bakis at Penn State for making this project possible, our interesting discussions and his excellent guidance and assistance throughout the entire duration of this project.

Also, I would like to thank my advisors Prof. Dr. Edoardo Mazza and Dr. Gerald Kress at ETH Zurich for their support and commitment to this work.

Furthermore, Mr. Todd Henry and Mr. Ben Wimmer provided a very useful piece of work by manufacturing and testing filament-wound composite tubes. Also, I would like to acknowledge Dr. Ying Shan and Mr. Stanton Sollenberger for their valuable technical discussions and support. A special thanks goes to all the students and researchers at Penn State.

University Park, Pennsylvania, September 2010

Christoph Roos

Contents

List of Figures

List of Tables

Symbols

Indices

x	Global laminate coordinate in x-direction
y	Global laminate coordinate in y-direction
z	Global laminate coordinate in z-direction
1	Local laminae coordinate in fiber direction (in-plane)
2	Local laminae coordinate transverse to fiber direction (in-plane)
3	Local laminae coordinate in normal direction (out-of-plane)
θ	Fiber angle orientation with respect to axial x-direction
$\varepsilon_{11,c}$	Compressive strain in 1-direction
$\varepsilon_{11,t}$	Tensile strain in 1-direction
$\varepsilon_{22,c}$	Compressive strain in 2-direction
$\varepsilon_{22,t}$	Tensile strain in 2-direction
γ_{12}	Shear strain in 1-2 direction
ε_{max}	Maximum ply-level strain in driveshaft
$\sigma_{11,c}$	Compressive stress in 1-direction
$\sigma_{11,t}$	Tensile stress in 1-direction
$\sigma_{22,c}$	Compressive stress in 2-direction
$\sigma_{22,t}$	Tensile stress in 2-direction
τ_{12}	Shear stress in 1-2 direction
σ_{max}	Maximum ply-level stress in driveshaft
ϑ	Temperature
ϑ_S	Shaft temperature
ϑ_{ult}	Critical shaft temperature
f	Frequency
f_{crit}	Critical frequency of rotation
f_{op}	Frequency per minute at steady state operating conditions
T	Torque
$T_{B,crit}$	Critical buckling torque
T_{op}	Torque applied at steady state operating conditions
$S_{f,h}$	Safety factor for maximum temperature calculation due to self-heating
$S_{f,b}$	Safety factor for critical buckling torque calculation
$S_{f,w}$	Safety factor for critical speed calculation
$S_{f,s}$	Safety factor for stress and strain calculation

V_{fc}	Fiber volume content

Acronyms and Abbreviations

BC	Boundary Condition
CLT	Classical Lamination Theory
CTE	Coefficient of Thermal Expansion
DMA	Dynamic Mechanical Analyzer
FMC	Flexible Matrix Composite
GA	Genetic Algorithm
MoS	Margin of Safety
RMC	Rigid Matrix Composite
UD	Unidirectional

Chapter 1

Introduction

Helicopters are being employed in a wide range of applications from search and rescue to tourist attractions. A driveline is a crucial mechanical component in a rotary-wing aircraft. Depending on the aircraft design, it connects main and tail rotor or two main rotors. By inducing a torque at a certain angular velocity, power is transmitted from one end of the shaft to the other.

Current helicopter drivelines are realized by using multi-segmented aluminum shafts as shown in Figure 1.1. Flexible couplings are utilized to join the segments and accommodate for misalignments in the shaft due to aerodynamic loads on the tailboom. Intermediate bearings (mid-span bearings) ensure to support the driveshaft along its axial direction and keep the driveshaft in position. On the one hand, this design can account for misalignments and flexure of the tailboom due to aerodynamic loads. On the other hand, a rather heavy-weight and also service and maintenance intensive engineering design is obtained.

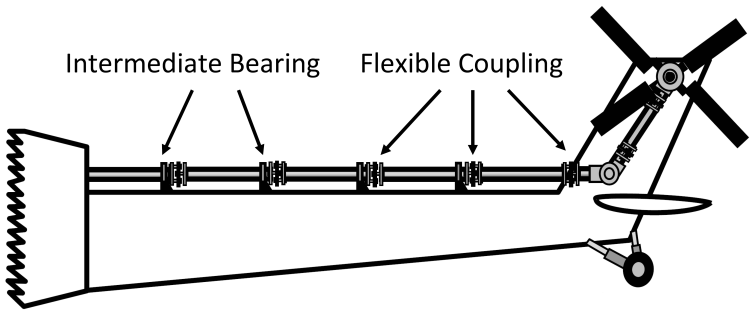

Figure 1.1: Metallic helicopter driveshaft design (Mayrides, 2005)

In order to improve these drawbacks a one-piece shaft with a minimum number of bearings is aimed at. A high flexural compliance and yet torsionally stiff structure is required. Not only is such a shaft able to account for misalignment in the driveline but also can power be transmitted efficiently. One big challenge when designing a one-piece driveshaft is heat generation within the shaft. A shaft misalignment as shown in Figure 1.2 not only induces a significant amount

of bending strain but also results in self-heating of an operating shaft. One can see that the composite material used has a huge impact on the actual shaft temperature. Generally, rigid matrix composites are flexural very stiff which results in a high shaft temperature. Flexible matrix composites, which can adapt better to a bent shape, show promising results in recent research activities carried out by Mayrides (2005), Shan and Bakis (2009), Sollenberger (2010). FMCs consist of low modulus elastomers, such as polyurethane, which are reinforced with high-stiffness continuous fibers, for instance carbon. Therefore, FMCs exhibit a high strength and stiffness in fiber direction and at the same they allow large strains in transverse direction to the fiber. Hence, this fiber-resin system is more compliant compared to typical rigid matrix composites and allows for more design flexibility.

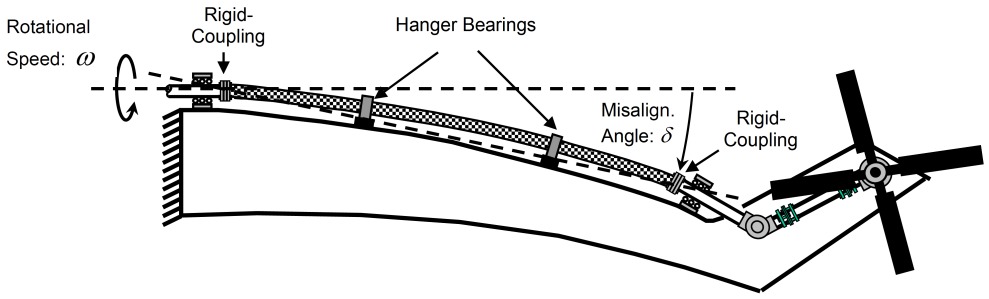

Figure 1.2: Misalignment in FMC driveshaft design (Mayrides (2005))

Also, there are two main philosophies with respect to shaft operating speed. Driveshafts can be operated either in a subcritical or supercritical range meaning that the operating speed is below or above the first natural frequency of the driveline. A supercritical design has one major advantage. Since the operating speed is higher, the same amount of power can be transmitted with a lower torque which allows for a lighter driveshaft design. Howsoever, in order to avoid vibrations, additional damping elements along the driveline are required which adds additional complexity and also weight to the system (Mayrides (2005)). In the following work, subcritical drivelines, as they are deployed in Blackhawk and Chinook helicopters, are considered only. As a result, the operating speed of the driveshaft needs to stay below its first natural frequency at all times.

This project aims at optimizing helicopter driveshafts with respect to weight using flexible matrix composites. The analysis needs to address several physical processes such as buckling, whirling, temperature, stress and strain constraints. Also, in order to minimize service and maintenance a minimum number of bearings is to be realized. Quasi-static and dynamic material properties are to be used in this work. A detailed project description is found in Section 2.7.

Chapter 2

Literature Review

2.1 FMC Materials

Flexible matrix composites are materials that consist of high stiffness and strength fibers embedded in a soft and flexible matrix which exhibits a high failure strain. Considering a UD reinforced FMC, the ratio of transverse moduli of elasticity can be up to 10^5 whereas this ratio is typically in the range between $10 - 10^2$ for RMC. Hence, this higher degree of anisotropy allows for more design flexibility and properties can be tailored to specific needs (Zindel (2009)).

Carbon fibers and glass fibers are commonly used for FMC materials and usually polyurethane or silicone forms the matrix system. Ultimate transverse tensile strain of FMCs can be 28% whereas rigid matrix composites usually exhibit a value of around 0.6% (Sollenberger (2010)). Having mentioned this, the compressive failure strain in FMCs can be as low as $900\mu\varepsilon$ (Sollenberger (2010)) whereas this value is typically in the range of $6000\mu\varepsilon$ for RMCs (MatWeb (2010)). This is due to the fact that the matrix system is fairly soft which results in less fiber support compared to a rigid matrix system.

A promising application for FMC materials are helicopter shafts where they need to adapt to a bent shape due to driveline misalignment. On the one hand, FMCs exhibit a higher loss factor than RMCs which would imply more internal damping and consequently also more self-heating. On the other hand, RMCs are much stiffer than FMCs and cannot adopt to a bent shape as nicely as FMCs shafts. It is shown in Shan and Bakis (2009) that the higher compliance of flexible matrix composites can compensate the higher loss factor. Internal heat generation is less in FMCs than in RMCs. Therefore, FMCs are superior to RMCs with respect to reducing self-heating and preventing overheating for a misaligned, spinning driveshaft.

2.2 Driveshaft Design

Most driveline designs are still realized by applying a metallic driveshaft. Many researchers have tried to replace a metallic driveshaft by a composite one in the last decades (Singh et al. (1997)). Early approaches in the 1970's attempted to replace a multi-segmented metal driveshaft with a multi-segmented rigid matrix composite. Zinberg and Symonds (1970) could report weight savings of around 28% by using a boron/ epoxy driveshaft. Herein, very simple models were applied to account for static and dynamic instabilities and strength. In subsequent work, carbon fiber reinforced composite were used to improve properties and more accurate models were incorporated by Lim and Darlow (1986), ter Wijlen and de Boer (1984) and many others. Most of the driveshafts are still designed to operate in the subcritical range. In ter Wijlen and de Boer (1984) a supercritical composite shaft was presented. A detailed review of the development of composite driveshaft designs from the 1970's to the late 1990's, including many references, can be found in Singh et al. (1997).

Flexible matrix composites were investigated by Hannibal et al. (1985) for bearingless rotor components and by Hannibal and Avila (1984) for an automobile driveshaft. Promising results were obtained and motivated to continue research in this area. In Hannibal et al. (1985), a full-scale tube was manufactured and tested statically and dynamically. No visual damage was observed during testing. They concluded that FMCs are viable candidates for driveshaft applications but also pointed out the need to further characterize these materials. In Shan (2006) and Sollenberger (2010), polyurethane-carbon FMCs tubes were characterized extensively.

Recent work from Mayrides (2005) showed weight savings of 29% (9 kg) and 26% (15.2 kg) for a Blackhawk and Chinook helicopter driveline, respectively, by utilizing a carbon-polyurethane composite material (T700/L100). The entire driveline was modeled using an FE approach. Buckling and a critical speed calculation were embedded within the model. A one-piece driveshaft design was realized which omits the need for flexible-joints as in current multi-segmented metallic shaft designs. A number of three and five mid-span bearings were reported to be sufficient for a Blackhawk and Chinook FMC driveshaft, respectively, whereas four and six are used in a current metallic design.

2.3 Critical Speed for Spinning Shaft

Zinberg and Symonds (1970) were among the first to investigate rotating anisotropic cylindrical driveshafts. Experimentally, the superior behavior of composite over aluminum alloy driveshaft was proven. This work was essential for shaft designing in the following decade or even decades and was often used as a foundation to validate critical speed models.

In Kim and Bert (1993) an analytical solution to calculate critical speed for

circular cylindrical hollow composite driveshaft with an arbitrary layup is presented. Sanders' best first approximation shell theory is used and can be reduced by tracers[1] to simpler shell theories such as Love's first approximation or Donnell's shell theories. Additionally, the more precise but also more complex Flügge's shell theory can be obtained, too. Centrifugal forces and Coriolis forces are included. The model was validated using existing data from literature and obtained results within engineering accuracy. Among the different thin-walled theories, Donnell's theory is not accurate for long shafts. Also, a very thin-walled driveshaft is assumed here so that the effects of transverse shear moduli on critical speed can be neglected. In Bert and Kim (1995c), the shortcoming of neglecting transverse shear moduli on whirling is eliminated. The model is extended by using a Bresse-Timoshenko beam. Thereby, bending-twisting coupling and transverse shear deformation are included in the critical speed analysis. The theory is capable of predicting the first natural frequency and is especially useful for rather short shafts where transverse shear deformation is important. In Bert and Kim (1995b), the whirling problem was taken one step further where the effect of fluctuating torque and/or fluctuating rotational speed on the critical speed was investigated. Fluctuations, however, have to be small compared to the torque applied to the shaft.

In dos Reis et al. (1987), a FE-model to predict critical speed of a thin-walled filament-wound composite shaft of any layup is presented. This work was based on experiments from Zinberg and Symonds (1970). The stiffness matrix was numerically determined by solving a two-point boundary value problem using Donnell's thin-shell theory. Results obtained showed that the layup greatly affects the shaft's dynamic behavior. Recently, more accurate models using finite element modeling have been developed by Gubrana and Guptab (2004), Chang et al. (2004) and Boukhalfa et al. (2008).

2.4 Buckling

Buckling has been investigated by many researches. A first model for a long solid shaft was developed in 1883 by Greenhill. However, it was not until 80 years later when the first models for anisotropic materials were developed by Dong et al. (1962) and Ambartsumyan (1964).

In Cheng and Ho (1963), a theoretical analysis for a heterogeneous anisotropic cylindrical shell under combined axial, pressure and torsional loading was developed. A thin-shell theory is assumed. Flügge's differential equations of equilibrium are used to solve the buckling problem. In Ho and Cheng (1963), this model was extended and the effect of boundary conditions was analyzed. Results agreed fairly well with theoretical calculations if the axial compression load is small.

In Bauchau et al. (1988), a torsional buckling model for a graphite-epoxy

[1]Tracers are coefficients in equations which have different values for different theories.

shaft was developed using a general shell theory. The model includes elastic coupling effects and transverse shearing deformations. Experiments showed good agreement with the model. Also, the significance of the layup stacking sequence was pointed out to be crucial to prevent torsional buckling.

In Bert and Kim (1995a), various shell theories such as Flügge's, Sanders', Love's first approximation and Donnell's theory, are considered and can be selected by tracers. These theories were validated by experiments and showed agreement within engineering accuracy. Also, it was shown that all theories considered therein, apart from one, showed a discrepancy of less than 2% considering a long tube. Donnell's theory is the only theory which overestimated buckling torques by 25% and should therefore not be used. Additionally, the effect of different boundary conditions on buckling torque was determined to be not higher than 5-3%. If in Bert and Kim (1995a), tracers of Flügge's differential equations are used, the same result as in Bert and Kim (1995a) is obtained.

In Kollár (1994), an analytical model which can determine the buckling shapes and loads for an anisotropic cylinder under temperature and/or mechanical loading is presented. Mechanical loads considered are axial load and torque. Since temperature loads are considered and the buckling shape is determined, a rather complex analytical model is obtained.

2.5 Material Model and Damping Model for a Bent, Spinning Shaft

In order to accommodate for misalignments, a one-piece shaft should be compliant in flexure to adopt well to the bent shape. FMCs shaft can be tailored by chosing an appropriate stacking sequence to fulfill this requirement. However, a shaft misalignment induces a cyclic bending strain in a spinning driveshaft. A FMC, consisting for instance of a polymer resin, shows a pronounced viscoelastic behavior. A high internal damping leads to a big amount of dissipated energy and internal heat generation which increases shaft temperature and can lead to overheating (Shan and Bakis (2009) and Hannibal and Avila (1984)). Also, a higher material temperature has a direct impact on the material properties. The higher the temperature, the lower the the elastic constants of the material. For instance, the E-modulus in 2-direction decreases with increasing temperature. A model to predict self-heating of a spinning, misaligned driveshaft is presented in Section 3.3.

In the following, the model of Shan and Bakis (2009) and Sollenberger (2010) used to predict internal damping of FMC laminates is presented, which lays the foundation of their self-heating model explained in Chapter 3. In the following subsections, a material model for an anisotropic viscoelastic composite material is presented.

Loss Factor η

One way to measure damping in harmonic vibration problems is to utilize the loss factor, η. Considering a viscoelastic behavior, a finite amount of energy is absorbed within each cycle (Shan and Bakis (2009)).

Assuming the applied strain and resultant stress to be (see Equation 2.1).

$$\varepsilon(t) \;=\; \varepsilon_a \cdot sin(\omega \cdot t) \qquad and \qquad \sigma(t) \;=\; \sigma_a \cdot sin(\omega \cdot t + \phi) \tag{2.1}$$

where ϕ, ω is the phase difference between strain and stress and angular frequency, respectively.

Considering the applied strain and resultant stress to be harmonic (see Equation 2.1), the loss factor, η, is given by Equation 2.2.

$$\eta \;=\; \frac{1}{2 \cdot \pi} \cdot \frac{\Delta W}{W} \;=\; tan(\phi) \tag{2.2}$$

where ΔW is the total dissipated energy during one stress cycle and W the maximum strain energy in this cycle which are given by Equations 2.3 and 2.4, respectively.

$$\Delta W \;=\; \oint \sigma(t) d\varepsilon(t) \;=\; \pi \cdot \sigma_a \cdot \varepsilon_a \cdot sin(\phi) \tag{2.3}$$

$$\begin{aligned} W \;&=\; \frac{1}{2} \cdot \varepsilon_{max} \cdot \sigma_{\varepsilon_{max}} \;=\; \frac{1}{2} \cdot \varepsilon_a \cdot sin(\frac{\pi}{2}) \cdot \sigma_a \cdot sin(\frac{\pi}{2} + \phi) \\ &=\; \frac{1}{2} \cdot \sigma_a \cdot \varepsilon_a \cdot cos(\phi) \end{aligned} \tag{2.4}$$

Fractional Derivative Standard Linear Model

A classical approach to model a viscoelastic material behavior is to use a standard linear model which gives the following relationship between stress σ and strain ε as shown in Equation 2.5.

$$\sigma(t) + a \cdot \frac{d\sigma(t)}{dt} = E \cdot \varepsilon(t) + b \cdot E \cdot \frac{d\varepsilon(t)}{dt} \tag{2.5}$$

where a is the retardation time, b is the creep relaxation time and E is the equilibrium modulus. If harmonic stress and strain application is assumed, Equation 2.5 reduces to Equation 2.6.

$$\sigma_0 = E \cdot \varepsilon_0 \cdot \frac{1 + i \cdot \omega \cdot b}{1 + i \cdot \omega \cdot a} = (E' + i \cdot E'') \cdot \varepsilon_0 \tag{2.6}$$

where E' is the storage modulus and E'' is the loss modulus.

However, this model is not used since it does not take the low frequency material properties into account well (Shan and Bakis, 2009). Also, the number of terms is to be reduced and a fractional derivative standard linear model (see Figure 2.1) is used instead. Now, Equation 2.5 appears in the following form as shown in Equation 2.7.

$$\sigma(t) + a \cdot D^{\beta} \cdot \sigma(t) = E \cdot \varepsilon(t) + b \cdot E \cdot D^{\beta} \cdot \varepsilon(t) \tag{2.7}$$

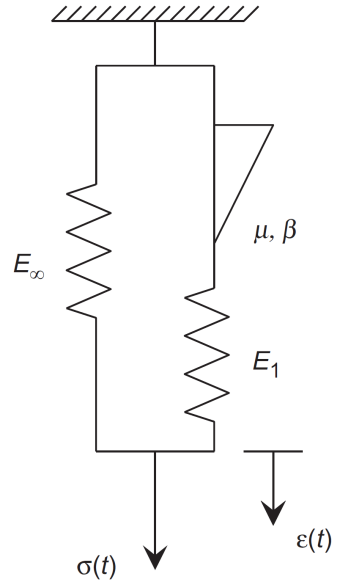

Figure 2.1: Rheological model of fractional derivative standard linear model - viscoelastic behavior (Shan and Bakis, 2009)

where $E = E_{\infty}$, $a = \frac{\mu}{E_1}$ and $b = \mu \cdot \frac{E_{\infty}+E_1}{E_{\infty} \cdot E_1}$

Compared to a classical standard linear model, the dashpot element is replaced by a so-called springpot element which is characterized by following stress-strain relationship $\sigma(t) = \mu \cdot D^{\beta} \cdot \varepsilon(t)$. This element shows a purely elastic behavior for $\beta = 0$ and a purely linear viscous behavior for $\beta = 1$ (Shan and Bakis, 2009).

A generalization of Equation 2.7 leads to Equation 2.8.

$$\sigma(t) + a \cdot \sum_{k=1}^{n} \alpha_k \cdot D^{\beta_k} \cdot \sigma(t) = E \cdot \varepsilon(t) + E \cdot \sum_{k=1}^{n} b_k \cdot D^{\beta_k} \cdot \varepsilon(t) \tag{2.8}$$

After some manipulations and assuming a harmonic response of stress $\sigma(t)$ and strain $\varepsilon(t)$, following formula for storage and loss moduli are obtained (see Equation 2.9).

$$\begin{aligned} E' &= Re\left\{\frac{1+\sum_{k=1}^{n} b_k(i\cdot\omega)^{\beta_k}}{1+\sum_{k=1}^{n} a_k(i\cdot\omega)^{\beta_k}}\right\}\cdot E \\ E'' &= Im\left\{\frac{1+\sum_{k=1}^{n} b_k(i\cdot\omega)^{\beta_k}}{1+\sum_{k=1}^{n} a_k(i\cdot\omega)^{\beta_k}}\right\}\cdot E \end{aligned} \tag{2.9}$$

By a fitting procedure of Equation 2.9 to experimental data, material parameters a_k, b_k, β_k and E can be determined. On the one hand, E_{11} is fiber dominated and assumed to be independent of temperature and frequency. Also, the Poisson's rations ν_{12} and ν_{23} are considered to be constant. On the other hand, matrix dominated material properties E_{22} and G_{12} are modeled using the fractional derivative model (Shan and Bakis, 2009). The rest of the lamina material properties are obtained by assuming a transverse isotropy in the 23-plane direction.

Lamina Material Properties

Applying the fractional derivative model, presented above, and assuming a harmonic stress and strain behavior, following storage and loss moduli are determined (see Equation 2.10).

$$E' = \frac{A\cdot C + B\cdot D}{C^2+D^2}\cdot E \qquad and \qquad E'' = \frac{B\cdot C + A\cdot D}{C^2+D^2}\cdot E \tag{2.10}$$

The coefficients A, B, C and D are shown in Equation 2.12. By applying Equation 2.2, the loss factor, η, is then given by Equation 2.11.

$$\eta = tan(\phi) \stackrel{!}{=} \frac{E''}{E'} \tag{2.11}$$

$$\begin{aligned} A &= 1 + b_1\cdot f^{\beta_1}\cdot cos(\frac{\pi\cdot\beta_1}{2}) + b_2\cdot f^{\beta_2}\cdot cos(\frac{\pi\cdot\beta_2}{2}) + ... + b_n\cdot f^{\beta_n}\cdot cos(\frac{\pi\cdot\beta_n}{2}) \\ B &= b_1\cdot f^{\beta_1}\cdot sin(\frac{\pi\cdot\beta_1}{2}) + b_2\cdot f^{\beta_2}\cdot sin(\frac{\pi\cdot\beta_2}{2}) + ... + b_n\cdot f^{\beta_n}\cdot sin(\frac{\pi\cdot\beta_n}{2}) \\ C &= 1 + a_1\cdot f^{\beta_1}\cdot cos(\frac{\pi\cdot\beta_1}{2}) + a_2\cdot f^{\beta_2}\cdot cos(\frac{\pi\cdot\beta_2}{2}) + ... + a_n\cdot f^{\beta_n}\cdot cos(\frac{\pi\cdot\beta_n}{2}) \\ D &= a_1\cdot f^{\beta_1}\cdot sin(\frac{\pi\cdot\beta_1}{2}) + a_2\cdot f^{\beta_2}\cdot sin(\frac{\pi\cdot\beta_2}{2}) + ... + a_n\cdot f^{\beta_n}\cdot sin(\frac{\pi\cdot\beta_n}{2}) \end{aligned} \tag{2.12}$$

where E, a_n, b_n and β_n are material constants which need to be determined by fitting E', E'' and η to experimental data over the frequency range of interest.

By applying the temperature-frequency superposition principle of Ferry (1970), the temperature dependence is embedded in the model. The Williams-Landel-Ferry (WLF) equation is used which is given by Equation 2.13.

$$log\,(\alpha_\vartheta) \;=\; \frac{C_1 \cdot (\vartheta - \vartheta_0)}{C_2 + \vartheta - \vartheta_0} \tag{2.13}$$

where α_ϑ, ϑ, ϑ_0, C_1 and C_2 are temperature shift function, temperature, reference temperature and material constants, respectively. The material constants C_1 and C_2 are to be determined from experiments.

This model is now able to predict temperature and frequency dependent dynamic lamina material properties of E[2].

Damping Model

The fractional derivative model is combined with the maximum strain energy approach to predict damping in a composite laminate based on lamina material properties.

Applying Equation 2.2, the loss factor, η, is given by Equation 2.14.

$$\eta \;=\; \frac{1}{2\pi}\frac{\Delta W}{W} \;=\; \frac{1}{2\pi}\frac{\sum\limits_k \Delta W^{(k)}}{\sum\limits_k W^{(k)}} \tag{2.14}$$

where the coefficient k indicates the dissipated energy and total strain energy, respectively, of the k^{th} ply. $\Delta W^{(k)}$ and $W^{(k)}$ are given by Equations 2.15 and 2.16.

$$\Delta W^{(k)} \;=\; \pi \cdot \eta_{ij}^{(k)} \cdot W_{ij}^{(k)} \tag{2.15}$$

$$W^{(k)} \;=\; \frac{1}{2} \cdot \sigma_{ij}^{(k)} \cdot \varepsilon_{ij}^{(k)} \tag{2.16}$$

In the principal ply-coordinates, Equations 2.15 and 2.16 become to Equations 2.17 and 2.18 if a linear elastic ply behavior is assumed.

$$\begin{aligned}\Delta W^{(k)} \;= \pi \cdot \int_V (&\eta_{11}^{(k)} \cdot \sigma_{11}^{(k)} \cdot \varepsilon_{11}^{(k)} + \eta_{22}^{(k)} \cdot \sigma_{22}^{(k)} \cdot \varepsilon_{22}^{(k)} + \eta_{33}^{(k)} \cdot \sigma_{33}^{(k)} \cdot \varepsilon_{33}^{(k)} \\ &+ \eta_{12}^{(k)} \cdot \tau_{12}^{(k)} \cdot \gamma_{12}^{(k)})\; dV\end{aligned} \tag{2.17}$$

[2] E represents any moduli that is to be modeled by using the fractional derivative model, for instance E_{22} or G_{12}

$$W^{(k)} = \frac{1}{2} \cdot \int_V (\sigma_{11}^{(k)} \cdot \varepsilon_{11}^{(k)} + \sigma_{22}^{(k)} \cdot \varepsilon_{22}^{(k)} + \sigma_{33}^{(k)} \cdot \varepsilon_{33}^{(k)} + \tau_{12}^{(k)} \cdot \gamma_{12}^{(k)})\ dV \tag{2.18}$$

For the stress and strain calculation for an multi-directional laminated orthotropic tube subjected to a bending moment, an approach by Jolicoeur and Cardou (1994) is used which is presented in Section 3.4.

To sum up, the fractional derivative model of Shan and Bakis (2009) is used to calculate frequency- and temperature-dependent lamina properties. After calculating lamina stresses and strains by using the model of Jolicoeur and Cardou (1994), a strain energy method is used to model the overall tube axial damping (Shan and Bakis (2009)).

2.6 Limitations of Previous Work

On the one hand, buckling, strength and critical speed requirements are among the most basic requirements for designing a driveshaft and are extensively discussed in literature. On the other hand, self-heating of driveshafts using frequency- and temperature-dependent material properties is a crucial and not a straightforward design requirement for composites. Due to its complexity, this requirement has always been neglected in analysis in research work before 2009. Shan and Bakis (2009) have presented this as a new theory and verified their calculations with experiments. However, no shaft design work has been done yet using this self-heating model.

It is also to be noted that in past work on shafts, mainly quasi-static material properties have been used for design purposes. The temperature- and frequency-dependent behavior is neglected. A large amount of experiments are to be carried out in order to characterize a composite material system statically and dynamically. This is not only time consuming but also very costly.

In Mayrides (2005), a model to find an optimum composite driveshaft design has been developed by considering buckling, critical speed and material strength. However, a maximum of three different fiber angle orientations could be varied during the optimization of the driveshaft. Also, quasi-static material properties have been used. Additionally, it has been shown by Y. Shan (unpublished research work at Pennsylvania State University, USA) that the critical speed calculation which was used by Mayrides (2005) is not accurate. Mayrides' whirling model overestimates critical speed by a factor of two or more compared to the reference of his model.

No model has been developed, to the author's knowledge, so far which incorporates temperature- and frequency-dependent dynamic material properties and a self-heating to design a minimum-weight driveline for a helicopter application.

2.7 Problem Statement

The aim of this investigation is to develop a multi physics structural model and optimization tool for a carbon-polyurethane composite one-piece driveshaft which incorporates following characteristics.

Among the main challenges in designing FMC shafts is to assure that the material does not overheat and that material allowables are not exceeded. The structural model should incorporate several physical processes. First, a self-heating calculation in the presence of material damping is to be executed. Also, ply-level stresses and strains have to be calculated. Additionally, a buckling torque calculation needs to be incorporated to prevent a structural instability. To avoid whirling, the critical speed for a spinning shaft should be calculated and embedded within the model. Thereby, dynamic temperature- and frequency-dependent material properties for a carbon-polyurethane composite are to be used which are available from previous work at Penn State.

Constraints such as upper temperature limit of the material, strength and strain allowables have to be considered which should be selected based on experimental data. The driveshaft is to be operated subcritically. Consequently, the first natural frequency needs to be higher than the operating speed.

Based on these requirements, a driveshaft optimization tool is to be developed which is capable of finding a minimum-weight driveline design. Herein, the number of plies, the stacking sequence and the number of mid-span bearings should be the design variables. Manufacturing constraints for filament-wound driveshaft are to be considered. More insight into driveshaft designs can be gained by varying applied torque, operating speed and misalignment of the shaft.

Analytical solutions should be used within the structural model. Both, the structural and optimization model are to be implemented in MATLAB (R2009b).

Chapter 3

Structural Model of Driveshaft

3.1 Overview

Filament-wound tubes are economically manufactured in a helical shape. Instead of obtaining a separate $+\theta$ and $-\theta$ fiber angle orientated layer, the outcome of this is one $[\pm\theta]$ orientated layer. A crossover of fiber tows is inevitable which leads to fiber undulation. This leads to a different mechanical behavior of helically-wound and UD-layered tubes. A lot of work was carried out in past research activities to capture the effect of fiber undulation, waviness, respectively and its effect on material properties (Hsiao and Daniel (1996), Bogetti et al. (1992), Pansart et al. (2009), Stecenko and Piggott (1997), Zindel (2009) and Zhang et al. (2008)). However, no analytical model exists to the author's knowledge which is capable of predicting that effect for a multi-layered laminate and a general loading case in good agreement with experiments.

The multi physics structural model to design a driveshaft is presented which will be referred to as *structural model* in this work. It exhibits following characteristics.

- Quasi-static and dynamic temperature- and frequency material properties for carbon fiber reinforced polyurethane matrix composite based on experiments (see Section 3.2)
- Stress and strain calculation for an orthotropic tube (see Section 3.4)
- Self-heating of a misaligned and spinning shaft for a multi-directional laminate (see Section 3.3)
- Buckling of a driveshaft (see Section 3.6)
- Cricital speed calculation for a subcritically spinning driveshaft (see Section 3.5)

Analytical solutions are employed. This enables to obtain a low computation time which is of highest importance for optimization (see Chapter 4).

In Figure 3.1, a flow chart of the structural model is shown. First, the driveshaft temperature ϑ_S is determined by executing the self-heating model for a spinning misaligned driveshaft. Material properties at the shaft temperature ϑ_S and frequency f_{op} are calculated. These properties are used within the stress and strain calculation, buckling and critical speed calculations.

Inputs to the structural model are shown in Table 3.1. The stacking sequence in the structural model starts from the inner radius of the shaft which implies that the numbering of the layers starts at the inner radius r_i.

Table 3.1: Inputs to Structural Model

Inputs:		
Geometry	fiber angle orientation:	θ_1, θ_2, ..., θ_k
	stacking sequence:	(θ_1/-θ_1/θ_2/-θ_2/.../θ_k/-θ_k)
	ply thickness:	t_i
	outer radius:	r_o
	shaft length:	L
	number of bearings:	n_b
Material Properties	elastic constants:	see Table 3.3
	material density:	ρ
	material allowables:	$\varepsilon_{11,c,crit}$, $\varepsilon_{11,t,crit}$, $\varepsilon_{22,t,crit}$, $\varepsilon_{22,c,crit}$, $\gamma_{12,crit}$, $\sigma_{11,c}$, $\sigma_{11,t}$, $\sigma_{22,t}$, $\sigma_{22,c}$, τ_{12}, ϑ_{crit}, $T_{B,crit}$, f_{op} (, $\alpha_{x,crit}$)
Loads	torque:	T
	strain due to misalignment:	ε_{max}

The outputs of the structural model are: temperature ϑ_S, compressive strain in 1-direction $\varepsilon_{11,c}$, tensile strain in 1-direction $\varepsilon_{11,t}$, tensile strain in 2-direction $\varepsilon_{22,t}$, compressive strain in 2-direction $\varepsilon_{22,c}$, shear strain in 1-2 direction γ_{12}, compressive stress in 1-direction $\sigma_{11,c}$, tensile stress in 1-direction $\sigma_{11,t}$, tensile stress in 2-direction $\sigma_{22,t}$, compressive stress in 2-direction $\sigma_{22,c}$, shear stress in 1-2 direction τ_{12}, buckling torque T_B, critical speed f_{crit} (CTE in x-direction α_x, not shown in Figure 3.1).

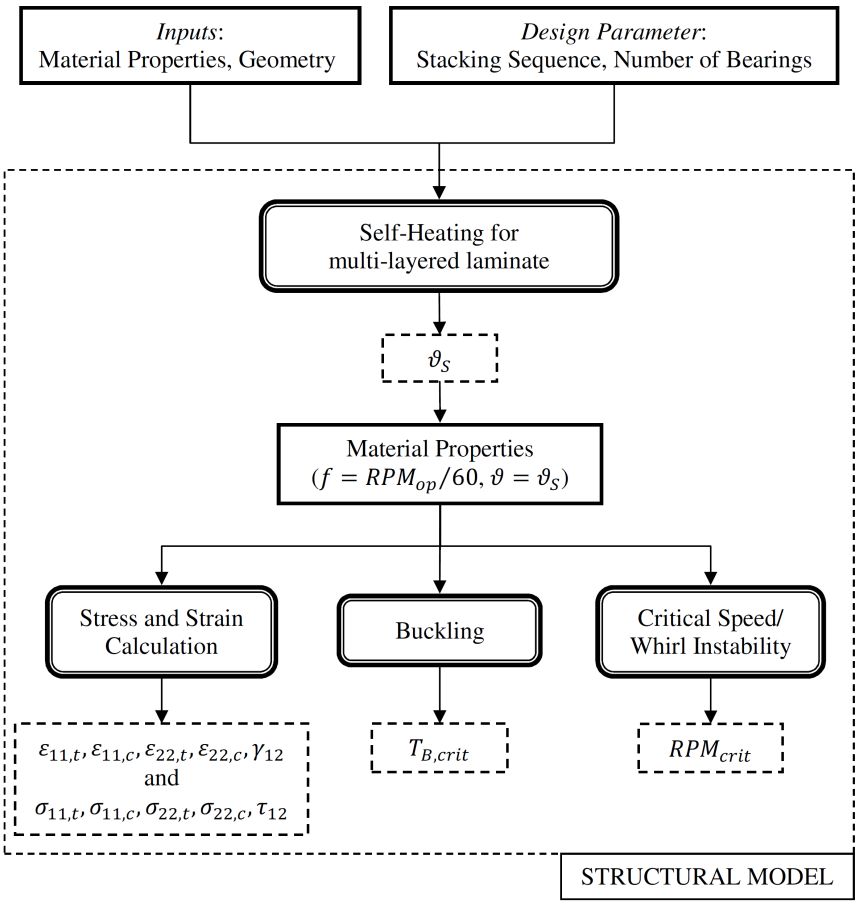

Figure 3.1: Structural Model of FMC driveshaft (Matlab)

3.2 Material Properties

By definition, FMC materials are more complaint than RMCs. Therefore, they show a higher nonlinear material behavior and exhibit different material characteristics. Looking at filament-wound FMC tubes, another challenge arises when predicting stiffness properties. The influence of fiber undulation seems to have a significant impact on these properties. As mentioned in the previous section, no simple analytical model is available and this effect is not considered within the modeling. For this reason, [+θ/-θ]-layers have to be utilized to model a helically-wound shaft in the current investigation. Although, the effect of fiber undulation/crossing is not modeled, it is embedded within the model indirectly to a certain extend by using experimental material properties from helically wound tubes (see Subsections 3.2.2 and 3.2.3).

Zindel (2009) has made an attempt to predict elastic properties for a thin filament-wound shaft by developing a nonlinear model which accounts for fiber undulations. Unfortunately, results from analysis did not match the experimental

results as well as one would prefer for design purposes.

A carbon fiber reinforced polyurethane matrix composite is used in the following investigation. HexTow® AS4D 12k carbon fibers are utilized (Hexcel (2010)). The polyurethane matrix is obtained by mixing liquid polyether pre-polymer Adiprene® LF750D and a pre-polymer Caytur® 31 DA curative, both from Chemtura Corporation (Chemtura (2010)). The mass mixing ratio is 100 : 50.3. After heating the mixture for two hours at 140°C, a 16 hours post-curing cycle at 100°C is executed (Sollenberger (2010)). In this work, this carbon fiber reinforced polyurethane composite is referred to as LF750D/ASD4.

3.2.1 Assumptions and Limitations

- Linear viscoelastic material behavior (see Section 2.5).
- Laminae are transversely isotropic in 23-plane direction.
- Since DMA experiments were carried out between room temperature (23°C) and 100°C. Therefore, the material model is limited to a maximum temperature of around 100°C. It can also be observed that the material is significantly softer at 100°C, which is why it should not be exceeded.

3.2.2 (Quasi-)static material properties

Quasi-static lamina properties are determined based on experimental data for angle-ply laminates. Experiments for 10°- and 15°- tubes were carried out by T. Henry and B. Wimmer at Penn State[1]. The data for 20°-, 30°-, 45°-, 60°- and 88°-tubes are obtained from Sollenberger (2010).

A summary of the quasi-static lamina material properties and how they were calculated is shown in Table 3.2.

It can be shown that Equation 3.1 is true when applying CLT (Daniel and Ishai (2006)).

$$\begin{aligned} G_{12} &= \frac{\tau_{12}(\theta = \pm 45°)}{\gamma_{12}(\theta = \pm 45°)} \stackrel{!}{=} \frac{\sigma(\theta = \pm 45°)/2}{\varepsilon_x(\theta = \pm 45°) - \varepsilon_y(\theta = \pm 45°)} \\ &= \frac{\sigma(\theta = \pm 45°)}{2} \cdot \frac{1}{\varepsilon_x(\theta = \pm 45°)(1 + \nu_{xy}(\theta = \pm 45°))} \\ &= \frac{E_{xx}(\theta = \pm 45°)}{2 \cdot \varepsilon_x(\theta = \pm 45°)(1 + \nu_{xy}(\theta = \pm 45°))} \end{aligned} \tag{3.1}$$

where $\nu_{xy}(\theta = \pm 45°)$ is the Poisson's ratio which is obtained experimentally and determined to be 0.884 (Sollenberger (2010)).

[1] Results are not published yet.

Table 3.2: Quasi-static lamina properties of LF750D/AS4D

Properties		Calculation Method
E_{11}	119 GPa	Estimation, based on quasi-static compression experiments of $[\pm 10°]_2$-tube using inverse CLT
E_{22} $(=E_{33})$	1.64 GPa	Average value of quasi-static compression and tension experiments of for $[\pm 88°]_2$-tube
G_{12} $(=G_{13})$	1.08 GPa	CLT based on quasi-static tension experiments of $[\pm 45°]_2$-tube according to Equation 3.1
G_{23}	0.439 GPa	Calculated according to Equation 3.3
ν_{12} $(=\nu_{13})$	0.33	Rule of mixture
ν_{23}	0.87	Using empirical interpolation function (see Sollenberger (2010))

In Figure 3.2[2][3], experimental results for quasi-static tension and compression test for angle-ply laminates are presented.

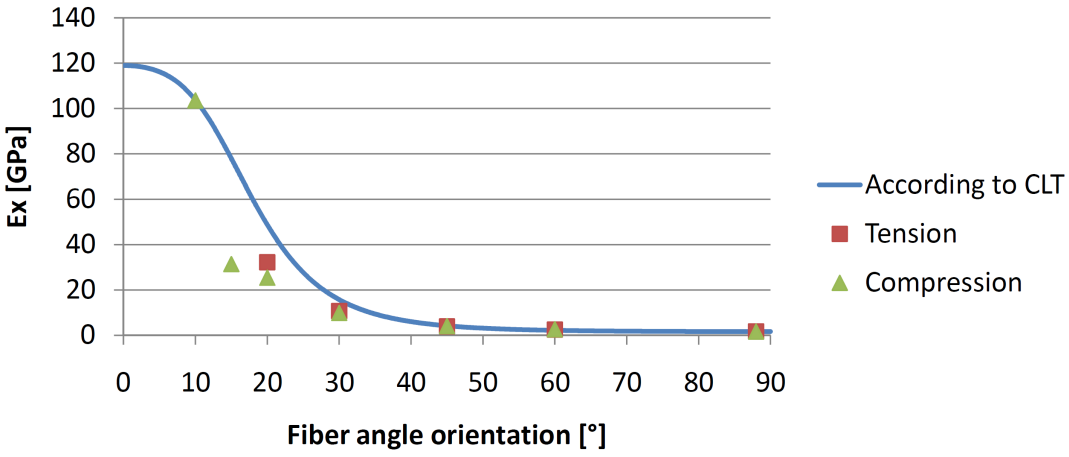

Figure 3.2: Quasi-static axial modulus E_{xx} and E_{11} using CLT for LF750D/AS4D

The prediction of the axial modulus E_{xx} by applying CLT and using the lamina material properties shown in Table 3.2 deviate as much as 60% for a 15°-tube compared to experimental data. The origin of this deviation between CLT and experimental data for some fiber orientations is not fully understood and is subject to further work (see Section 6.2). It has been stated by Shan (2006) and

[2]No experimental data for quasi-static tensile tests for a 10° and 15° angle-ply is available at this point of time

[3]The axial modulus E_{xx} is the secant modulus measured between 0 and 500 $\mu\epsilon$.

Sollenberger (2010) that CLT might not be capable of predicting elastic constants, such as E_{xx}, accurately for FMCs. Also, the effect of fiber undulation might be too important to be neglected. Last but not least, manufacturing issues could also be partly responsible for the big variation of E_{xx} for low fiber angle orientations since filament-winding becomes more challenging for fiber angle orienations as low as 10° and 15°.

3.2.3 Dynamic material properties

Data of dynamic material properties was obtained by performing DMA-spin tests of laminated tubes. Lamina material properties were obtained by fitting the data to the linear viscoelastic constitutive model presented in Section 2.5. DMA tests were carried out at 500 $\mu\epsilon$. The detailed test set-up is presented in Sollenberger (2010).

The E-modulus in 1-direction is assumed independent of frequency and temperature and its quasi-static value of E_{11}=119 GPa is used. Also, Poisson's ratio $\nu_{12} = \nu_{13} = 0.33$ and $\nu_{23} = 0.87$ are assumed independent of temperature and frequency and are determined using rule of mixture. Lamina material properties E_{22} and G_{12} are calculated using the viscoelastic material model presented in Section 2.5. The material constants shown in Table 3.3[4] are fitted to experimental data. The frequency to be used in Equation 2.12 is the reduced frequency $f_{\alpha_T} = \alpha_\vartheta \cdot f$ which takes temperature dependence into account (see Equation 2.13). The storage modulus, loss modulus and loss factor obtained are temperature- and frequency-dependent.

[4] E_{11}=79 GPa was used by Sollenberger (2010) since no experimental data for 10° and 15° helically-wound tubes were available at the time of his work.

Table 3.3: Dynamic material properties of LF750D / AS4D (Sollenberger (2010))

Properties:			
Longitudinal:	E_1	=	110 GPa
	η_1	=	0.0015
Transverse:	E	=	0.2148 GPa
	a_1	=	0.2120
	b_1	=	4.9357
	β_1	=	0.2275
	a_2	=	$6.0 \cdot 10^{-5}$
	b_2	=	0.0039
	β_2	=	0.8106
	C_1	=	-4.802
	C_2	=	126.5
Shear:	G	=	0.1571 GPa
	a_1	=	2.8878
	b_1	=	0.0230
	β_1	=	$2.0 \cdot 10^{-11}$
	a_2	=	0.5170
	b_2	=	4.6893
	β_2	=	0.2433
	C_1	=	-24.46
	C_2	=	264.1
Poisson Ratio:	ν_{12}	=	0.33
	ν_{23}	=	0.87

A transverse isotropic material behavior in the 23-plane direction is assumed. Lamina elastic constants $E_{22} = E_{33} = E'_{22} = fcn(f_{\alpha_\vartheta}, \vartheta_S)$, $G_{12} = G_{13} = G'_{12} = fcn(f_{\alpha_\vartheta}, \vartheta_S)$ can be determined for a given temperature and frequency. The Poisson's ratio ν_{21} is calculated according to Equation 3.2 by applying CLT.

$$\nu_{21} = E_{22} \cdot \frac{\nu_{12}}{E_{11}} \tag{3.2}$$

Shear modulus G_{23} can be determined by Equation 3.3.

$$G_{23} = \frac{E_{22}}{2 \cdot (1 + \nu_{23})} \tag{3.3}$$

These dynamic lamina material properties are employed in the structural model for all calculations that are carried out.

3.3 Self-Heating Model for a Spinning, Misaligned Driveshaft

3.3.1 Assumptions

Following assumptions are made in the self-heating calculation model.

- All strain energy loss (dissipated energy) which is caused by internal damping is converted into heat.
- There is no coupling between the temperature and elastic fields.
- Laminated orthotropic, viscoelastic material behavior.
- Laminae are assumed to be transversally isotropic in the 23-plane.
- The shaft is subjected to cyclic pure bending loads where flexural strain is uniformly distributed along the length of the shaft.
- Torque is assumed constant and to have no influence on heating.
- Shear stress $\tau_{r\theta}$ is neglected within the heat-generation calculation for simplicity.
- A one-dimensional heat transfer problem in radial direction is assumed. Heat transfer along length is neglected.
- The inner surface of the shaft is insulated and the outer surface convective and radiative heat transfer occurs.
- A Reynolds number of $Re > 10^3$ is assumed.

3.3.2 Modeling

A self-heating model for a spinning misaligned driveshaft is developed by Shan and Bakis (2009) which is valid for angle-ply laminates. A homogenized tube was assumed. Therein, the model by Sun and Li (1988)[5] is used to predict 3D effective elastic constants for a thick-walled tube. In Sollenberger (2010), this model is generalized to multi-layered laminates[6].

[5]It is to be noted that a very similar model was already presented by Kress (1985) and Kress (1986), respectively.

[6]In Sollenberger (2010), it is documented that the model of Sun and Li (1988) is used to calculate the elastic constants C_{ij} . This is not true. He actually used general Hooke's law. This is important to mention since the model of Sun and Li (1988) can, strictly, only be applied to thick flat laminates. If applied to thick-walled tubes, a numerical error is introduced since the physics in not right anymore. Consequently, the model of Sun and Li (1988) should not be used for thick-walled laminated tubes

The shaft is subject to a bending strain of $1500\mu\varepsilon$ which is due to misalignment in the shaft. This value was used by Sollenberger (2010) in recent work on driveshafts and is assumed to be a realistic value for practical helicopter applications.

Mayrides (2005) (see Figure 3.3) calculated the ambient shaft temperature for two extreme scenarios whereas he based his calculation on Ocalan (2002). First, the helicopter is in operation where radiation from and to the tailboom from the atmosphere is assumed and forced convention due to rotor down-wash. A steady state temperature of 44°C was determined. Second, a parking case is assumed and free convection instead of force convection is applied. The steady state temperature is 89°C (see Mayrides (2005) and Ocalan (2002)). For this work, an ambient temperature in between these two extreme cases is assumed and determined to be 60°C.

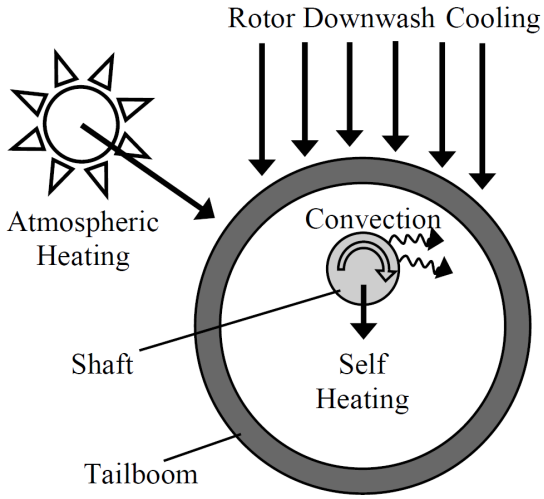

Figure 3.3: Heating model by Mayrides (2005)

Using the damping model which is explained in Section 2.5, the finite difference thermal model is applied to predict equilibrium temperature in a rotating, misaligned orthotropic FMC shaft. In the following, the finite difference thermal model is presented (Shan and Bakis (2009)).

The wall thickness in radial direction is divided into $n+1$ nodes with equal distance $\Delta r = \frac{b-a}{n}$ where a and b are the inner and outer radius, respectively, and n is the number of nodes(see Figure 3.4. The number of nodes has to be selected so that the same number of nodes falls in each ply.

The approach by Jolicoeur and Cardou (1994) is used to calculate laminate stress and strain distribution in a multi-layered laminate for a tube subjected to a bending moment.

The thermal energy generated per unit volume per unit time at each nodal point is expressed by Equation 3.4.

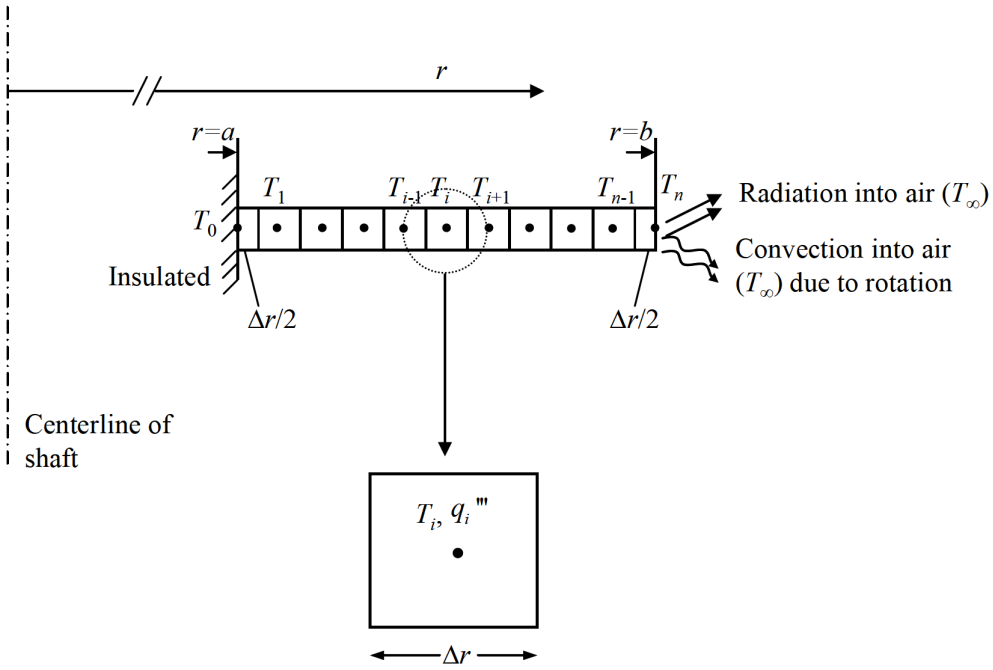

Figure 3.4: Thermal model for shaft self-heating (Shan and Bakis (2009))

$$q''' = \frac{\omega}{2 \cdot \pi} \cdot \Delta W \tag{3.4}$$

where ω is the circular shaft frequency and ΔW is given by Equation 2.3.

According to a 1D heat transfer problem, the heat balance expression at the i^{th} node is given by Equation 3.5.

$$q_{i+1 \to i} + q_{i-1 \to i} + q_i^g = 0 \tag{3.5}$$

where $q_{i \to j}$ is the rate of heat transfer from nodal point i to j and q_i^g the rate of heat generated at i^{th} node. Equation 3.4 can be written in a finite difference form (see Equation 3.6).

$$r_{i+1} \cdot k \cdot \frac{T_{i+1} - T_i}{\Delta r} + r_{i-1} \cdot k \cdot \frac{T_{i-1} - T_i}{\Delta r} + r_i \cdot q_i''' \cdot \Delta r = 0 \tag{3.6}$$

where $k = 0.72 W m^{-1} K{-}1$ is the radial thermal conductivity of the composite laminate which is assumed independent of temperature. T_i and r_i are the temperature and radius at the i^{th} node, respectively.

In a steady state condition, the air temperature is the same as at the inner shaft surface. For this reason, the inner surface (i=0) is assumed to be insulated

which can expressed by Equation 3.7 and in a finite difference form according to Equation 3.8.

$$q_{1\to 0} + q_0^g \;=\; 0 \tag{3.7}$$

$$r_1 \cdot k \cdot \frac{T_1 - T_0}{\Delta r} + q_i''' \cdot a \cdot \frac{\Delta r}{2} \;=\; 0 \tag{3.8}$$

At the outer shaft surface (i_n), convective and radiative heat transfer occurs and is given by Equation 3.9 and in a finite difference form according to Equation 3.10.

$$q_{n-1\to n} + q_{\infty\to n} + q_n^g \;=\; 0 \tag{3.9}$$

$$r_{n-1} \cdot k \cdot \frac{T_{n-1} - T_n}{\Delta r} + h_c \cdot b \cdot (T_\infty - T_n) + \varepsilon \cdot \sigma \cdot b \cdot (T_\infty^4 - T_n^4) + q_n''' \cdot b \cdot \frac{\Delta r}{2} \;=\; 0 \tag{3.10}$$

where $q_{\infty\to n}$ is the rate of heat transfer from ambient air into n^{th} node due to convection and radiation. T_∞ is the ambient air temperature and h_c the effective convection heat transfer coefficient and is given by Equation 3.11. ε is the emissivity of the surface and $\sigma = 5.66961 \cdot 10^{-8} W m^{-2} K^{-4}$ is the Stefan-Boltzman constant.

$$h_c = k_a \cdot \frac{Nu}{2b} \tag{3.11}$$

where $k_a = 0.0251 W m^{-1} K^{-1}$ is the thermal conductivity of air at 20°C. $Nu = 0.533 \cdot Re^{1/2}$ is the average Nusselt number where $Re = (2 \cdot b)^2 \cdot \frac{\omega}{2 \cdot \nu}$ is the Reynolds number. $\nu = 1.57 \cdot 10^{-5} m^2 s{-}1$ is the kinematic viscosity of air at 20°C.

By rearranging Equations 3.6 and 3.8, a closed form expression for temperatures at nodal point 0 through n-1 is obtained, $T_0 = fcn(T_1, q_0''')$ and $T_i = fcn(T_{i+1}, T_{i-1}, q_i''')$. Similarly, a closed form expression for the equilibrium temperature at the surface can be obtained, $T_n = fcn(T_{n-1}, T_\infty, q_n''')$.

To sum up, frequency-dependent lamina material properties, stacking sequence, shaft geometry, rotational speed and bending strain are inputs to the thermal model. Since the lamina properties are also temperature-dependent, an iterative approach is to be used to solve for equilibrium shaft temperature.

The main coding of the self-heating model has been carried out by Y. Shan and S. Sollenberger. An additional measure to improve speed is implemented by the author which improves computation time of the MATLAB code significantly

(up to a factor of four). This can be achieved by predicting the shaft temperature more accurately so that less iterations are required until a steady state temperature is reached. Additionally, the discretization in the code of the finite difference model is generalized. In order to minimize computation time, a minimum number of elements in radial direction may be used which leads to a trade-off between accuracy and speed.

In the following validation subsection, not only the self-heating coding within the structural model is verified. Additionally, a study on discretization, number of elements through the thickness direction, is presented.

3.3.3 Validation

The structural model which calculates self-heating of a multi-layered anisotropic spinning FMC driveshaft was verified by comparing results to Sollenberger (2010). Results match perfectly and are not shown here. An experimental validation and FE-verification of the self-heating model is presented in Sollenberger (2010).

Computation time directly correlates with the number of elements through the wall thickness. In order to reduce computation time, the number of elements needs to be reduced, too. This, however, influences the discretization of the model and might decrease the capability of predicting accurate shaft temperatures. A trade-off between computation time and accuracy of shaft temperature prediction is to be expected.

In Figure 3.5, a driveshaft with four layers and a stacking sequence of [60/-60/45/-45] is used. On the horizontal axis, the number of iterations within the structural model to calculated maximum shaft temperature is shown. The maximum temperature within the shaft is shown on the vertical axis. The blue bar represents a driveshaft with 40 elements through the wall thickness, the red bar, 20 elements and the green bar a driveshaft with just four elements which results is one element per layer. All three cases converge after 14 iterations. On the one hand, the final shaft temperature discrepancy for these three discretization cases is less than 0.1%. On the other hand, computation time increase by a factor of more than 75 by increasing the number of elements from four to 40.

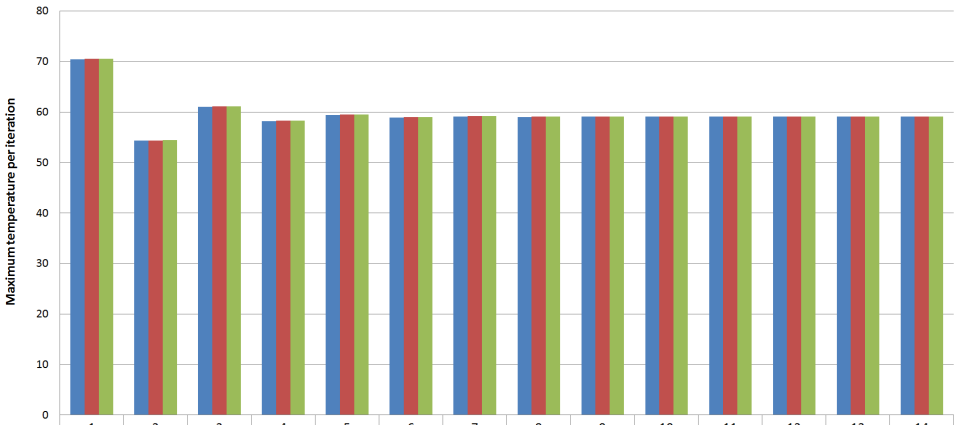

	1	2	3	4	5	6	7	8	9	10	11	12	13	14
40 elements through thickness	70.4374	54.3415	61.0452	58.2219	59.4133	58.9103	59.1227	59.033	59.0709	59.0549	59.0617	59.0588	59.06	59.0595
20 elements through thickness	70.4815	54.3717	61.0796	58.2549	59.4467	58.9437	59.156	59.0664	59.1042	59.0882	59.095	59.0921	59.0933	59.0928
4 elements through thickness	70.487	54.3879	61.0971	58.2702	59.4638	58.9597	59.1726	59.0827	59.1207	59.1046	59.1114	59.1085	59.1097	59.1092

Figure 3.5: Effect of number of element through wall thickness on maximum shaft temperature (four layers)

The temperature distribution within the shaft's wall in radial direction for the converged shaft temperature is shown in Figure 3.6. A continuous temperature distribution is obtained and the maximum temperature is reached at the outer surface of the driveshaft.

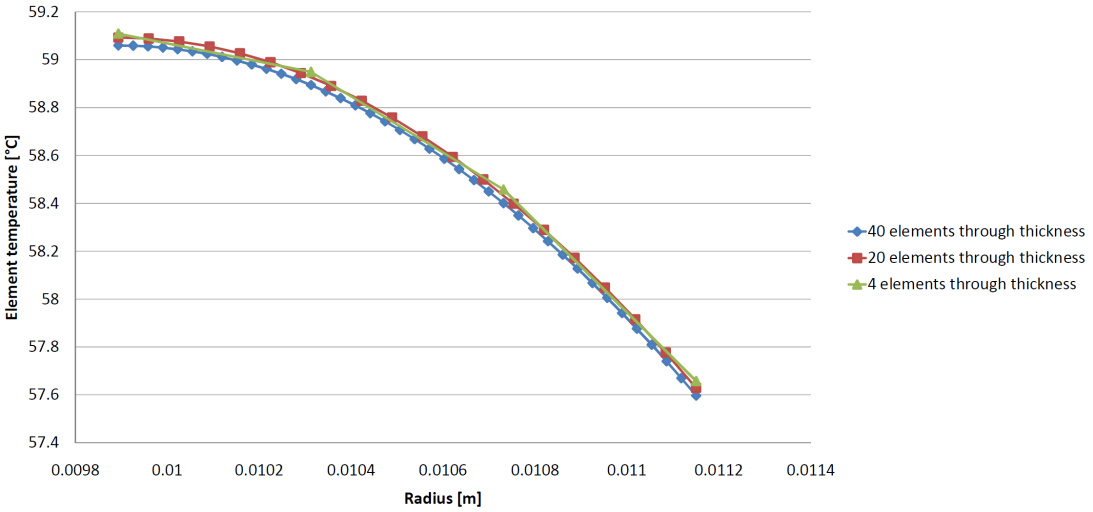

Figure 3.6: Temperature distribution within the shaft's wall (four layers)

In Figure 3.7, a driveshaft with 16 layers and a stacking sequence of [60/-60/45/-45/30/-30/60/-60/45/-45/80/-80/45/-45/80/-80]. The blue bar represents a driveshaft with four elements per layer (a total of 64 elements), the red bar two elements per layer (a total of 32 elements) and the green bar one element per layer (a total of 16 elements). The shaft temperature converges after

11 iterations for all three cases. A maximum discrepancy of the maximum shaft temperature of less than 0.5% occurs. The computation time, however, increases by a factor of more than 14 if the number of elements in thickness direction is quadrupled.

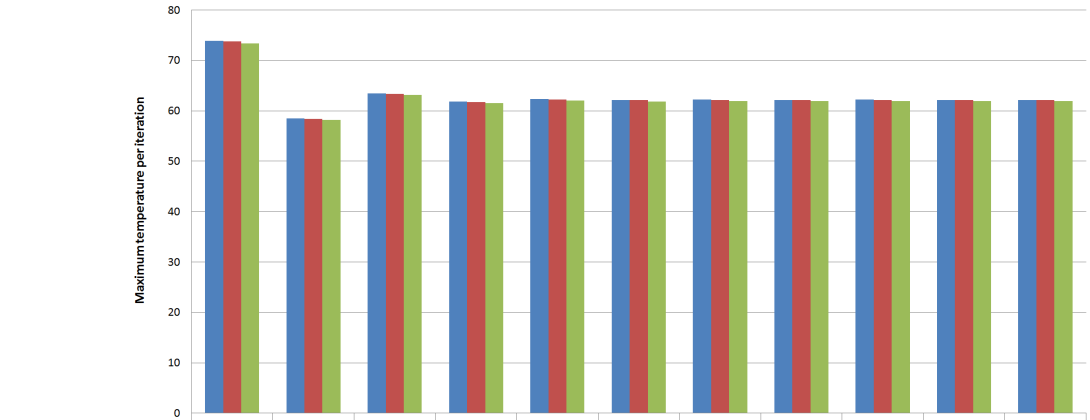

	1	2	3	4	5	6	7	8	9	10	11
64 elements through thickness	73.8579	58.4435	63.4066	61.7834	62.3132	62.1401	62.1967	62.1782	62.1842	62.1822	62.1829
32 elements through thickness	73.753	58.4053	63.3495	61.7319	62.2601	62.0875	62.1439	62.1254	62.1315	62.1295	62.1301
16 elements through thickness	73.3999	58.2342	63.1241	61.5238	62.0466	61.8757	61.9316	61.9133	61.9193	61.9173	61.918

Figure 3.7: Effect of number of element through wall thickness on accuracy (16 layers)

The temperature distribution within the wall of the shaft in radial direction for the converged shaft temperature is shown in Figure 3.8. Again, maximum temperature is reached at the outer shaft surface.

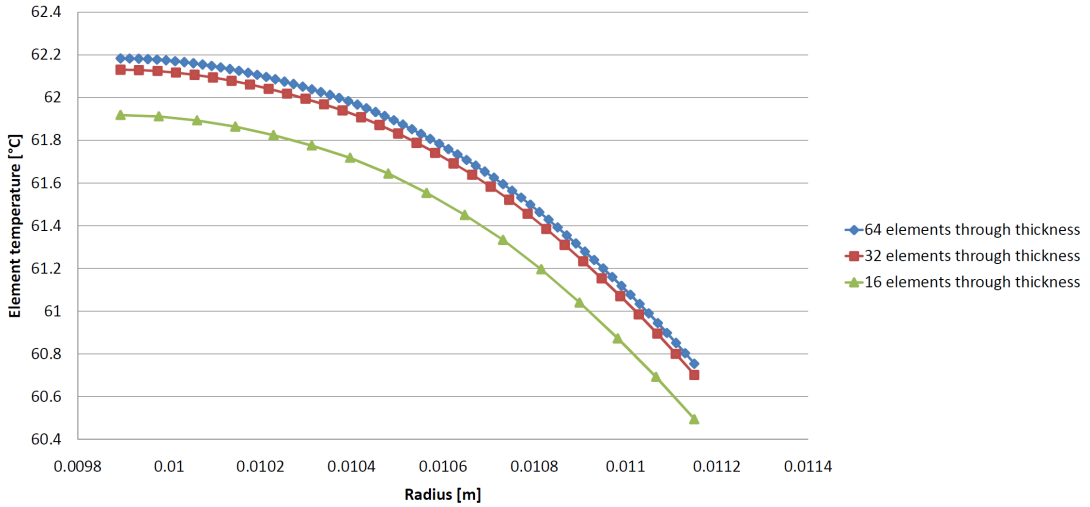

Figure 3.8: Temperature distribution within the shaft's wall (16 layers)

The same calculation was carried out for other stacking sequences and the maximum discrepancy always stayed below 1.5% for a shaft consisting of 16 layers

compared to 64 layers. Therefore, only one element per layer is used in the following self-heating calculation within the driveshaft. By reducing the number of elements to one element per layer, computation time could significantly be reduced which is extremely beneficial for a driveshaft optimization.

3.3.4 Failure Criterion

The ultimate shaft temperature is selected to be 100°C based on experimental results by Sollenberger (2010). A so-called reduction factor of 1.2 is applied which is, strictly speaking, not a safety factor since a Celsius temperature scale is utilized. A Kelvin temperature scale would have to be applied instead, however, this is not done here. Taking this reduction factor into account, a shaft temperature of 83.3°C (= 100° C/1.2) is not to be exceeded.

The margin of safety (MoS) for the maximum temperature calculation due to self-heating is given by Equation 3.12. The value of this margin of safety factor needs to be higher than 1 to avoid overheating of the shaft.

$$MoS_{overheating} = \frac{\vartheta_{ult}}{\vartheta_{S,max}(\mathbf{x})} \cdot \frac{1}{S_{f,h}} \tag{3.12}$$

3.4 Stress and Strain Calculation for a Misaligned Shaft

3.4.1 Assumptions

An analytical solution for a coaxial orthotropic cylinder subjected to torsion, bending and tensile loads is presented by Jolicoeur and Cardou (1994). Following assumptions are made.

- A thick-walled, orthotropic cylinder is considered
- Elastic body under small strains
- Constant loads along the axial axis
- No shear load resultant
- Stresses and strains are functions of r and θ only and independent of z which implies constant curvature of the bent cylinder.
- No moisture effects are considered

Since the Bernoulli-Euler hypothesis is not used, warping and rotation of the cross sections result.

3.4.2 Modeling

It is important to mention that this stress and strain calculation is utilized in two different parts of the structural model. First, ply-level stresses and strains need to be calculated for a multi-layered tube subjected to a bending moment. Since the applied torque is not cyclic, it does not contribute to heat generation and must not be considered in the stress and strain calculation for the self-heating model. Second, ply-level stresses and strains are calculated for a shaft subjected to torque and a bending moment in order to identify maximum stresses and strains.

The lamina elastic constants C_{ij} are inputs to the stress and strain calculation by Jolicoeur and Cardou (1994) and can be obtained by the generalized Hooke's law.

A brief procedure of the model of Jolicoeur and Cardou (1994) is shown below but not repeated here in detail. The reader is referred to Jolicoeur and Cardou (1994) for a detailed explanation of the model.

1. Constitutive equations by Lekhnitskii (1981)
2. Displacements using procedure by Lekhnitskii (1981)
3. Stress functions using Lekhnitskii's (1981) stress functions F and Φ
4. Separation of variables
5. General solution of pure bending problem
6. General solution of axially symmetric problem
7. Complete general solution
8. Stresses and displacement
9. Boundary conditions

Stresses and strains obtained by this model are laminate stresses. Lamina stresses and strain in the [123]-coordinate system are obtained by a transformation into the local coordinate system which is shown in many composite books such as Daniel and Ishai (2006).

Results for an angle-ply laminate are shown in Subsection 5.2.

3.4.3 Validation

The validation of the stress and calculation is done within two approaches. First, results are compared to Jolicoeur and Cardou (1994) to verify a correct coding of the structural model. Second, results are compared to FE-calculations which were carried out by Y. Shan (unpublished research work).

The verification results compared to Jolicoeur and Cardou (1994) are shown in Figures 3.9, 3.10 , 3.11.

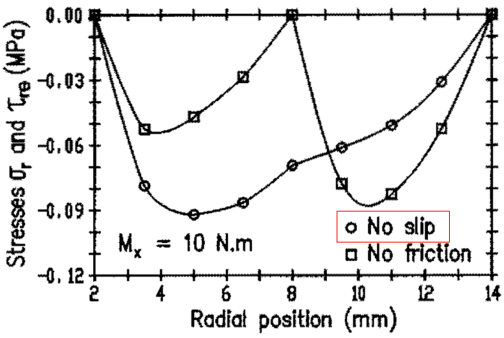

(a) Jolicoeur and Cardou (1994)

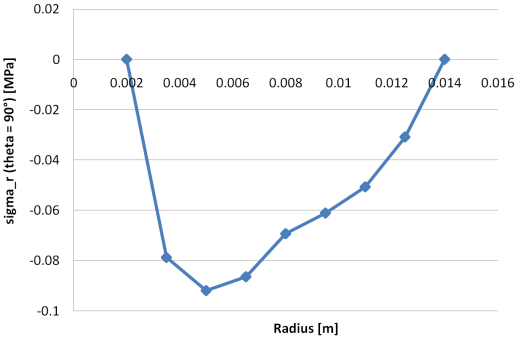

(b) Structural Model

Figure 3.9: Validation of stress and strain calculation - σ_r, $\theta = 90°$

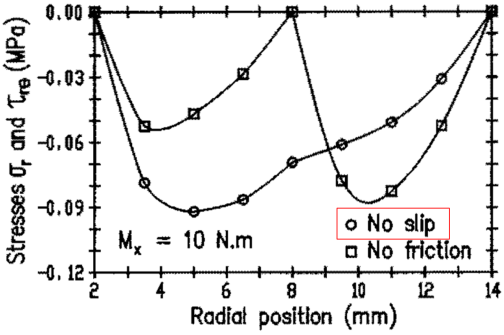

(a) Jolicoeur and Cardou (1994)

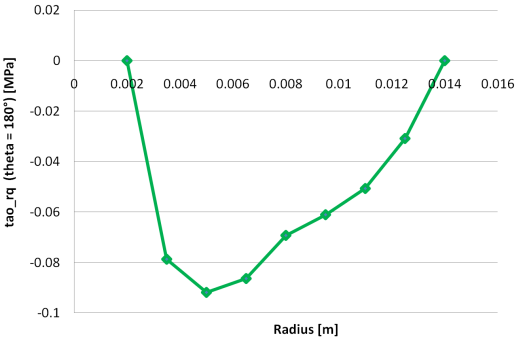

(b) Structural Model

Figure 3.10: Validation of stress and Strain calculation - $\tau_{r\theta}$, $\theta = 180°$

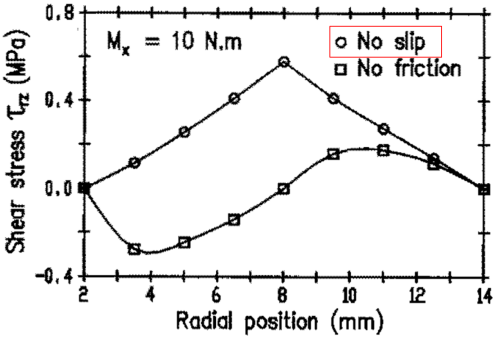

(a) Jolicoeur and Cardou (1994)

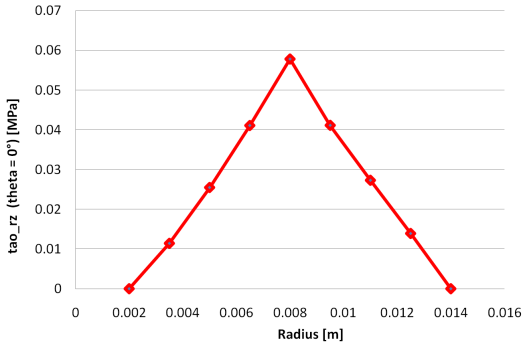

(b) Structural Model

Figure 3.11: Validation of stress and Strain calculation - τ_{rz}, $\theta = 0°$

Y. Shan (unpublished research work at Penn State) investigated two different loading cases. In the first one, a bending moment M_x=50 Nm is applied to the shaft and no axial force or torque is present. In the latter case, an axial force P=1000 N is applied only. Results for the first loading cases are shown in Figures 3.12, 3.13, 3.14 and 3.15. Results of the second loading cases are presented in Appendix B.

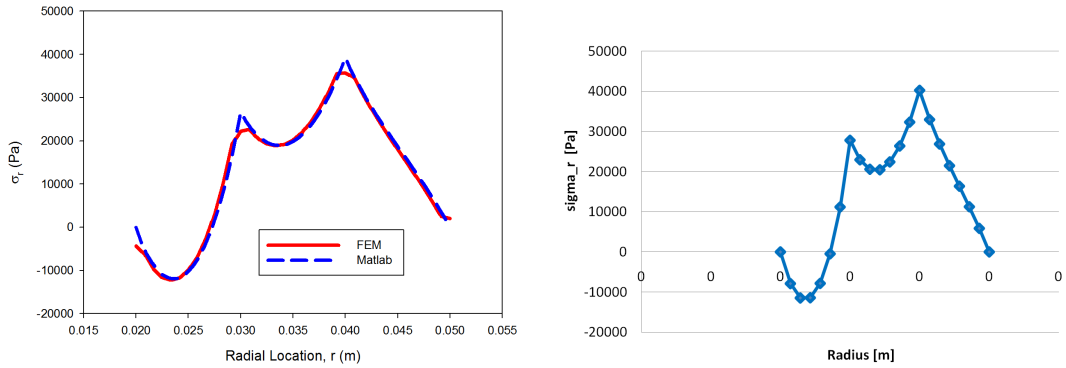

(a) Verification, to Y. Shan (unpublished) (b) Structural Model

Figure 3.12: Validation of stress and Strain calculation - σ_r (FE)

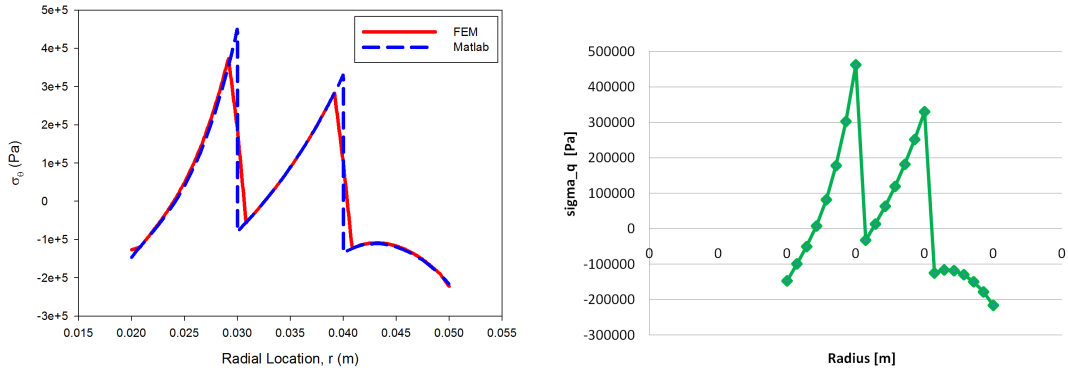

(a) Verification, to Y. Shan (unpublished) (b) Structural Model

Figure 3.13: Validation of stress and strain calculation - σ_θ (FE)

All results match nicely which assures right coding of the structural model and a strong theoretical foundation for the stress and strain calculation.

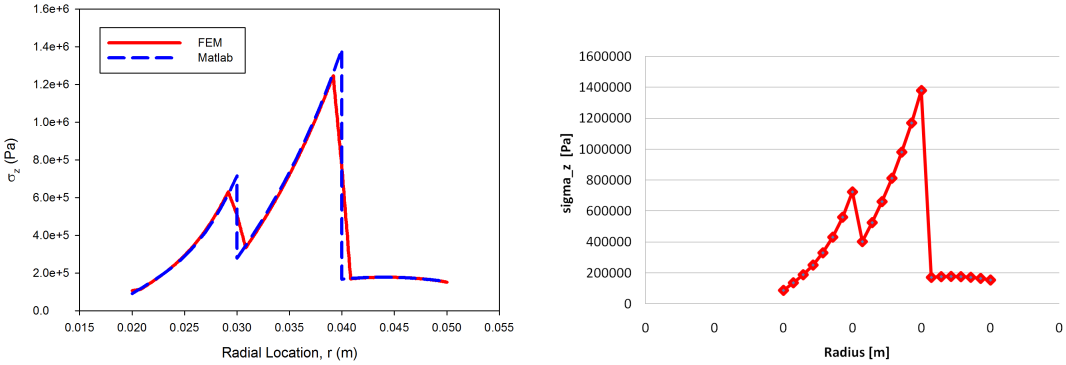

(a) Verification, to Y. Shan (unpublished) (b) Structural Model

Figure 3.14: Validation of stress and strain calculation - σ_z (FE)

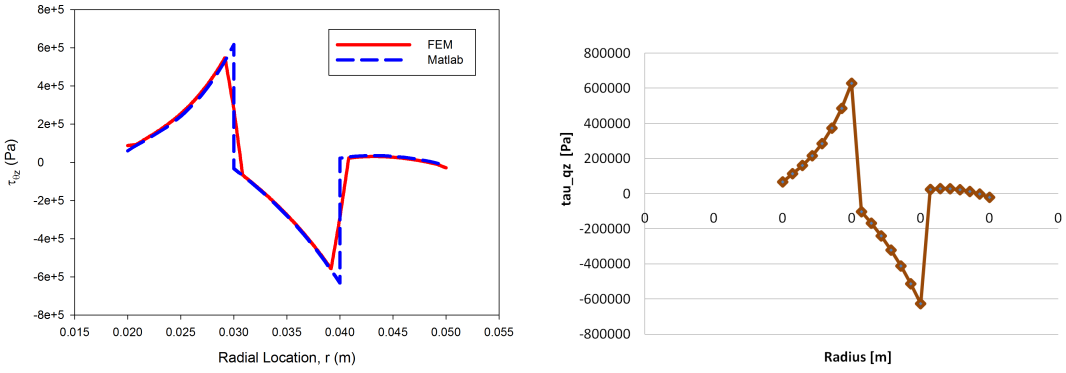

(a) Verification, to Y. Shan (unpublished) (b) Structural Model

Figure 3.15: Validation of stress and strain calculation - $\tau_{\theta z}$ (FE)

3.4.4 Failure Criteria

Commonly used failure criteria such as Tsai-Wu and Tsai-Hill are not able to predict failure of FMC materials well. The effect the softer material system seems too significant.

A maximum ply-level stress and maximum ply-level strain criterion is applied within the structural model to predict failure. Even though, the laminate might be able to sustain more loading, ply failure is to be avoided for fatigue reasons. A linear stress and strain approach is used. Since FMCs typically show a nonlinear material behavior, one might expect a maximum stress criterion to be critical in any case. This, however, does not have to true for any stacking sequence since temperature- and frequency-dependent material properties are utilized within the stress and strain calculation. Dynamic moduli, for instance G_{12}, can be much lower compared to quasi-static moduli. Consequently, the lamina failure strain is reached before lamina strength. To sum up, both, a maximum stress and a maximum strain criteria, are embedded within the structural model to assure that strength and failure strains of the lamina are not exceeded.

Based on experiments carried out by S. Sollenberger, T. Henry and B. Wimmer, lamina strengths and lamina failure strains for LF750D/AS4D are obtained. The numerical values are summarized below.

- Tensile ply-level failure strain in 1-direction:
  $\varepsilon_{11,t} \cong \varepsilon_{x,fiber,tens} = 18000\ \mu\varepsilon = 1.8\%$
- Tensile ply-level failure strain in 2-direction:
  $\varepsilon_{22,t} \cong \varepsilon_{x,tens}(\theta = 88°) = 9900\ \mu\varepsilon = 0.99\%$
- Compressive ply-level failure strain in 1-direction:
  $\varepsilon_{11,c} \cong -1600\ \mu\varepsilon$ = -0.16 % [7]
- Compressive ply-level failure strain in 2-direction:
  $\varepsilon_{22,c} \cong \varepsilon_{x,comp}(\theta = 88°) = -62300\ \mu\varepsilon$ = -6.23%
- Shear ply-level failure strain in 1-2 direction:
  $\gamma_{12} = \gamma_{12}(\theta = 45°)$ [8] $= \pm 58000\ \mu\varepsilon = \pm\ 5.8\%$
- Tensile ply-level strength in 1-direction:
  $\sigma_{11,t} \cong \sigma_{11,fiber,tens} \cdot V_{fc} = 2613$ MPa
- Tensile ply-level strength in 2-direction:
  $\sigma_{22,t} \cong \sigma_{x,tens}(\theta = 88°) = 10.10$ MPa

[7] This value is based on an empirical law (Bakis, C. E., personal communication, August 2010). Experimental data for strength and failure strain is not available at this point of the project.

[8] By applying CLT, it can be shown that that $\gamma_{12} = \varepsilon_x - \varepsilon_y = \varepsilon_x(\theta = 45°) \cdot (1 + \nu_{xy})$

- Compressive ply-level strength in 1-direction:
  $\sigma_{11,c} \cong E_{11,aver} \cdot \varepsilon_{11,c} =$ -176.0 MPa
- Compressive ply-level strength in 2-direction:
  $\sigma_{22,c} \cong \sigma_{x,comp}(\theta = 88°) =$ -27.53 MPa
- Shear ply-level strength in 1-2 direction:
  $\tau_{12} = \tau_{12}(\theta = 45°)$[9] $= \pm$ 68.10 MPa

The same safety factor for the stress and strain calculation is assumed within the structural model. It is selected to be $S_{f,s} = 1.2$ which is a typical value for lightweight structures.

The margin of safety for the strain and stress calculation is given by Equations 3.13 and 3.14, respectively. If the values of these two margin of safety factors are higher than 1, the shaft fulfills strain and stress requirements.

$$MoS_{strain} = \left(\frac{\varepsilon_{ij,ult}}{\varepsilon_{ij,max}}\right)_{min} \cdot \frac{1}{S_{f,s}} \tag{3.13}$$

$$MoS_{stess} = \left(\frac{\sigma_{ij,ult}}{\sigma_{ij,max}}\right)_{min} \cdot \frac{1}{S_{f,s}} \tag{3.14}$$

3.5 Critical Speed Calculation for a Spinning Shaft

3.5.1 Assumptions

Following assumptions are made for the critical speed analysis.

- The shaft rotates at constant speed about its longitudinal axis. The transient phase at the beginning and end of operation is not looked at.
- The shaft has a uniform, circular cross section.
- The driveshaft is modeled as a Bresse-Timoshenko beam which implies that first-order shear deformation theory with rotatory inertia and gyroscopic action is used.
- A perfectly balanced shaft is assumed meaning that at every cross section, the center of mass is perfectly aligned with the geometric center.
- No axial forces or torques are applied to shaft.
- All damping and nonlinear effects are excluded.
- The shaft is pinned at both ends.

[9] It can be shown that $\tau_{12} = \sigma_x(\theta = 45°)/2$

3.5.2 Modeling

The critical speed, also referred to as whirl instability, calculation for a spinning shaft is based on Bert and Kim (1995c). The critical speed is defined as the point at which the spinning shaft reaches its first natural frequency.

A model by Sun and Li (1988) is used to calculate 3D material effective elastic constants. These effective elastic constants are inputs in the critical speed calculation.

A Cartesian coordinate system which is fixed in space is used. The longitudinal axis is selected as x-axis whereas the y- and z-coordinates are perpendicular to it. Applying Hamilton's principle, the equations of motion for a rotating anisotropic Bresse-Timoshenko beam are given by Equation 3.15 (Bert and Kim (1995c)).

$$\begin{aligned}
C_S \cdot \left(\frac{\partial^2 v}{\partial x^2} - \frac{\partial \psi_z}{\partial x} \right) &= \rho \cdot A \cdot \frac{\partial^2 v}{\partial t^2} \\
C_S \cdot \left(\frac{\partial^2 w}{\partial x^2} - \frac{\partial \psi_y}{\partial x} \right) &= \rho \cdot A \cdot \frac{\partial^2 w}{\partial t^2} \\
C_B \cdot \frac{\partial^2 \psi_y}{\partial x^2} + \frac{C_{BT}}{2} \cdot \frac{\partial^2 \phi}{\partial x^2} + C_S \cdot \left(\frac{\partial w}{\partial x} - \psi_y \right) &= \rho \cdot I \cdot \frac{\partial^2 \psi_y}{\partial t^2} - 2 \cdot \rho \cdot I \cdot \Omega \cdot \frac{\partial \psi_z}{\partial t} \\
C_B \cdot \frac{\partial^2 \psi_z}{\partial x^2} + \frac{C_{BT}}{2} \cdot \frac{\partial^2 \phi}{\partial x^2} + C_S \cdot \left(\frac{\partial v}{\partial x} - \psi_z \right) &= \rho \cdot I \cdot \frac{\partial^2 \psi_z}{\partial t^2} - 2 \cdot \rho \cdot I \cdot \Omega \cdot \frac{\partial \psi_y}{\partial t} \\
C_T \cdot \frac{\partial^2 \phi}{\partial x^2} + \frac{C_{BT}}{2} \cdot \left(\frac{\partial^2 \psi_y}{\partial x^2} + \frac{\partial^2 \psi_z}{\partial x^2} \right) &= \rho \cdot J \cdot \frac{\partial^2 \phi}{\partial t^2}
\end{aligned} \tag{3.15}$$

where C_S is the transverse shear stiffness of the shaft (see Equation 3.16), C_B the bending stiffness of the shaft (see Equation 3.18), C_B the bending-twisting coupling stiffness of the shaft (see Equation 3.19). The displacement in y- and z-direction are denoted by v and w, respectively and the angle of twist by ϕ. ψ_y and ψ_z are the bending slope associated with rotation about the y- and z-axis, respectively. A is the cross-sectional area, I the area moment of inertia and J the polar area moment of inertia of the shaft. The density and rotational speed is denoted by ρ and Ω, respectively.

It may be noted that the shear stiffness factor C_S is different than in Bert and Kim (1995c). C_S is calculated by Dharmarajan and McCutchen (1973) and is used by Bert and Kim (1995c). However, in Dharmarajan and McCutchen (1973), the z-direction is selected to be the axial direction whereas in Bert and Kim (1995c) the x-direction is the axial direction. Bert and Kim (1995c) did not adapt that C_S-factor to the coordinate system used by Dharmarajan and McCutchen (1973). This has been corrected by using the in-plane shear modulus $\bar{G}_{xy}$ instead of $\bar{G}_{xz}$ in Equation 3.16.

$$C_S = K \cdot A \cdot \bar{G}_{xy} \tag{3.16}$$

where K is the shear correction coefficient (see Equation 3.17) of the shaft.

It may also be noted that the K-factor is different from Bert and Kim (1995c) for the same reason as for the C_S-factor which is explained above. $\bar{G}_{xz}$, $\bar{\nu}_{xz}$ and $\bar{E}_{zz}$ is changed to the in-plane properties $\bar{G}_{xy}$, $\bar{\nu}_{xy}$ and $\bar{E}_{xx}$ as shown in Equation 3.17.

In addition to this, it can be shown that the K-factor equation is incorrect. In fact it is already wrong in Dharmarajan and McCutchen (1973). If Equation 3.17 is compared to equation (A-5) in Bert and Kim (1995c), it can be seen that one sign is different (see Equation C.6). Using this corrected K factor, the K factor for thin-walled shaft ($\bar{m} \cong 1$) is now correctly obtained according to equation (A-6) in Bert and Kim (1995c).

$$K = \frac{\frac{6}{7} \cdot (1 - \bar{m}^4) \cdot (1 + \bar{m}^2)}{1 + \frac{27}{7} \cdot \bar{m}^2 \cdot (1 - \bar{m}^2) - \bar{m}^6 - 2 \cdot \left(\frac{\bar{\nu}_{xy} \cdot \bar{G}_{xy}}{7 \cdot \bar{E}_{xx}}\right) \cdot [1 + 9 \cdot \bar{m}^2 \cdot (1 - \bar{m}^2) - \bar{m}^6]} \tag{3.17}$$

where $\bar{m} = \frac{R_i}{R_o}$.

$$C_B = \frac{\pi}{4} \cdot \sum_{k=1}^{N} \bar{Q}_{11}^{(k)} \cdot \left[R_{o(k)}^4 - R_{i(k)}^4\right] \tag{3.18}$$

where k is the ply number, N the total number of plies and (k) denotes the k^{th} ply.

$$C_{BT} = \sum_{k=1}^{N} \bar{Q}_{16}^{(k)} \cdot \left[R_{o(k)}^4 - R_{i(k)}^4\right] \tag{3.19}$$

$$C_T = \frac{\pi}{2} \cdot \sum_{k=1}^{N} \bar{Q}_{66}^{(k)} \cdot \left[R_{o(k)}^4 - R_{i(k)}^4\right] \tag{3.20}$$

Assuming normal modes, v, w and ϕ is given by Equation 3.21.

$$\begin{aligned} v(x,t) &= V(x) \cdot e^{i \cdot \omega \cdot t} \\ w(x,t) &= W(x) \cdot e^{i \cdot \omega \cdot t} \\ \phi(x,t) &= X(x) \cdot e^{i \cdot \omega \cdot t} \end{aligned} \tag{3.21}$$

By substituting them into the equations of motion, three coupled ordinary differential equations as a function of x are obtained. For a shaft pinned at both ends, a set of homogeneous algebraic equations is to be solved which can be expressed by Equation 3.22.

$$\begin{bmatrix} C_{11} & i \cdot C_{12} & C_{13} \\ -i \cdot C_{12} & C_{11} & C_{13} \\ C_{31} & C_{31} & C_{33} \end{bmatrix} \begin{Bmatrix} \bar{V} \\ \bar{W} \\ \bar{X} \end{Bmatrix} = \begin{Bmatrix} 0 \\ 0 \\ 0 \end{Bmatrix} \tag{3.22}$$

where $\lambda = m\frac{\pi}{L}$, L is the length of the shaft between supports and m the mode number The coefficients C_{11}, C_{12}, C_{13}, , C_{31} and C_{33} are given by Equation 3.23.

$$\begin{aligned} C_{11} &= C_B \cdot \lambda^4 - \left(\rho \cdot I + \frac{C_B}{C_S} \cdot \rho \cdot A\right) \cdot \omega^2 \cdot \lambda^2 + \left(\frac{\rho^2 \cdot I \cdot A}{C_S} \cdot \omega^2 - \rho \cdot A \cdot \omega^2\right) \\ C_{12} &= 2 \cdot \rho \cdot I \cdot \Omega \cdot \omega \cdot \left(\lambda^2 - \frac{\rho \cdot A}{C_S} \cdot \omega^2\right) \\ C_{13} &= \frac{C_{BT}}{2} \cdot \lambda^3 \\ C_{31} &= C_{13} - \frac{C_{BT}}{2} \cdot \frac{\rho \cdot A}{C_S} \cdot \lambda \cdot \omega^2 \\ C_{33} &= C_T \cdot \lambda^2 - \rho \cdot J \cdot \omega^2 \end{aligned} \tag{3.23}$$

To obtain a nontrivial solution, the determinant of the matrix in Equation 3.23 must vanish which yields to a fifth order equation in ω^2 and is to be solved.

In the structural model, material properties at the shaft temperature and operating rotational speed are used. A more accurate approach is to use material properties at the critical frequency. This requires an iterative approach within the whirling calculation. Furthermore, if material properties at critical speed are used, the shaft temperature due to self-heating is to be calculated at critical speed, too. This requires a second iterative loop within this whirling calculation.

The results obtained for angle-ply laminates using constant material properties at operating speed and shaft temperature are shown in Table 3.4 in the second row. In the third row, critical speeds are shown if material properties at critical speed and the shaft temperature, when spinning at critical speed, are shown.

If the actual critical frequency and shaft temperature are used within the whirling calculation, the computation time increases by a factor of 10^4[10]. This huge increase of the whirling computation time is due to the fact that the self-heating model needs to be executed several times within the critical speed calculation. For computation time reasons, constant material properties at operating

[10]The computation time for the entire structural model increases by a factor of five

Table 3.4: Critical speed calculation using material properties at critical speed (seven layers, three mid-span bearings)

Angle-ply laminate	Whirling (f=4116, T=T_S) [critical RPM]	Whirling ($f \neq$ const., $T \neq$ const.) [critical RPM]	Deviation in %
10°	4919.2	4918.7	-0.01
15°	4911	4912.62	0.032
30°	4098.1	4098.11	-0.0007
45°	2775.8	2775.56	-0.0071
60°	1474.8	1462.32	-0.85
75°	747.04	697.75	-6.6
88°	661.74	600.48	-9.3

frequency and shaft temperature due to self-heating at the operating speed are used. By applying an additional safety factor of $S_{f,2} = 1.1$, this frequency and temperature effect is taken into account (see Subsection 3.5.4). This factor accounts for the maximal derivation of 10%, which reflects a worst case scenario, by neglecting material properties at critical speed and its corresponding shaft temperature.

3.5.3 Validation

The critical speed calculation model is presented in this subsection.

The shear stiffness factor C_S and the shear correction coefficient K were shown to be incorrect in Bert and Kim (1995c). Therefore, the model is not only validated by Bert and Kim (1995c) but also by more recent critical speed models using FE-approaches (Boukhalfa et al. (2008) and Chang et al. (2004)). Thereby, the critical speed calculation within the structural can be verified and validated.

In Figure 3.16, critical speed is calculated for an off-axis laminate with 10 layers. The fiber angle orientation is shown on the x-axis and the critical speed on the y-axis. The blue bar represents the model from Boukhalfa et al. (2008), the green bar the model from Chang et al. (2004) , the violet bar the model by Bert and Kim (1995c) and the red bar shows the results of the structural model.

Critical speeds agree well for any fiber angle orientation and any reference that it is compared to.

In Figure 3.17, critical speeds are calculated for a [90/45/-45/0/0/0/0/0/0/45] laminate. The length over diameter ratio L/D is shown on the x-axis and the critical speed on the y-axis. As in Figure 3.16, the different colors of the bars represent different models used to predict whirling instability.

The whirling model used within the structural model seems to overestimate critical speed for a L/D-ratio of two by 16% if compared to Bert and Kim (1995c)

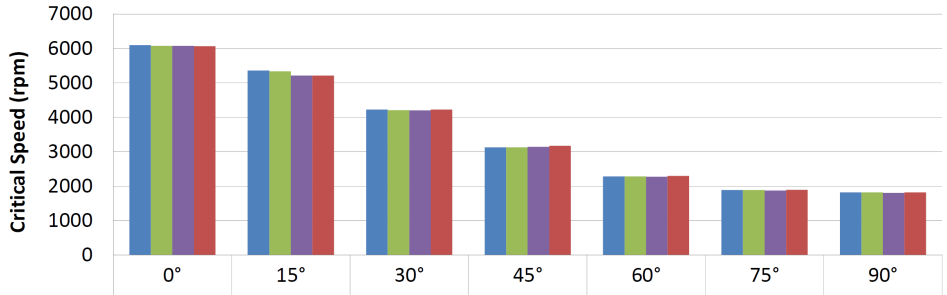

	0°	15°	30°	45°	60°	75°	90°
Boukhalfa et al. (2008)	6094	5359	4222	3129	2284	1890	1816
Chang et al. (2004)	6072	5331	4206	3124	2284	1890	1816
Bert and Kim (1995c)	6072	5209	4197	3143	2278	1874	1803
Structural Model	6067	5216	4224	3173	2300	1891	1818

Figure 3.16: Validation: critical speed vs. fiber angle orientation

and by 11% if compared to Boukhalfa et al. (2008). However, a L/D-ratio of two is very low. Considering a Blackhawk driveline with four mid-span bearings[11], the L/D-ratio is determined to be 19. If six mid-span bearings are considered, the L/D-ratio is 14. For a L/D ratio of 15, the whirling model overestimates critical speed by only 1.4% if compared to Bert and Kim (1995c) and by 1.3% if compared to Boukhalfa et al. (2008). This discrepancy is low and results are within engineering accuracy.

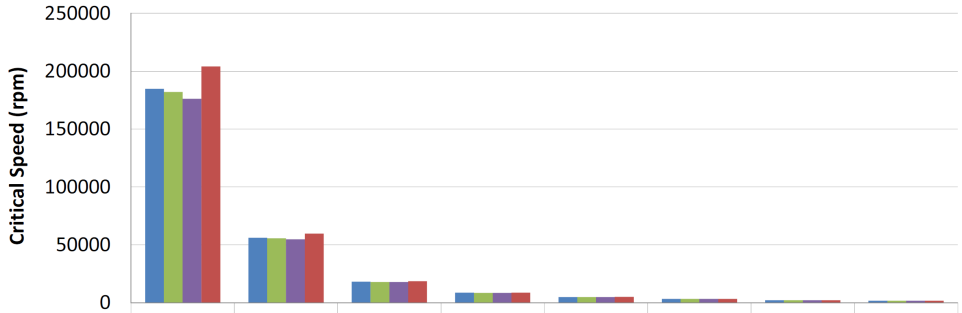

	2	5	10	15	20	25	30	35
Boukhalfa et al. (2008)	184667	56196	18005	8549	4934	3198	2236	1650
Chang et al. (2004)	181996	55706	17929	8527	4925	3192	2233	1648
Bert and Kim (1995c)	176300	54830	17880	8543	4945	3209	2246	1658
Structural Model	204010	59661	18470	8662	4973	3214	2244	1654

Figure 3.17: Validation: critical speed vs. L/D-ratio

In Appendix C, it is shown that results do not match well if the K- and C_S-factor as presented by Bert and Kim (1995c) are utilized in the critical speed calculation model.

[11] A current metallic Blackhawk driveline currently has four mid-span bearings.

To sum up, the critical speed calculation within the structural model uses the stiffness factor C_S, given by Equation 3.16, and the shear correction coefficient K, given by Equation 3.17. It was shown that by applying this factors, results match nicely with other whirl instability models if the L/D ratio is above 5.

3.5.4 Failure Criterion

The critical speed is the shaft's first natural frequency. Since the shaft is to be operated subcritically, the first natural frequency is not to be exceeded. Therefore, the critical speed f_{crit} needs to be lower than the operating shaft speed f_{op}. A safety factor of $S_{f,w,1} = 1.2$ is applied to account for deviation in the modeling. A second safety factor $S_{f,w,2} = 1.1$ is applied since material properties at operating speed (not at actual critical speed) and shaft temperature due to self-heating, for a shaft spinning at operating speed, were used (see Subsection 3.5.2).

The operating shaft speed must not exceed the critical frequency which is given by Equation 3.24. In other words, the critical speed has to be higher than the operating speed.

$$f_{crit} = \frac{f_{op}}{S_{f,w,1} \cdot S_{f,w,2}} = \frac{f_{op}}{S_{f,w}} \tag{3.24}$$

The margin of safety for the critical speed calculation is given by Equation 3.25. The value of this margin of safety factor needs to be higher than 1 so that whirling of the shaft can be avoided. The higher the critical speed, the higher the margin of safety for whirling.

$$MoS_{whirl} = \frac{f_{crit}}{f_{op}} \cdot \frac{1}{S_{f,w}} \tag{3.25}$$

3.6 Buckling

3.6.1 Assumptions

Following assumption are made for buckling.

- The tube is thin, meaning the ratio of wall thickness to radius is small.
- The lamina material is linear elastic, macroscopically homogeneous and transverse isotropic in 23-plane direction for this calculation. The theory would, however, allow monoclinic and orthotropic lamina behavior, too.
- Displacements are small compared to the wall thickness, so that a linear strain-displacement relationship can be assumed. Also, displacements vary linearly across the shell thickness which is constant for fixed x and θ.

- A *very long* shaft is assumed, so that boundary conditions can be neglected.
- Bending moment due to misalignment is excluded.
- Body forces and body moments are negligible.
- Dissipative effects are neglected.
- A steady-state operation is assumed, the transient start-up phase is neglected.

A Blackhawk or Chinook helicopter driveline has a length to radius ratio of 38[12], 22, respectively . This can be regarded as a long shaft in a good approximation.

3.6.2 Modeling

The buckling model applied in the structural model is based on Cheng and Ho (1963) which is the same as in Bert and Kim (1995a) if Flügge's equations are applied. This buckling model is presented in the following.

A polar coordinate system is used as shown in Figure 3.18.

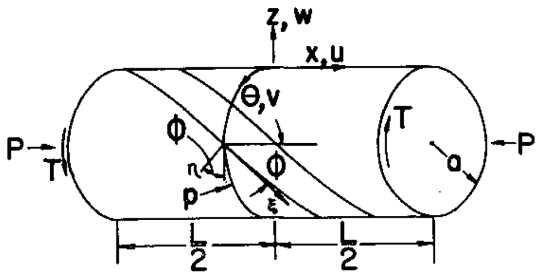

Figure 3.18: Coordinate system (Cheng and Ho (1963))

The strain and strain relations can be expressed by the general Hooke's law which can be reduced to the expression shown in Equation 3.26.

$$\begin{bmatrix} \sigma_{xx} \\ \sigma_{\theta\theta} \\ \sigma_{x\theta} \end{bmatrix} = \begin{bmatrix} C_{11} & C_{12} & C_{16} \\ C_{12} & C_{22} & C_{26} \\ C_{16} & C_{26} & C_{66} \end{bmatrix} \cdot \begin{bmatrix} \epsilon_{xx} \\ \epsilon_{\theta\theta} \\ \epsilon_{x\theta} \end{bmatrix} \tag{3.26}$$

The six elastic constants C_{11}, C_{12}, C_{16}, C_{22}, C_{26} and C_{66} are sufficient to express this behavior.

Kinematic relations are expressed as following (see Equation 3.27).

[12]If the same number of mid-span bearings is used as for the current metal design.

$$\begin{aligned}
\varepsilon_{xx} &= u_{,x} - z \cdot w_{,xx} \\
\varepsilon_{\theta\theta} &= \frac{v_{,\theta}}{r_m} - \frac{z}{r_m} \cdot \frac{w_{,\theta\theta}}{r_m + z} + \frac{w}{r_m + z} \\
\varepsilon_{x\theta} &= \frac{u_{,\theta}}{a + r_m} + \left(1 - \frac{z}{r_m}\right) \cdot v_{,x} - w_{,x\theta} \cdot \left(\frac{z}{r_m} + \frac{z}{r_m + z}\right)
\end{aligned} \tag{3.27}$$

where r_m is the mean radius of the shaft

If $\left(\frac{z}{a}\right)^n$ for $n = 3$ and higher are neglected, Equation 3.27 becomes Equation 3.28

$$\begin{aligned}
\varepsilon_{xx} &= \varepsilon_x^0 - z \cdot \kappa_x \\
\varepsilon_{\theta\theta} &= \varepsilon_\theta^0 + z \cdot \left(1 - \frac{z}{r_m}\right) \cdot \kappa_\theta \\
\varepsilon_{x\theta} &= \left(1 + \frac{z^2}{2 \cdot R_m^2}\right) \cdot \varepsilon_{x\theta}^0 + z \cdot \left(1 - \frac{z}{2 \cdot r_m}\right) \cdot \kappa_{x\theta}
\end{aligned} \tag{3.28}$$

where the strains at the middle surface are given by Equation 3.29.

$$\begin{aligned}
\varepsilon_{xx}^0 &= u_{,x} \\
\varepsilon_{\theta\theta}^0 &= \frac{1}{r_m} \cdot (v_{,\theta} + w) \\
\varepsilon_{x\theta}^0 &= \frac{u_{,\theta}}{r_m} + v_{,x}
\end{aligned} \tag{3.29}$$

The coefficients related to change of curvature and angle of twist are expressed by Equation 3.30.

$$\begin{aligned}
\kappa_x &= -w_{,xx} \\
\kappa_\theta &= -\frac{1}{R_m^2} \cdot (w_{,\theta\theta} + w) \\
\kappa_{x\theta} &= -\frac{2}{r_m} \cdot \left(w_{,x\theta} + \frac{u_{,\theta}}{2 \cdot r_m} - \frac{v_{,x}}{2}\right)
\end{aligned} \tag{3.30}$$

The following force/moment and strain relation is obtained (see Equation 3.31).

$$\begin{Bmatrix} N_{xx} \\ N_{\theta\theta} \\ N_{x\theta} \\ N_{\theta x} \\ M_{xx} \\ M_{\theta\theta} \\ M_{x\theta} \\ M_{\theta x} \end{Bmatrix} = \begin{bmatrix} A_{11}+\frac{B_{11}}{a} & A_{12}+\frac{B_{12}}{a} & A_{16}+\frac{B_{16}}{a}+\frac{D_{16}}{2\cdot a^2} \\ A_{12} & A_{22} & A_{26}+\frac{D_{26}}{2\cdot a^2} \\ A_{16}+\frac{B_{16}}{a} & A_{26}+\frac{B_{26}}{a} & A_{66}+\frac{B_{66}}{a}+\frac{D_{66}}{2\cdot a^2} \\ A_{16} & A_{26} & A_{66}+\frac{D_{66}}{2\cdot a^2} \\ B_{11}+\frac{D_{11}}{a} & B_{12}+\frac{D_{12}}{a} & B_{16}+\frac{D_{16}}{a} \\ B_{12} & B_{22} & B_{26} \\ B_{16}+\frac{D_{16}}{a} & B_{26}+\frac{D_{26}}{a} & B_{66}+\frac{D_{66}}{a} \\ B_{16} & B_{26} & B_{66} \end{bmatrix} \cdots$$

$$\cdots \begin{bmatrix} B_{11}+\frac{D_{11}}{a} & B_{12} & B_{16}+\frac{D_{16}}{2\cdot a} \\ B_{12} & B_{22}-\frac{D_{22}}{a} & B_{26}-\frac{D_{26}}{2\cdot a} \\ B_{16}+\frac{D_{16}}{a} & B_{26} & B_{66}+\frac{D_{66}}{2\cdot a} \\ B_{16} & B_{26}-\frac{D_{26}}{a} & B_{66}-\frac{D_{66}}{2\cdot a} \\ D_{11} & D_{12} & D_{16} \\ D_{12} & D_{22} & D_{26} \\ D_{16} & D_{26} & D_{66} \\ D_{16} & D_{26} & D_{66} \end{bmatrix} \begin{Bmatrix} \varepsilon^0_{xx} \\ \varepsilon^0_{\theta\theta} \\ \varepsilon^0_{x\theta} \\ \kappa_x \\ \kappa_\theta \\ \kappa_{x\theta} \end{Bmatrix} \tag{3.31}$$

where A_{ij}, B_{ij} and C_{ij} for $i, j = 1, 2, 6$ are given by Equation 3.32. N_{ij} are the resultant forces per unit length and M_{ij} the resultant moments per unit length.

$$(A_{ij}, B_{ij}, D_{ij}) = \int_{h/2}^{h/2} C_{ij} \cdot (1, z, z^2)\, dz \tag{3.32}$$

The differential equations of equilibrium can then be expressed as shown in Equation 3.33 ($P = p = 0$).

$$\begin{aligned} r_m \cdot N_{x,x} + N_{\theta x,\theta} - 2 \cdot T_S \cdot u_{,x\theta} &= 0 \\ r_m \cdot N_{\theta,\theta} + r_m^2 \cdot N_{x\theta,x} + M_{\theta,\theta} + r_m \cdot M_{x\theta,x} - 2 \cdot r_m \cdot T_S \cdot (v_{,x\theta} + w_{,x}) &= 0 \\ M_{\theta,\theta\theta} + r_m \cdot (M_{x\theta} + M_{\theta x})_{,x\theta} + r_m^2 \cdot M_{x,xx} - r_m \cdot N_\theta + & \\ 2 \cdot r_m \cdot T_S \cdot (v_{,x} - w_{,x\theta}) &= 0 \end{aligned} \tag{3.33}$$

where T_S is the external torsional (shearing) force per unit length.

By substituting Equations 3.29, 3.30 and 3.31 in 3.33, the differential equations of equilibrium are then given in terms of displacements. The resulting partial differential equations are not straight forward to solve. One approach to find a particular solution is obtained by the inverse method. It is considered that the displacement of the middle surface is given by Equation 3.34.

$$\begin{aligned} u &= U \cdot sin\left[\frac{\lambda \cdot x}{r_m} + n \cdot \theta\right] \\ v &= V \cdot sin\left[\frac{\lambda \cdot x}{r_m} + n \cdot \theta\right] \\ w &= W \cdot cos\left[\frac{\lambda \cdot x}{r_m} + n \cdot \theta\right] \end{aligned} \tag{3.34}$$

where n is the number of half-waves in the axial direction $\lambda = \frac{m \cdot \pi \cdot r_m}{L}$, m the number of waves in circumferential direction and U, V and W are constants.

Inserting Equation 3.34 in the differential equations of equilibrium in terms of displacements, Equation 3.35 is obtained ($q_1 = q_2 = 0$ since $p = P = 0$).

$$\begin{bmatrix} F_{11} - 2 \cdot n \cdot \lambda \cdot q_3 & 0 & F_{13} \\ F_{12} & F_{22} - 2 \cdot n \cdot \lambda \cdot q_3 & F_{23} - 2 \cdot \lambda \cdot q_3 \\ F_{13} & F_{23} - 2 \cdot \lambda \cdot q_3 & F_{33} - 2 \cdot n \cdot \lambda \cdot q_3 \end{bmatrix} \times \begin{bmatrix} U \\ V \\ W \end{bmatrix} \tag{3.35}$$

where $q_3 = \frac{1}{A_{22}} \cdot T$ and the coefficients F_{ij} are given by Equation 3.36.

$$\begin{aligned} F_{11} &= (\bar{A}_{11} + \bar{B}_{11}) \cdot \lambda^2 + 2 \cdot n \cdot \bar{A}_{16} \cdot \lambda + n^2 \cdot (\bar{A}_{66} - \bar{B}_{66} + \bar{D}_{66}) \\ F_{12} &= (\bar{A}_{16} + 2 \cdot \bar{B}_{16} + \bar{D}_{16}) \cdot \lambda^2 + n \cdot (\bar{A}_{12} + \bar{A}_{66} + \bar{B}_{12} + \bar{B}_{66}) \cdot \lambda \\ &\quad + n^2 \cdot \bar{A}_{26} \\ F_{13} &= (\bar{B}_{11} + \bar{D}_{11}) \cdot \lambda^3 + n \cdot (3 \cdot \bar{B}_{16} + \bar{D}_{16}) \cdot \lambda^2 + (n^2 \cdot (\bar{B}_{12} + 2 \cdot \bar{B}_{66} \\ &\quad - \bar{D}_{66}) + \bar{A}_{12}) \cdot \lambda + n^3 \cdot (\bar{B}_{26} - \bar{D}_{26}) + n \cdot (\bar{A}_{26} - \bar{B}_{26} + \bar{D}_{26}) \\ F_{22} &= (\bar{A}_{66} + 3 \cdot \bar{B}_{66} + 3 \cdot \bar{D}_{66}) \cdot \lambda^2 + 2 \cdot n \cdot (\bar{A}_{26} + 2 \cdot \bar{B}_{26} + \bar{D}_{26}) \cdot \lambda \\ &\quad + n^2 \cdot (1 + \bar{B}_{22}) \\ F_{23} &= (\bar{B}_{16} + 2 \cdot \bar{D}_{16}) \cdot \lambda^3 + n \cdot (\bar{B}_{12} + 2 \cdot \bar{B}_{66} + \bar{D}_{12} + 3 \cdot \bar{D}_{66}) \cdot \lambda^2 \\ &\quad + (n^2 \cdot (3 \cdot \bar{B}_{26} + 2 \cdot \bar{D}_{26}) + \bar{A}_{26} + \bar{B}_{26}) \cdot \lambda + n^3 \cdot \bar{B}_{22} + n \\ F_{33} &= \bar{D}_{11} \cdot \lambda^4 + 4 \cdot n \cdot \bar{D}_{16} \cdot \lambda^3 + 2 \cdot (n^2 \cdot (\bar{D}_{12} + 2 \cdot \bar{D}_{66}) + \bar{B}_{12}) \cdot \lambda^2 \\ &\quad + 2 \cdot n \cdot (2 \cdot n^2 \cdot \bar{D}_{26} + 2 \cdot \bar{B}_{26} - \bar{D}_{26}) \cdot \lambda + (n^2 - 1)^2 \cdot \bar{D}_{22} \\ &\quad + (2 \cdot n^2 - 1) \cdot \bar{B}_{22} + 1 \end{aligned} \tag{3.36}$$

where $\bar{A}_{ij}$, $\bar{B}_{ij}$, $\bar{D}_{ij}$ are given by Equation 3.37.

$$(\bar{A}_{ij}, \bar{B}_{ij}, \bar{D}_{ij}) = \frac{1}{A_{22}} \cdot \left(A_{ij}, \frac{B_{ij}}{r_m}, \frac{D_{ij}}{r_m^2}\right) \tag{3.37}$$

The determinant of the matrix in Equation 3.35 has to be equal to zero so that nontrivial solutions exist which yields to following equation (see Equation 3.38[13]).

$$c_3 \cdot q_3^3 + c_2 \cdot q_3^2 + c_1 \cdot q_3 + c_0 \;=\; 0 \tag{3.38}$$

where c_0, c_1, c_2 and c_3 are given by Equation 3.39.

$$\begin{aligned}
c_0 &= -(F_{13}^2 \cdot F_{22}) + 2 \cdot F_{12} \cdot F_{13} \cdot F_{23} - F_{11} \cdot F_{23}^2 - F_{12}^2 \cdot F_{33} + F_{11} \cdot F_{22} \cdot F_{33} \\
c_1 &= -4 \cdot F_{12} \cdot F_{13} \cdot \lambda + 4 \cdot F_{11} \cdot F_{23} \cdot \lambda + 2 \cdot F_{12}^2 \cdot \lambda \cdot n + 2 \cdot F_{13}^2 \cdot \lambda \cdot n \\
&\quad - 2 \cdot F_{11} \cdot F_{22} \cdot \lambda \cdot n + 2 \cdot F_{23}^2 \cdot \lambda \cdot n - 2 \cdot F_{11} \cdot F_{33} \cdot \lambda \cdot n \\
&\quad - 2 \cdot F_{22} \cdot F_{33} \cdot \lambda \cdot n \\
c_2 &= -4 \cdot F_{11} \cdot \lambda^2 - 8 \cdot F_{23} \cdot \lambda^2 \cdot n + 4 \cdot F_{11} \cdot \lambda^2 \cdot n^2 + 4 \cdot F_{22} \cdot \lambda^2 \cdot n^2 \\
&\quad + 4 \cdot F_{33} \cdot \lambda^2 \cdot n^2 \\
c_3 &= 8 \cdot \lambda^3 \cdot n - 8 \cdot \lambda^3 \cdot n^3
\end{aligned} \tag{3.39}$$

The solution can now easily be obtained by calculation the roots of q_1 and inserting the solution in Equation 3.40.

$$T \;=\; 2 \cdot \pi \cdot r_m^2 \cdot T_S \;=\; 2 \cdot \pi \cdot r_m^2 \cdot A_{22} \cdot q_3 \tag{3.40}$$

3.6.3 Validation

A buckling model proposed by Cheng and Ho (1963) and Bert and Kim (1995a), respectively, was implemented in the structural model. Cheng and Ho (1963) did not provide a validation case of his model in his work. Therefore, results of the buckling torque calculation are validated by Bert and Kim (1995a). It is to be noted that in the validation section of Bert and Kim (1995a), Sander's equations were used whereas in the structural model Flügge's equations are applied. Having mentioned this, a small discrepancy of these two models is to be expected.

In Figure 3.19, buckling torques for an off-axis laminate is shown. The fiber angle orientation is shown on the x-axis and the buckling torque on the y-axis. The blue bars represent results obtained by Bert and Kim (1995a) using Sander's equation whereas the red bars represent results obtained by using Flügge's equations. Considering that two different models are used, the results agree well and are within engineering accuracy.

[13]It is to be noted that factors of $q_i \cdot q_j \cdot q_k$ are not neglected here as this is done in the Cheng and Ho (1963)

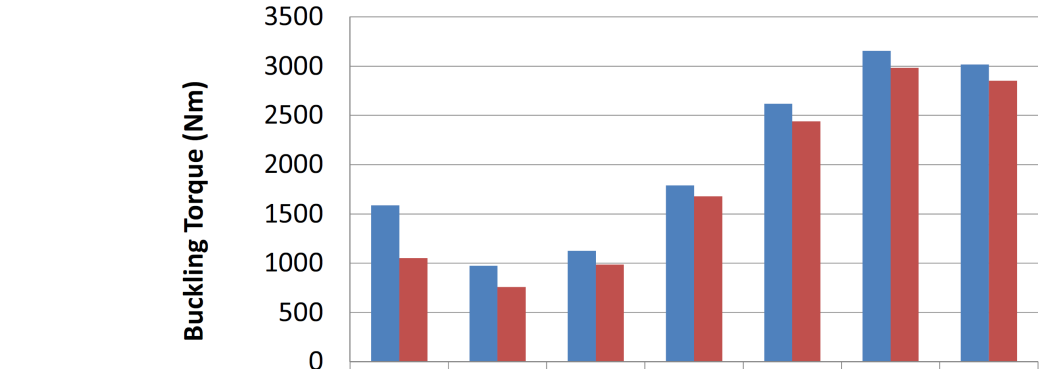

	0°	15°	30°	45°	60°	75°	90°
Bert and Kim (1995a): Sanders shell theory	1587	974	1126	1790	2617	3156	3016
Structural Model: Flügge's theroy	1053	759	985	1678	2440	2982	2850

Figure 3.19: Validation: buckling torque vs. fiber angle orienations

3.6.4 Failure Criterion

The critical buckling torque needs to be lower than the operating torque. In literature, safety factors for buckling of 3-5 are commonly applied. This high safety factor is mainly due to imperfections which lowers the buckling resistance significantly. Since the buckling calculation applied in the structural model is rather conservative (see Subsection 3.6.1) and a light-weight design is to be realized, a safety factor of $S_f = 3$ is utilized within the structural model.

The critical buckling torque T_{crit} can be expressed as following (see Equation 3.41). The applied buckling torque needs to be lower than the critical buckling torque to avoid buckling of the driveshaft.

$$T_{crit} = \frac{T_B}{S_f} \tag{3.41}$$

The margin of safety for the buckling calculation is given by Equation 3.42. The value of this margin of safety factor needs to be higher than 1 so that buckling of the shaft can be avoided.

$$MoS_{buckling} = \frac{T_{b,crit}(\mathbf{x})}{T_{op}} \cdot \frac{1}{S_{f,b}} \tag{3.42}$$

3.7 Calculation of CTEs for Multi-Directional Laminates

3.7.1 Assumptions and Purpose of CTE-Calculation

A transversally isotropic lamina material is assumed and the same assumptions as for Classical Lamination Theory apply. Additionally, no moisture effects are taken into consideration.

In the current metallic driveshaft design, a special end-fitting engineering design allows the shaft to move in axial direction which prevents an axial force in the driveshaft. However, in some extraordinary scenarios this end-fitting design fails and an axial force can arise. This can happen in extreme maneuvering where misalignment and thermal expansion in axial direction is very high. Howsoever, these special scenarios are not being investigated in the scope of this work since a calculation of axial force would require a complex modeling of the entire tailboom. This is to be avoided due to computation time reasons.

Nevertheless, the effect of thermal expansion in composites which can be significantly different to a metal design is discussed in this section. The aim of this investigation is to point out the importance of considering thermal expansion when designing an end-fitting for a composite driveshaft and a metallic tailboom.

3.7.2 Modeling

A temperature increase in the shaft can results in an elongation or contraction (!) of a multi-directional composite. In this calculation, the coefficients of thermal expansion in x-, y- and xy-plane are calculated. Inputs are the coefficients of thermal expansion in 1- and 2- direction, α_1 and α_2, respectively, which are to be determined from a UD-laminate. T. Henry (unpublished research work at Penn State) obtained these two values experimentally (see Table 3.5).

Table 3.5: CTE for lamina

α_1	$=$	$0.53 \cdot 10^{-6} \frac{1}{^\circ C}$
α_2	$=$	$94.5 \cdot 10^{-6} \frac{1}{^\circ C}$

Following procedure is applied to calculate the laminate CTEs from lamina CTEs.

1. Transform lamina CTEs from local coordinate system into global coordinate system

2. Calculate strains in global coordinate system due to thermal loading according to classical lamination theory

3. Set $\Delta T = 1$ and obtain CTEs for multidirectional laminate in global coordinate system

The composite books Gibson (2007) or Daniel and Ishai (2006) can be used as a reference to derive laminate CTEs equations.

The lamina CTEs can be transformed to the global coordinate systems as shown in Equation 3.43.

$$\left\{ \begin{array}{c} \alpha_x \\ \alpha_y \\ \alpha_{xy}/2 \end{array} \right\}_k = [T]_k^{-1} \left\{ \begin{array}{c} \alpha_1 \\ \alpha_2 \\ 0 \end{array} \right\}_k \tag{3.43}$$

where $[T]_k$ is given by Equation 3.44.

$$[T]_k = \left[\begin{array}{ccc} cos^2\theta & sin^2\theta & 2cos\theta sin\theta \\ sin^2\theta & cos^2\theta & -2cos\theta sin\theta \\ -cos\theta sin\theta & cos\theta sin\theta & cos^2\theta - sin^2\theta \end{array} \right]_k \tag{3.44}$$

For an orthotropic lamina, the following stress and strain relation applies (Gibson (2007)) as expressed in Equation 3.45.

$$\left\{ \begin{array}{c} \varepsilon_x \\ \varepsilon_y \\ \gamma_{xy} \end{array} \right\}_k = \left[\begin{array}{ccc} \bar{S}_{11} & \bar{S}_{12} & \bar{S}_{16} \\ \bar{S}_{12} & \bar{S}_{22} & \bar{S}_{26} \\ \bar{S}_{16} & \bar{S}_{26} & \bar{S}_{66} \end{array} \right]_k \left\{ \begin{array}{c} \sigma_x \\ \sigma_y \\ \sigma_{xy} \end{array} \right\}_k + \left\{ \begin{array}{c} \alpha_x \\ \alpha_y \\ \alpha_{xy} \end{array} \right\}_k \Delta\vartheta \tag{3.45}$$

If only thermal loads are present, the following is true (see Equation 3.46).

$$\left\{ \begin{array}{c} \varepsilon_x^\vartheta \\ \varepsilon_y^\vartheta \\ \gamma_{xy}^\vartheta \end{array} \right\}_k = \left\{ \begin{array}{c} \alpha_x \\ \alpha_y \\ \alpha_{xy} \end{array} \right\}_k \Delta\vartheta \tag{3.46}$$

The thermal stresses introduced by these thermal strains are given by Equation 3.47.

$$\left\{ \begin{array}{c} \sigma_x^\vartheta \\ \sigma_y^\vartheta \\ \sigma_{xy}^\vartheta \end{array} \right\}_k = \left[\bar{Q}\right]_k \left\{ \begin{array}{c} \varepsilon_x^\vartheta \\ \varepsilon_y^\vartheta \\ \gamma_{xy}^\vartheta \end{array} \right\}_k \tag{3.47}$$

where the coefficient matrix $\bar{Q}$ is shown in Equation 3.48.

$$\left[\bar{Q}\right]_k = \left[\begin{array}{ccc} \bar{Q}_{11} & \bar{Q}_{12} & \bar{Q}_{16} \\ \bar{Q}_{12} & \bar{Q}_{22} & \bar{Q}_{26} \\ \bar{Q}_{16} & \bar{Q}_{26} & \bar{Q}_{66} \end{array} \right]_k \tag{3.48}$$

By applying CLT, the thermal forces N^{ϑ} and thermal moments M^{ϑ} are obtained by Equations 3.49 and 3.50, respectively.

$$\begin{aligned}\left\{N^{\vartheta}\right\} &= \int \left\{\sigma^{\vartheta}_{xyz}\right\}_k \, dz = \int \left[\bar{Q}\right]_k \left\{\alpha_{xyz}\right\}_k \Delta\vartheta \, dz \\ &= \Delta\vartheta \sum_{k=1}^{N} \left[\bar{Q}\right]_k \left\{\alpha_{xyz}\right\}_k (z_k - z_{k-1}) \end{aligned} \tag{3.49}$$

$$\begin{aligned}\left\{M^{\vartheta}\right\} &= \int \left\{\sigma^{\vartheta}_{xyz}\right\}_k \, z \, dz = \int \left[\bar{Q}\right]_k \left\{\alpha_{xyz}\right\}_k \Delta\vartheta \, z \, dz \\ &= \frac{\Delta\vartheta}{2} \sum_{k=1}^{N} \left[\bar{Q}\right]_k \left\{\alpha_{xyz}\right\}_k \left(z_k^2 - z_{k-1}^2\right) \end{aligned} \tag{3.50}$$

Thermal forces N^{ϑ} and thermal moments M^{ϑ} can be expressed in terms of thermal strains $\varepsilon^{0,\vartheta}$ and thermal curvature κ^{ϑ} (see Equation 3.51).

$$\left\{ \begin{array}{c} N^{\vartheta} \\ M^{\vartheta} \end{array} \right\} = \left[\begin{array}{cc} A & B \\ B & D \end{array} \right] \left\{ \begin{array}{c} \varepsilon^{0,\vartheta} \\ \kappa^{\vartheta} \end{array} \right\} \tag{3.51}$$

By inverting Equation 3.51, Equation 3.52 is obtained.

$$\left\{ \begin{array}{c} \varepsilon^{0,\vartheta} \\ \kappa^{\vartheta} \end{array} \right\} = \left[\begin{array}{cc} A & B \\ B & D \end{array} \right]^{-1} \left\{ \begin{array}{c} N^{\vartheta} \\ M^{\vartheta} \end{array} \right\} \tag{3.52}$$

If only thermal strains are present, the laminate strains $\varepsilon^{0,\vartheta}$ can be expressed as given by Equation 3.53.

$$\left\{ \begin{array}{c} \varepsilon_x^{0,\vartheta} \\ \varepsilon_y^{0,\vartheta} \\ \gamma_{xy}^{0,\vartheta} \end{array} \right\} = \left\{ \begin{array}{c} \bar{\alpha}_x \\ \bar{\alpha}_y \\ \bar{\alpha}_{xy} \end{array} \right\} \Delta\vartheta \tag{3.53}$$

If the temperature difference, $\Delta\vartheta$, is set to 1, the laminate CTEs, $\bar{\alpha}$, are given by Equation 3.54.

$$\left\{\bar{\alpha}\right\} = \left\{\varepsilon^{0,\vartheta}\right\} \tag{3.54}$$

3.7.3 Validation

The CTEs calculation is validated in this subsection.

For a 0° angle-ply laminate, the laminate coefficient of thermal expansion $\bar{\alpha}_{xx}$ and $\bar{\alpha}_{yy}$ should be equal to the lamina coefficient of thermal expansion α_{11} and α_{22}, respectively. Also, for a 90° angle-ply laminate the laminate CTE $\bar{\alpha}_{xx}$ and

$\bar{\alpha}_{yy}$ should be equal to the lamina CTE α_{22} and α_{11}, respectively. Additionally, the laminate CTE $\bar{\alpha}_{xy}$ must be zero for an angle-ply laminate.

The validation plot shown Figure 3.20 is obtained by using the same material properties as in the example 7.9 on page 307 in Gibson (2007) and a ply-thickness of $0.25mm$. The lamina coefficient of thermal expansion is $\alpha_{11} = 0.88 \cdot 10^{-6} \frac{1}{^\circ C}$ and $\alpha_{22} = 31 \cdot 10^{-6} \frac{1}{^\circ C}$, respectively.

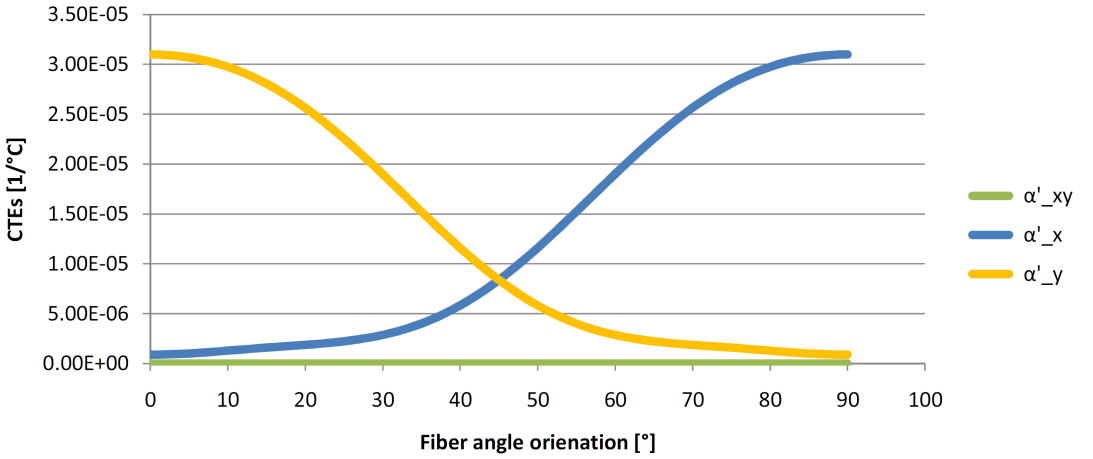

Figure 3.20: Validation: CTEs for angle-ply laminate where $\alpha'_{ij} = \bar{\alpha}_{ij}$

It can be seen that for a 0° angle-ply laminate $\bar{\alpha}_{xx} = \alpha_{11}$, $\bar{\alpha}_{yy} = \alpha_{22}$ and for a 90° angle-ply laminate $\bar{\alpha}_{xx} = \alpha_{22}$, $\bar{\alpha}_{yy} = \alpha_{11}$. Also, $\bar{\alpha}_{xy}$ is 0 for any fiber angle orientation.

In addition to this validation, the CTE calculation is verified by carrying out the calculation in example 7.9 on page 307 in Gibson (2007). Results match exactly and are not shown here.

3.7.4 Critical Value

Since only the driveshaft is to be replaced by a composite material, the tailboom is still manufactured from aluminum. Even for relatively low temperature difference $\Delta\vartheta$, relatively high axial force can develop. This is due to the fact, that aluminum has typically a CTE of $\alpha_{alu} = 24 \cdot 10^{-6} \frac{1}{^\circ C}$ whereas for composite the axial CTE α_{xx} can even be negative. In order to limit this thermal expansion difference between the tailboom and driveshaft, the composite axial CTE should be limited to a range between $+3^\circ C$ and $-3^\circ C$ of the CTE of aluminum. This leads to following lower and upper limits for the axial laminate CTE α_{xx}=$[21 \cdot 10^{-6} \frac{1}{^\circ C}, 27 \cdot 10^{-6} \frac{1}{^\circ C}]$.

It is shown in Subsection 5.2.2 that a CTE constraint is extremely restrictive and is therefore not embedded within the structural model for the optimization. However, this axial displacement has to be accounted for by an appropriate end-fitting design of the driveshaft.

3.8 Conclusion

The most important assumptions and the capabilities of the structural model are discussed in this section.

Since buckling and critical speed calculation is only valid for thin-walled tubes, the entire structural model is only valid for thin-walled driveshaft. A shaft with a wall thickness less than 10% of the outer radius ((r_o/t_{wall})-ratio of 10) is considered as being thin. Considering a fixed outer radius r_o, the inner radius is not to be lower than $r_{i_min} = 0.9 \cdot r_o$. This restriction defines the maximum number of plies in the laminated shaft to be used within its optimization.

Also, the length, measured between two support bearings, to thickness ratio of the shaft is to be higher than 15 to fulfill the assumption of a long shaft. Otherwise, boundary conditions within the buckling calculation should not be neglected.

To sum up, the structural model is capable of calculating the maximum temperature in a rotating, misaligned driveshaft. A temperature- and frequency-dependent material behavior is assumed for all analysis. Critical lamina ply-level stresses and strains are calculated so that a failure due to overload can be avoided. Furthermore, the critical speed by which the spinning shaft reaches its first natural frequencies is determined. Also, the buckling torque is calculated by which the shaft becomes structurally unstable. Failure criteria were formulated and appropriate safety factors defined. Additionally, it was tried to minimize computation time which enables the driveshaft optimization tool to be executed faster. All sub-models of the structural model were successfully validated which gives confidence in the correctness of the entire model.

Chapter 4

Optimization of Driveshaft

4.1 Introduction

The structural model is embedded within an optimization routine to find a feasible solution[1] and minimum-weight solution for a helicopter driveline. In this approach to find an optimal shaft design, the stacking sequence, the number of plies and the number of bearings can be varied. For manufacturing and simplicity reasons, discrete values for fiber angle orientations are to be chosen. This implies that each layer of the composite shaft is restricted to a predefined set of fiber orientations (see Section 4.2). Consequently, this optimization problem is referred to as a so-called discrete optimization problem. The optimization process is carried out in a two-level approach to reduce complexity and computation time.

On the first level, an optimum solution is calculated for a constant set of bearings and plies where the stacking sequence, using discrete fiber orientations, is to be altered. Genetic algorithms are known to be suitable for this sort of problems. In the following a genetic algorithm approach is employed to find the best stacking sequence for a given number of plies and bearings. The selection of optimization parameters such as population size and the way to generate the offspring is crucial to find a good trade-off between computation time and obtaining the "best" solution (see Subsection 4.3.5). Nevertheless, there is no guarantee that the optimum solution is found in a genetic algorithm. This optimization algorithm is explained in Section 4.3.

On the second level, the number of bearings and plies is varied, too. By applying sequential calculations for a specific set of bearings and plies, the overall optimal minimum-weight solution for a driveshaft is found. This model is referred to as *optimization model* in the following and is explained in Section 4.4.

[1] A feasible solution is defined as a solution that satisfies all constraints given by the failure criterion of self-heating, critical speed, buckling torque and stress and strain calculation.

4.2 Design Variables

Not only is the optimization algorithm itself of highest importance to find good solutions but also the selection of variables which can be changed within the model during the optimization. These variables are known as design variables of the model and their selection also affects the entire writing of an optimization code to a high extent. Therefore, it is crucial to carefully select these variables.

For this optimization problem, following design parameters are selected for the optimization model.

- Fiber angle orientation (incremental steps of 15°): θ=15°, θ=30°, θ=45°, θ=60° and θ=75°. Due to manufacturing constraints of filament-winding, θ=0° and θ=90° cannot be employed, θ=10° and θ=88° are used instead. Since the driveshafts are manufactured by winding helical plies, there is always a $+\theta$ and $-\theta$ fiber orientation (see Section 3.1).

- Stacking sequence, starting from the inner radius of the shaft: (θ_1/-θ_1/θ_2/-θ_2/.../θ_k/-θ_k)

- Number of plies whereas the maximum number to be used is restricted so that the shaft's wall thickness is small compared to its radius (minimum (r_o/t_{wall})-ratio of 10): n_l

- Number of mid-span bearings: n_b

The thickness t_i of one ply for filament-winding is selected to be $0.25mm$. The lamina/laminate density $\rho_L = 1489\frac{kg}{m^3}$ for LF750D/AS4D is calculated by the rule of mixture.

In the following analysis, a Blackhawk and Chinook helicopter driveline is investigated and the properties are shown in Tables 4.1[2] and 4.1.

Table 4.1: Sikorsky UH-60 Blackhawk helicopter driveline properties (Mayrides (2005))

Blackhawk driveline properties:	
Total shaft length:	L_S = 7.544 m
Outer radius:	r_o = 0.04445 m
Mid-span bearing weight:	m_b = 3.84 kg
Operation speed:	f_{op} = 4116 rpm = 68.6 Hz
Applied torque:	T_{op} = 734 Nm
Operating power:	P = 316 kW
Driveline weight:	m_D = 31.3 kg

[2]The power is calculated by $P = \omega \cdot T = 2 \cdot \pi \cdot f \cdot T$

Considering a Blackhawk driveshaft, the maximum total number of plies is $n_p = 14$ ($=\frac{r_o - r_i}{t_i}$) and the number of different fiber orientations n_θ is seven. Assuming a constant number of bearings and constant number of plies, a full enumeration would leads to $\left(\frac{n_p}{2}\right)^{n_\theta} = 7^7 = 823'543$ different solutions. Furthermore, the average time to calculate one solution requires 15 seconds. Consequently, a full enumeration would take more than 142 days (!). Thus, it is obvious that an optimization procedure is required to solve this problem efficiently.

Table 4.2: Boeing CH-47 Chinook helicopter driveline properties (Mayrides (2005))

Chinook driveline properties:	
Total shaft length:	$L_S = 8.598$ m
Outer radius:	$r_o = 0.05715$ m
Mid-span bearing weight:	$m_b = 5.20$ kg
Operation speed:	$f_{op} = 6912$ rpm $= 115.2$ Hz
Applied torque:	$T_{op} = 4067$ Nm
Operating Power:	$P = 2983$ kW
Driveline weight:	$m_D = 60.1$ kg

For a Chinook driveshaft the maximum number of ($\pm$)-plies to obtain a thin-wall design is 11. Since computation time of the structural model is mainly driven by the number layers, a larger outer diameter and therefore thicker maximum shaft's wall thickness increases computation time. A full enumeration would leads to $\left(\frac{n_p}{2}\right)^{n_\theta} = 7^1 1 = 1.9773 \cdot 10^9$ different solutions. This would take more than 1270 years (!) if a computation time of 20 seconds per run is assumed.

It is crucial to distinguish between the optimization model and the optimization algorithm. The optimization algorithm employed in this work is a genetic algorithm and is part of optimization model. Herein, the number of bearings and the number of plies is kept constant. The stacking sequence can be altered only. Within the optimization model, however, the number of bearings and the number of plies can change, too.

In the following Section 4.3, the optimization algorithm, genetic algorithm, is presented.

4.3 Optimization Algorithm

4.3.1 Terminology

A genetic algorithm is based on the idea of natural selection, the survival of the fittest by Darwin's principle. At each step, GA selects individuals to be parents which generate children for the next generation. Ideally, a better and

better solution is achieved over successive generations. More information on evolutionary algorithms can be found in optimization books such as Goldberg (1989).

In the following, the most important terminological terms are explained briefly.

- **Fitness function**
  This is the objective function, the function which is to be minimized during the optimization.
- **Individual**
  Also known as Genome, this is one point in the search space to which a fitness function can be addressed to.
- **Genes**
  These are the entries of an individual. Here, the genes are the layup stacking sequence and the number of bearings.
- **Score**
  This is the fitness function's value of one individual.
- **Population**
  A group of individuals is called population. Herein, same individuals can appear more than once in a the same population.
- **Generation**
  This is the number of populations that are executed during the optimization algorithm.
- **Parents**
  To create a new generation, individuals are selected to be parents. This is done by a parent selection function which is based on their fitness function values.
- **Children**
  Offspring generated through crossover of parents, mutation and cloning of current population to form a new population.
- **Elite Children**
  When generating the off-spring, the best individuals with the least score in the current population are directly transferred to the next generation. This process is also known as cloning of the parents and the children are referred to as elite children.
- **Crossover**
  Crossover is a way to generate off-spring from two individuals, the so-called parents, within the population. The crossover child inherits part of its genes from parent 1 and the other part from parent 2 (see Subsection 4.3.4).

- **Mutation**
  Mutation is another way to generate children for a new generation. Only one parent is required which passes down part of its genes to the mutation child (see Subsection 4.3.4).

4.3.2 Problem Statement

As mentioned above, the number of plies and number of bearings are kept constant within the optimization algorithm.

Since a feasible solution of the optimization algorithm has to fulfill several constraints such as not exceeding a maximum ply-stress, this optimization problem is referred to as a constraint optimization problem. Such a problem can be represented as shown in Equation 4.1.

$$\begin{aligned} &min\ f(\mathbf{x}) \\ &g_i(\mathbf{x}) \leq 0 \end{aligned} \tag{4.1}$$

where $f(\mathbf{x})$ is the objective function, $\mathbf{x} = \{\pm\theta_1, \pm\theta_2, .., \pm\theta_n, n_b\}$ is a vector containing the stacking sequence, the number of bearings and the inequality constraining functions $g_i(\mathbf{x})$ are given by Equation 4.3.

A constrained optimization problem, as shown in Equation 4.1, can be transformed into an unconstrained one. One method is to utilize a penalty method which is also explained in the lecture-class script by Kress and Keller (2007). Here, the so-called exterior point penalty function is applied (see Equation 4.2). The function $p(\mathbf{x})$ is called a pseudo objective function and is the new function to be minimized.

$$\begin{aligned} min\ p(\mathbf{x}) &= f(\mathbf{x}) + \Omega(\mathbf{x}, R) = f(\mathbf{x}) + \sum_{k=1}^{n} \{max[0, g_i(\mathbf{x})]\}^2 \\ &= f(\mathbf{x}) + R \cdot [max(0, g_1(\mathbf{x}))^2 + max(0, g_2(\mathbf{x}))^2 + max(0, g_3(\mathbf{x}))^2 \\ &\quad + max(0, g_4(\mathbf{x}))^2 + max(0, g_5(\mathbf{x}))^2] \end{aligned} \tag{4.2}$$

where the constraining functions g_i are given by Equation 4.3. $\Omega(\mathbf{x}, R)$ is the penalty function and R is the penalty factor and is selected to be 10^4. The function value of g_i is negative if the i^{th} criterion is fulfilled and positive if it is not.

$$
\begin{aligned}
g_1(\mathbf{x}) &= -\frac{\vartheta_{ult}}{\vartheta_{S,max}(\mathbf{x})} \cdot \frac{1}{S_{f,h}} - 1 \\
g_2(\mathbf{x}) &= -\frac{T_{b,crit}(\mathbf{x})}{T_{op}} \cdot \frac{1}{S_{f,b}} - 1 \\
g_3(\mathbf{x}) &= -\frac{f_{crit}(\mathbf{x})}{f_{op}} \cdot \frac{1}{S_{f,w}} - 1 \\
g_4(\mathbf{x}) &= -\left(\frac{\varepsilon_{ij,ult}}{\varepsilon_{ij,max}(\mathbf{x})}\right)_{min} \cdot \frac{1}{S_{f,s}} - 1 \\
g_5(\mathbf{x}) &= -\left(\frac{\sigma_{ij,ult}}{\sigma_{ij,max}(\mathbf{x})}\right)_{min} \cdot \frac{1}{S_{f,s}} - 1
\end{aligned} \tag{4.3}
$$

It is to be noted that this problem could also be referred to as a five-constraints problem since weight of the driveline[3] remains the same within one execution of the genetic algorithm. Having mentioned that, the function $f(\mathbf{x})$ could also be chosen to be zero. However, this is not done here since one can compare solutions found within the optimization model easier this way.

As mentioned above, the function f is constant within one execution of the model. In order to distinguish between feasible solutions, where the penalty function $\Omega(\mathbf{x}, R) = 0$ is equal to zero, an additional criterion is required. It is utterly important to point out that this criterion is only employed if, and only if, a solution is feasible. This is done as shown in Equation 4.4. By definition, the factors g_i are negative for feasible solutions and therefore the function value $p\mathbf{x})$ in Equation 4.4 is always lower than $f(\mathbf{x})$. By applying this additional criterion, a solution which has the highest overall margin of safety is regarded as being the optimal solution.

$$
\begin{aligned}
min\ p(\mathbf{x}) &\equiv min\ p(\mathbf{x}) + \sum_{k=1}^{n} g_i(\mathbf{x}) \\
&= min\ p(\mathbf{x}) + g_1(\mathbf{x}) + g_2(\mathbf{x}) + g_3(\mathbf{x}) + g_4(\mathbf{x}) + g_5(\mathbf{x})
\end{aligned} \tag{4.4}
$$

MATLAB R2009b provides a genetic algorithm optimization function which works well for continuous optimization problems. For discrete optimization problems, this MATLAB function can also be employed but requires several user input functions. This function is applied in this driveshaft optimization and is explained in the following subsection.

4.3.3 How it works - Procedure

The procedure of the genetic algorithm applied to this optimization problem is presented below.

[3]The driveline weight is equal to the driveshaft weight and the mass of the mid-span bearings.

1. **Generate Initial Population:**
   To start the algorithm, an initial population is required. In the present case, this population is generated randomly by a user-input function. The size of the population is to be defined by the user and is kept constant within the a run of the algorithm. On the one hand, a large population size enables the algorithm to search a large solution space and obtain a good solution. On the other hand, computation time heavily depends on the size of the population. Therefore, this population size should be selected carefully.

2. **Calculate Fitness of Individuals:**
   After running the structural model, the fitness function value, score, of an individual can be calculated. This is to be done for every individual within the current generation.

3. **Fitness Scaling of Individuals:**
   Raw fitness values are sorted so they are more suitable for the selection of parents for the next generation. Here, a rank-based sorting method is applied where the fittest individual is 1, the second fittest 2 and so on. By applying this scaling method, the effect of spread of raw scores is removed. It is to be noted that many other fitness scaling methods can be found in literature.

4. **Selection of Parents to Generate New Population:**
   Parents for the next generation are chosen according to their scaled fitness function value. In the present case, a stochastic uniform selection is used. Parents are selected based on their probability which is higher, the lower their fitness function value is. Alternative selection methods exist such as "roulette-selection" or "tournament-selection".

5. **Generate New Generation:**
   A new generation is generated by elite children, crossover and mutation. First, a user-defined number of elite children are selected which form the first individuals of the next generation. Having done this, the rest of new population is generated by applying crossover and mutation (see Subsection 4.3.4). Herein, additional user-defined parameters need to be defined (see Subsection 4.3.5). Having generated a new population of the same size as the last generation, the algorithm starts from beginning as long as no stopping criterion is met.

6. **Stopping Condition:**
   A stopping criterion is a condition that stops the genetic algorithm. This can be the case if for instance the maximal number of generations is exceeded or the the algorithm has converged.

7. **Final solution of Optimization Algorithm:**
   The final solution of the algorithm is the best individual of the last popula-

tion. This is the optimal solution found during the optimization algorithm for a constant number of bearing and constant number of layers.

A flow chart for the optimization algorithm is shown in Figure 4.1. To sum up, after generating an initial population, the structural model is executed for each individual of the population and the fitness is calculated. Afterwards, a fitness scaling is applied and the parents are selected. A new population is generated and the algorithm is executed again until one stopping criterion is reached. The individual with the stacking sequence that leads to lowest fitness function value is the final solution of the optimization algorithm.

Every solution is saved in a look-up table. Before running the structural model for a given layup stacking sequence, it is checked if this solution has already been calculated earlier. This look-up table is embedded within the optimization algorithm to omit the calculation of exact same individuals. This improves the speed of the algorithm and reduces computation time of the optimization model which is presented in the following Section 4.4.

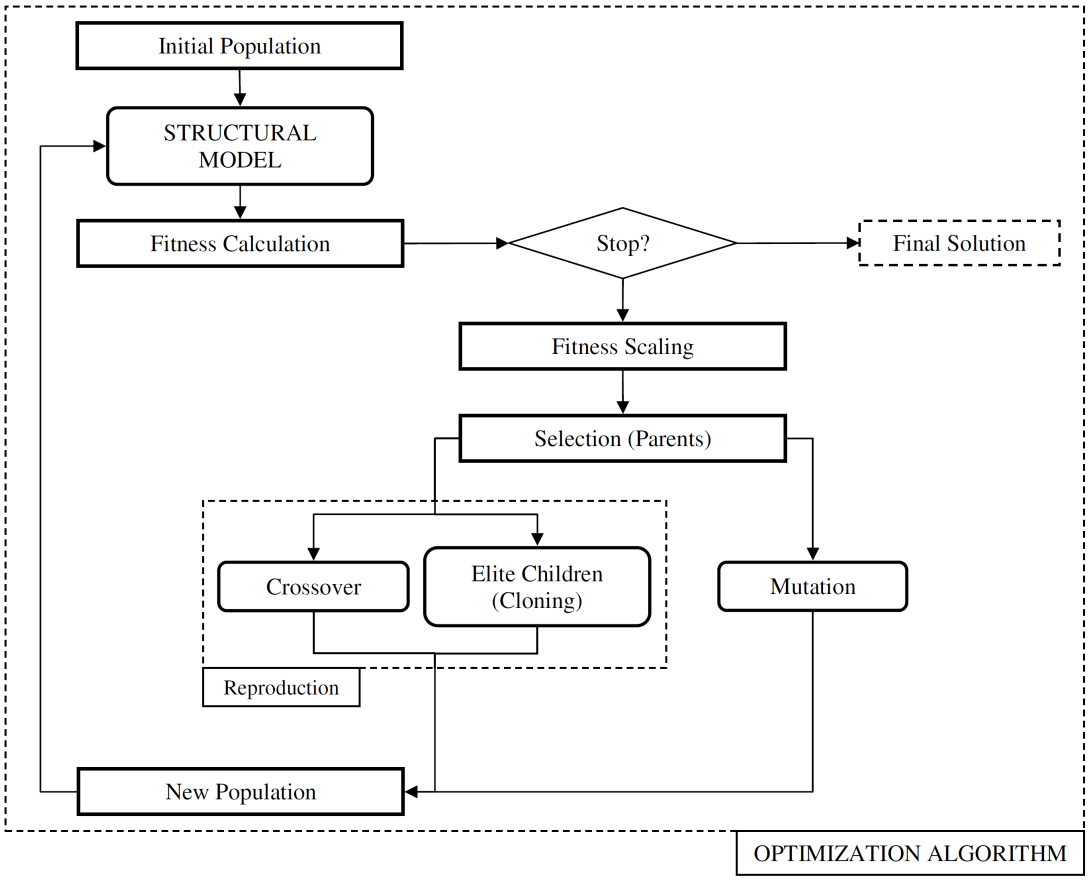

Figure 4.1: Flow chart - Optimization algorithm

4.3.4 Crossover and Mutation

Many different ways to perform crossover and mutation are found in literature.

Crossover requires two parent individuals. The mutation child inherits genes from both parents. In this work, the number of genes that are inherited from parent 1 and parent 2, respectively, is selected randomly. For every gene, a random number between 0 and 1 is generated. Starting point is the first gene of parent 1 and parent 2. If that random number is smaller than 0.5, the current gene from parent 1 is selected to be the gene of the child. If the number is larger than 0.5, the current gene of parent 2 is selected. Applying the same procedure for all genes, a child with the same number of genes as their parents is obtained. Alike children generated by crossover are tried to be avoided by two measures. First, the crossover by using the same two parents is repeated. Since, the selection of genes is done randomly, a different child is likely to occur. However, the variety within a population typically decreases towards the convergence of the algorithm. A second measure might now be required, a different parents combination is selected until a different crossover child is obtained. In extremely few cases, same crossover children may still exist if the population variety is not large enough. It has observed during this work, that avoiding same crossover children enables the algorithm to find better solutions since the variety in the population is bigger. The amount of crossover is defined by the crossover fraction which is a user-input. A crossover fraction of 1 suggests that generating children is done by crossover only and no mutation. If a crossover fraction of 0 is chosen, mutation is performed only.

Mutation requires only one single parent. Part of the genetic code of this parent is handed down to the mutation child. The number of genes which are not inherited by the parent is defined by the mutation rate. A mutation rate of 1 implies that no genes are handed down from the parent to its child whereas a mutation rate of 0 means that parent and child are alike. After the mutation rate is defined, the positions of the genes to be changed are selected which is done randomly. Also, the new mutation gene is generated randomly by choosing one of the possible fiber angle orientations. Alike mutation children can be avoided by re-running the mutation of this parent if two children. Unless the mutation rate is 0, which implies that parent and child are alike, different mutation children can always be obtained in the current optimization problem. The mutation rate can be changed over generations. At the beginning, a large mutation rate should be chosen so that a wide range of the design solution space can be explored. Once the algorithm progresses, searching for good solutions should be more localized and a smaller mutation rate is recommended. This helps finding the best solution more often and makes the algorithm more reliable. It is shown in Subsection 4.3.5 that changing the mutation rate over generation yields to better results than keeping it constant.

Selecting a best-possible crossover fraction and mutation rate is not straight forward but crucial to enable the algorithm to find good solutions. These pa-

rameters are to be identified in the course of parameter studies (see Subsection 4.3.5).

4.3.5 Parameters for Genetic Algorithm

One characteristic of genetic algorithms is the large amount of input parameters that this optimization technique requires. As mentioned in the previous subsection, parameters that are to be selected for the genetic algorithm are of highest importance in order to find a good solution. The population size, crossover fraction, number of elite children and mutation rate are to be determined to obtain a best possible result and make the optimization algorithm as robust as possible. This is done by a trial and error approach. Blackhawk driveshaft properties are used due to computation time reasons.

The parameters population size, crossover fraction and mutation rate influence each other by finding the best solution. A large population size can be avoided by selecting good values for crossover fraction and mutation rate. The identification of optimal parameters to be used within the optimization algorithm is done after several different configurations as shown for instance in Figures 4.2, 4.3, 4.4 and 4.5.

The population size is selected to be 40 and was chosen based these parameter study on population size and crossover fraction. The stall generation, the convergence criterion used here, is 10. This means that the algorithm stops if the minimum function value is not improved within the last 10 generations. By a similar approach, the number of elite children was selected to be 4. The maximum number of generations to be executed is 40.

In the Figures 4.2, D.1, D.2, D.3 and 4.5 mutation rate is kept constant whereas in the Figures D.5, D.6, D.7, D.8, D.9, 4.3, 4.5, D.10, 4.4, D.11 and D.12 the mutation rate is decreases with the number of generations. On the vertical axis, the crossover fraction is shown and on the horizontal axis the minimum fitness function value found during the optimization is shown. Each point represents the execution of one run of the optimization algorithm. The number of elite children is four and the population size 40. The optimization algorithm is run five times for every crossover fraction.

The larger the mutation rate, the higher the randomness in the optimization algorithm. If the mutation rate is too low, the design space is searched very locally and the final optimum solution heavily depends on the initial population of the algorithm. Reducing the mutation rate factors over the number of generations enables the algorithms to find better solutions compared to a fixed mutation rate factor. A crossover fraction of 0.5 and a mutation rate of 0.7 for the first population is used and is linearly decreased to 0.2. A mutation rate of 0.2 would be used if the maximum number of generations was reached. By applying this varying mutation rate factor, the optimal solution is found relatively reliable. It is to be mentioned again that there is never a 100% guarantee of finding the optimal

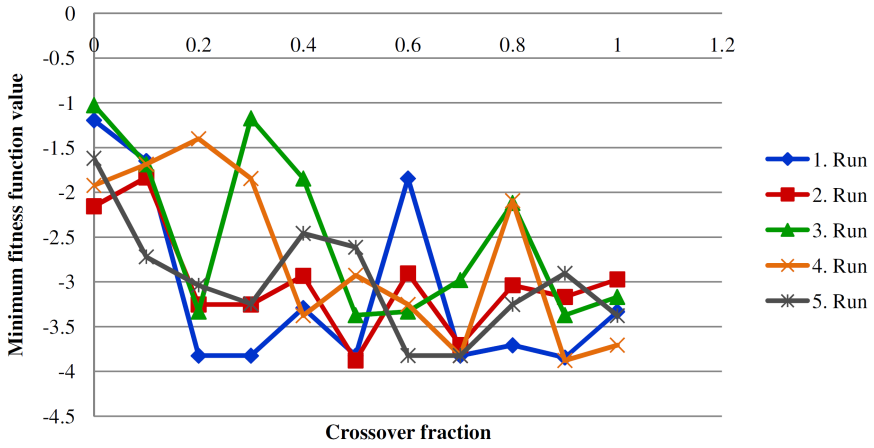

Figure 4.2: Study: Crossover fraction and constant mutation rate, 0.5

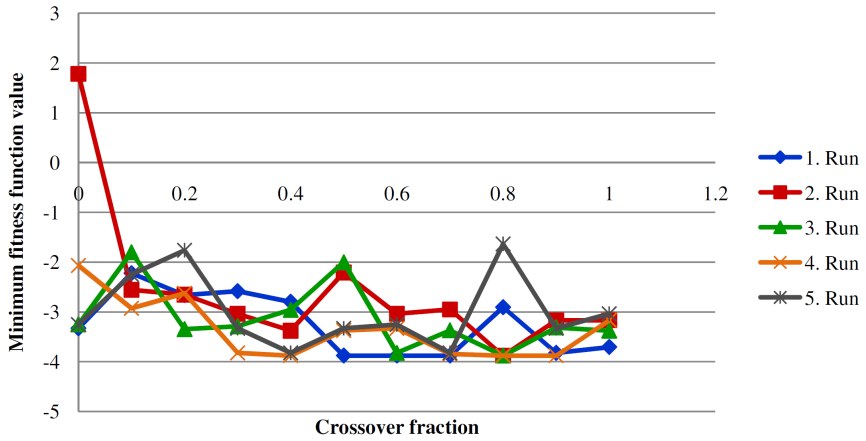

Figure 4.3: Study: Crossover fraction and varying mutation rate of 0.7-0.3

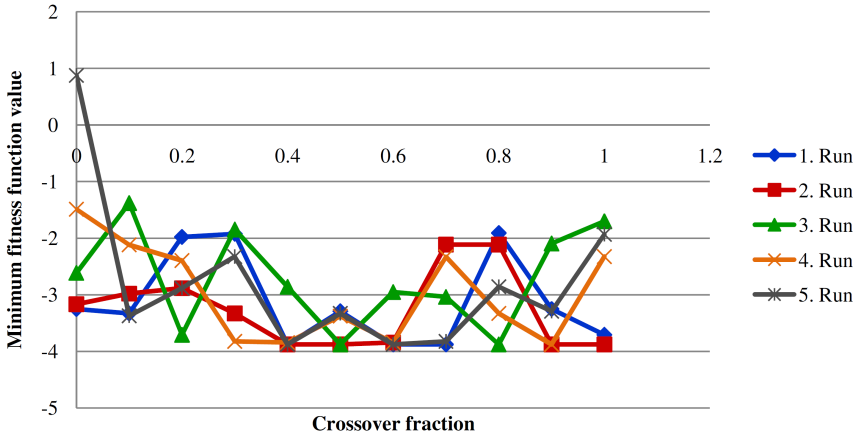

Figure 4.4: Study: Crossover fraction and varying mutation rate of 0.7-0.2

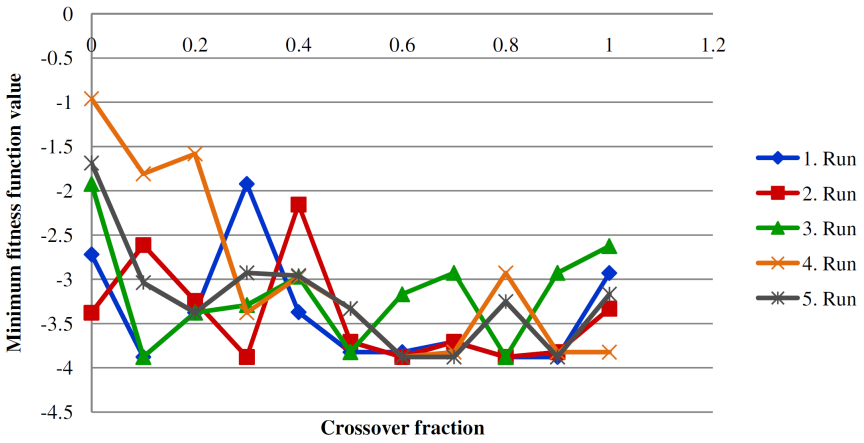

Figure 4.5: Study: Crossover fraction and varying mutation rate of 0.7-0.1

solution in every run since a genetic algorithm is always driven by randomness to a certain extent.

4.4 Optimization Model

The optimization model allows the optimization of stacking sequence, number of plies and number of bearings. A flow chart of the optimization procedure is shown in Figure 4.6.

In a first loop, the minimum number of bearings for the maximum number of plies is identified. If one feasible solution is found, the optimization algorithm is stopped immediately to reduce computation time. At this stage, the best solution is not of interest since the minimum number bearings and layers has not been identified yet. This measure allows avoiding unnecessary calculations and lowers the computation time drastically. If, however, no feasible solution is found, the algorithm is executed once again. This measure minimized the risk of missing a feasible solution for a lower number of bearings.

Afterwards, the minimum number of plies for the minimum number of bearings is identified in a second loop. Also, the algorithm is stopped after one feasible solution is found. Additionally, the calculation is repeated once if no feasible solution is found as this is done in the in the first loop.

It is to be noted that, theoretically, lighter solutions might exist by applying the optimization procedure presented here. A lighter design might be found for a larger number of bearings for which a thinner driveshaft would fulfill all requirements. Practically, however, no such solutions are found here. An additional loop for a higher number of bearings, for which the minimum number of plies would have to be found, is not required.

Having identified the minimum number of bearings and the minimum number of plies, the optimization algorithm is executed again. This time, the algorithm

is not stopped after the fist feasible solution is found since the optimum stacking sequence among all solutions is to be found at this point. The algorithm only stops after a convergence criterion is met. The solution with the best stacking sequence for the minimum number of bearings and plies is obtained.

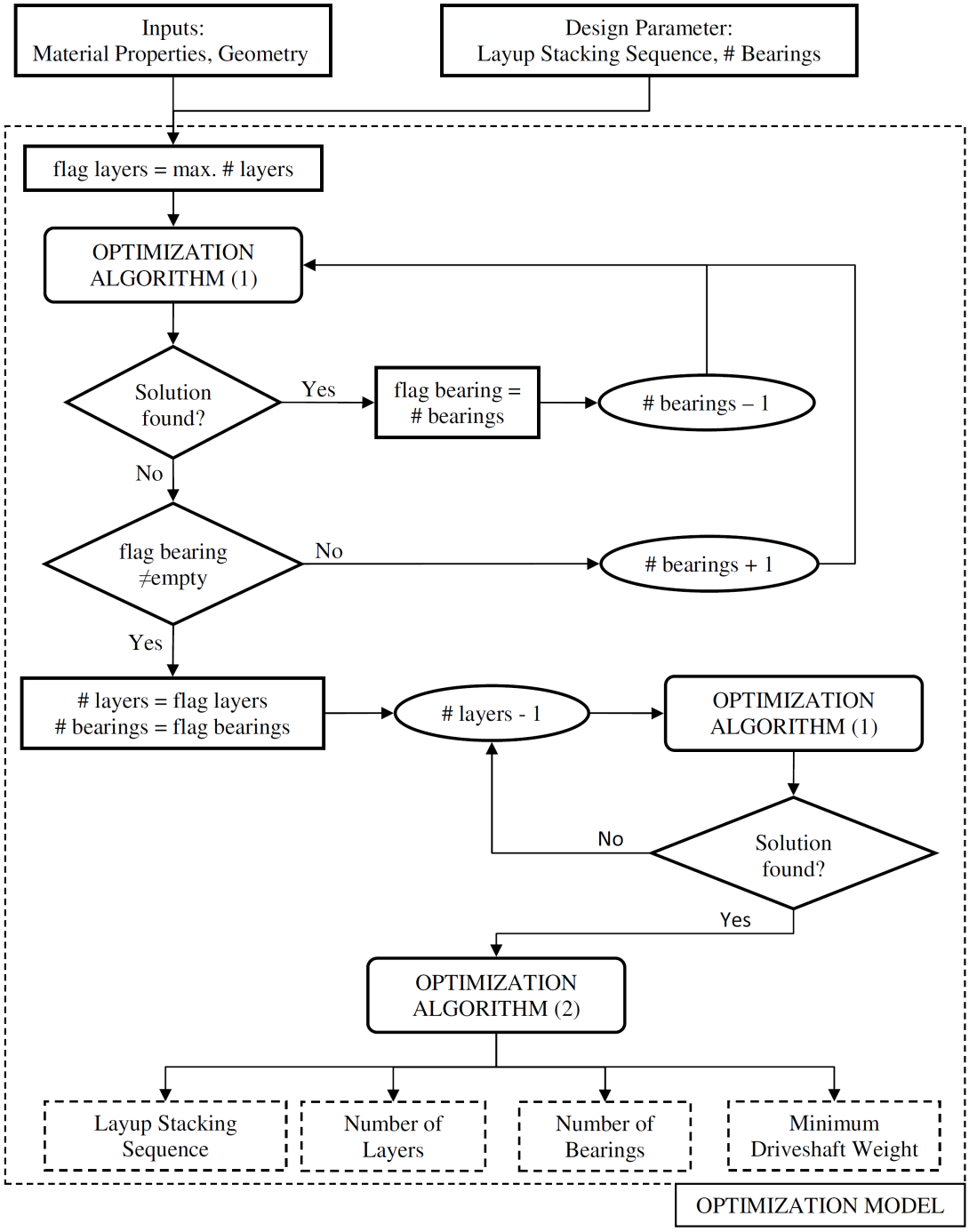

Figure 4.6: Flow chart - Optimization model of FMC driveshaft

4.5 Summary

The optimization model used to find a minimum-weight driveshaft design for the least amount of mid-span bearings is presented in this chapter. This model is capable of finding the minimum number of mid-span bearings, the minimum number of plies and the optimum layup stacking sequence for a minimum driveshaft weight. Constraints such as not exceeding maximum shaft temperature, critical speed, buckling torque, maximum allowable stress and strain are implemented within this model. A genetic algorithm is applied to solve the discrete optimization problem. Optimization parameters such as population size, crossover fraction, mutation rate and number of elite children are determined in a parameter study.

Chapter 5

Results

5.1 Overview

In this section, a primarily design study and results of the optimization model for a spinning, misaligned driveshaft are presented. Different loading cases and amounts of bending strain are considered within the optimization studies of the shaft to gain more insight into designing driveshafts. Frequency- and temperature-dependent material properties for LF750D/AS4D are utilized throughout the optimization. The outer diameter and the length of the shaft are fixed so that a metal driveshaft could be replaced by a FMC driveshaft by only making little changes.

Within the primarily design study (see Section 5.2), a Blackhawk helicopter driveline is assumed. In Section 5.3, an Blackhawk driveline is optimized. Various loading scenarios are looked at and discussed. Additionally, the effect misalignment on the optimal driveshaft solution is investigated. A Chinook driveshaft optimization problem is considered in Section 5.4. Different loading cases are examined. Blackhawk and Chinook optimization results obtained are compared to previous work done in this area.

5.2 Primarily Design Study for Angle-Ply Laminated Driveshafts

5.2.1 Results - Structural Model

A primarily design study for angle-ply laminates is carried out and presented in this section. Thereby, some insight into the dependence of fiber orientation on the analysis within structural model is to be obtained.

An angle-ply laminate with six $\pm\theta$ layers is assumed, the stacking sequence is given by $[\pm\theta]_6$. Material Properties for LF750/AS4D are used and four mid-span bearings were assumed along the shaft within this study.

In Figures 5.1, 5.2, 5.3, 5.4, 5.5, 5.6, 5.7 and 5.8 the red line and green line represent the critical value without and with a safety factor, respectively.

In Figure 5.1, the maximum temperature due to self-heating for an angle-ply laminated spinning and misaligned shaft is shown. The maximum shaft temperature needs to stay below the value represented by the green line. For fiber angle orientations of around 20°, very high temperatures can occur. Even though the behavior of a laminate might be quite different, it is likely that not many plies with a fiber angle-orientation of around 20° occur in a minimum-weight shaft design.

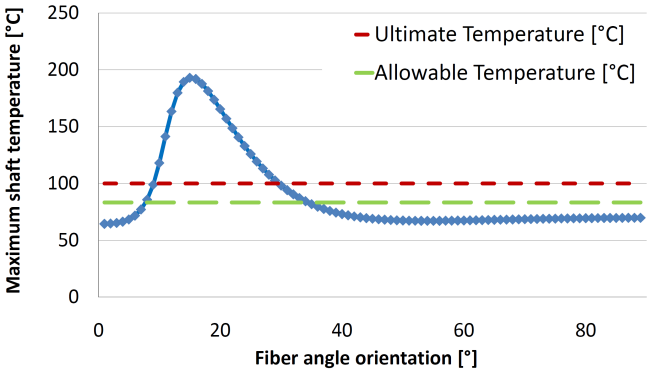

Figure 5.1: Parameter study: self-heating vs. angle of fibers in angle-ply shafts

The critical buckling torque for a driveshaft is shown in Figure 5.2. The buckling torque needs to be higher than the green line so that buckling does not occur. It can be seen that only angle-ply laminates with fiber orientations of around 40° and values close to 90° can fulfill this requirement. Low fiber orientations are to be avoided when a high buckling torque is needed.

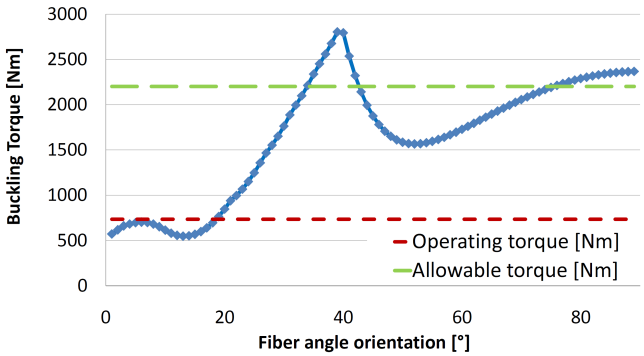

Figure 5.2: Parameter study: buckling torque vs. angle of fibers in angle-ply shafts

In Figure 5.3, the critical speeds are shown. The first natural frequency of the driveshaft, critical speed, needs to be above the green line so that whirling

instability can be avoided. Angle-ply laminates with low fiber angle orientation are beneficial with respect to avoiding whirling of the shaft. On the other hand, high fiber angle orientations are to be avoided since the axial stiffness is too low.

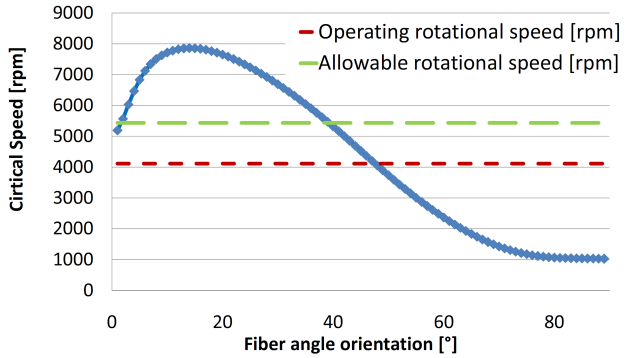

Figure 5.3: Parameter study: critical speed vs. angle of fibers in angle-ply shafts

In Figures 5.4, 5.5, 5.6, 5.7 and 5.8 lamina strains in 1-direction, 2-direction and shear strain in the 1-2 direction are shown. The green line represents the critical value that is not to be exceeded.

Figure 5.4 shows the maximum compressive strain in 1-direction. Low fiber orientations lead to a lot of strain and are to be avoided with respect to maximum compressive strain in 1-direction.

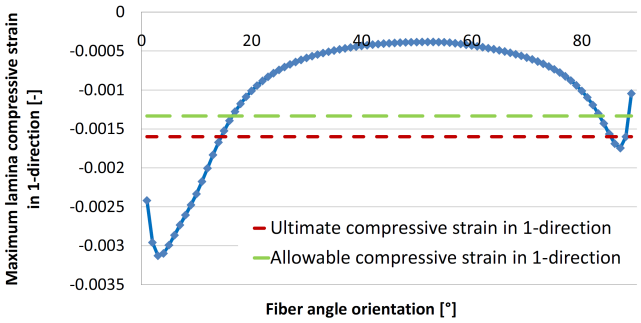

Figure 5.4: Parameter study: maximum lamina compressive strain in 1-direction vs. angle of fibers in angle-ply shafts

In Figure 5.5, maximum tensile strains in 1-direction are shown. The absolute value is the same as for compressive strain in this direction but the allowable maximum strain is much different. For this reason, tensile strain in 1-direction is not critical since compressive strain allowable in 1-direction is limiting for any angle-ply laminate.

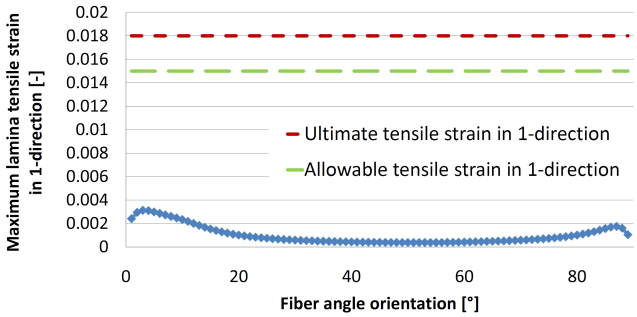

Figure 5.5: Parameter study: maximum lamina tensile strain in 1-direction vs. angle of fibers in angle-ply shafts

Maximum compressive strain in 2-direction are shown in Figure 5.6. Fiber angle orientations between around 40° and 70° are beneficial to avoid high strains in this direction. Here, strains in compression are not as critical as in 1-direction.

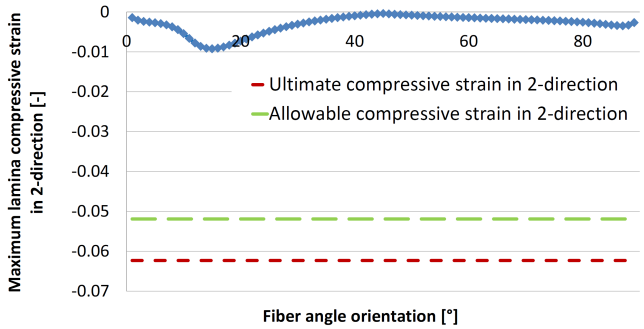

Figure 5.6: Parameter study: maximum lamina compressive strain in 2-direction vs. angle of fibers in angle-ply shafts

In Figure 5.7, the maximum tensile strains in 2-direction are shown. It is to be noted that the same value as in compression is obtained. Since the allowable tensile strain in 2-direction is lower than in compressive, tensile strain is critical in this case. This is the opposite as for strain in 1-direction for which compressive strain is critical.

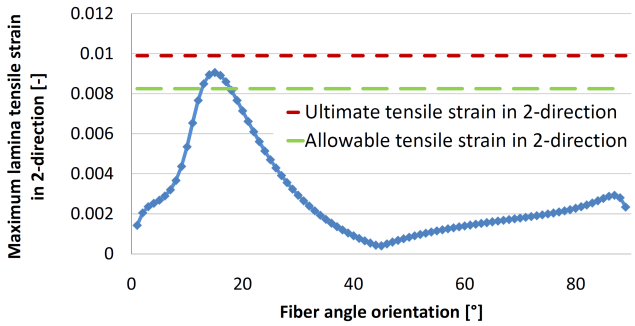

Figure 5.7: Parameter study: maximum lamina tensile strain in 2-direction vs. angle of fibers in angle-ply shafts

Absolute maximum shear strains in the 1-2 direction are shown in Figure 5.8. Angle-ply laminates with very low and also very high fiber angle orientations develop high shear strains and should therefore be avoided to obtain low shear strains.

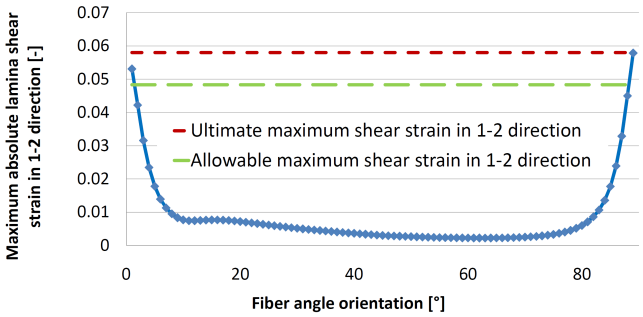

Figure 5.8: Parameter study: maximum lamina shear strain in 1-2 direction vs. angle of fibers in angle-ply shafts

In Appendix E in Figures E.1, E.2, E.3, E.4 and E.5, the effect of torque and bending on the strain calculation is shown. It can be concluded that in 1-direction, the effect from torque and bending loading are equally important for low fiber angle orientations but torque dominates for fiber orientations higher than 40°. In 2-direction, bending loading determines the maximum strain apart from fiber orientations around 45° and some small regions for very high and low fiber orientations. The maximum shear strain is dominated by torque loading for low and high fiber angle orientations and by bending for the orientations in between.

It is to be noted that no angle-ply laminate can fulfill all requirements in the current case – meaning that no feasible solution is found.

5.2.2 CTE Calculation

The coefficients of thermal expansion in the laminate direction in x-, y- and xy-plane-direction are calculated and shown in Figure 5.9 for an angle-ply laminate. To avoid high axial force due to thermal expansion, an measure is to limit the CTE in x-direction α_{xx} of the driveshaft within a certain range as discussed in Subsection 3.7.4. This limiting range is represented by two red lines in this figure.

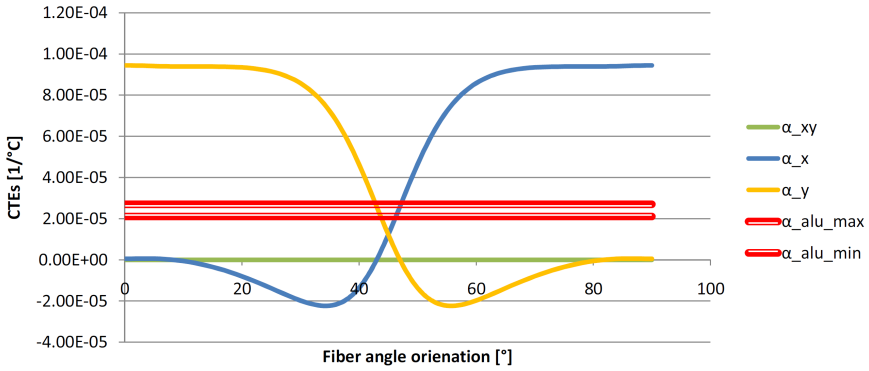

Figure 5.9: Parameter Study: CTEs

Limiting CTEs to a certain range of aluminum is very restrictive and also conservative meaning that it would lead to an extremely heavy shaft design. Therefore, a CTE constraint is not embedded neither in the structural model nor in the optimization of the driveshaft. As mentioned earlier, the different CTEs of metal and composite material should be taken into account when designing the end fittings.

5.3 Optimization of Blackhawk Driveline

5.3.1 Spinning and Misaligned Shaft Subjected to Torque Loading

In this subsection, results of the optimization model for a spinning, misaligned shaft under a torque loading are presented and discussed. The optimization model is executed five times to "assure" that the final solution obtained is the optimum solution.

A minimum-weight design is obtained by a stacking sequence of $[\pm 60/\pm 30/\pm 30/\pm 30/\pm 45]$ and four mid-span bearings. This solution was found to be the optimum solution in all five runs of the optimization tool. Therefore, it is highly probable that this is a global solution. The minimum-weight of the driveline is 24.1 kg. Compared to the current metallic driveline used in a Blackhawk helicopter, 7.25 kg of weight are saved which is 23.2%. Even though the same number of bearings as for a multi-segmented metallic design is used, a large

weight saving can be obtained. This saving is mainly due to the use of composite material which allows a lighter design. In addition to this, no flexible couplings are required for a one-piece driveshaft design which accounts for 1.36 kg (=4·0.34 kg) in the current metallic design.

In Table 5.1, the margins of safety for overheating, strain, stress, whirling and buckling are presented. On the one hand, a margin of safety of more than two for buckling is comparably high and the margin of safety for overheating is still well above 1. On the other hand, the margins of safety for stress and whirling are very close to 1. The optimum design configuration can just meet the requirements. The number of mid-spans bearings is mainly determined by the whirling criterion whereas the number of plies is driven by the maximum stress and buckling torque criteria. The overheating criterion highly influences the layup stacking sequence of the driveshaft.

Table 5.1: Margin of safety factors (Blackhawk)

	$MoS_{overh.}$	MoS_{strain}	MoS_{stress}	MoS_{whirl}	$MoS_{buckling}$
$f_{op} = 4116$ rpm $T_{op} = 734$ Nm	1.2229	1.1076	1.0270	1.0184	2.0265

5.3.2 Varying Applied Torque and Rotational Speed

By varying the rotational speed, f and applied torque, T, more insight into shaft design can be gained.

In a first study, the rotational speed and torque is increased and/or decreased by 25% to analyze the sensitivity of a minimum-weight driveshaft design on loading and speed.

In a second study, the transmitted power along the shaft is constant. If the rotational speed is increased, the applied buckling has to be decreased proportionally and vice versa.

Varying torque and rotational speed

In Table 5.2[1], optimum driveshaft designs are obtained by execution the optimization tool. Again, the optimization model was run five times.

[1]A ratio of (T/T_{op})=1.25 means that the applied torque in this study is 25% higher than the applied torque during operating condition. Similarly, the (f/f_{op})-ratio is defined.

Table 5.2: Varying torque and rotational speed (Blackhawk driveline)

Index:	(1)	(2)	(3)	(4)	(5)	(6)	(7)	(8)	(9)
T/T_{op}	1.0	1.0	1.0	1.25	1.25	1.25	0.75	0.75	0.75
f/f_{op}	1.0	1.25	0.75	1.25	1.0	0.75	0.75	1.0	1.25
# mid-span bearings	4	5	4	5	4	4	4	4	5
# $\pm$ layers	5	5	5	5	6	5	4	4	4
Driveline weight [kg]	24.1	27.9	24.1	27.9	25.7	24.1	22.4	22.4	26.2
Weight saving [%]	23.2	10.9	23.2	10.9	17.8	23.2	26.6	26.6	16.3

As expected, most weight can be saved if rotational speed and applied torque are lowest. It is to be mentioned that for a $(T/T_{op}) = 0.75$- and $(f/f_{op}) = 0.75$-ratio, a feasible solution for three mid-span bearings could almost be realized obtained.

A detailed list of minimum-weight designs obtained for the different (T/T_{op})- and (f/f_{op})-ratios are presented. The layup stacking sequences, numbers of layers (given by stacking sequence) and numbers of mid-span bearings are shown in Table 5.3.

Table 5.3: Stacking sequence for varying torque and rotational speed (Blackhawk driveline)

	Stacking sequence:	# $\pm\theta$-plies	# mid-span bearings
(1)	$[\pm 60/\pm 30/\pm 30/\pm 30/\pm 45]$	5	4
(2)	$[\pm 60/\pm 30/\pm 30/\pm 30/\pm 45]$	5	5
(3)	$[\pm 60/\pm 45/\pm 45/\pm 45/\pm 45]$	5	4
(4)	$[\pm 45/\pm 45/\pm 30/\pm 30/\pm 45]$	5	5
(5)	$[\pm 45/\pm 45/\pm 30/\pm 30/\pm 30/\pm 45]$	6	4
(6)	$[\pm 60/\pm 45/\pm 45/\pm 45/\pm 45]$	5	4
(7)	$[\pm 60/\pm 30/\pm 30/\pm 45]$	4	4
(8)	$[\pm 60/\pm 30/\pm 30/\pm 30]$	4	4
(9)	$[\pm 60/\pm 30/\pm 30/\pm 45]$	4	5

For any (T/T_{op})- and (f/f_{op})-ratio, only three different fiber angle orientations, 30°, 45° and 60°, occur for a minimum-weight driveshaft with an overall highest margin of safety. For a high torque, 45° fiber orientations are predominantly used.

The corresponding margins of safety are presented in Table 5.4.

Table 5.4: Margins of safety for varying torque and rotational speed (Blackhawk driveline)

	$MoS_{overh.}$	MoS_{strain}	MoS_{stress}	MoS_{whirl}	$MoS_{buckling}$
(1)	1.2229	1.1076	1.0270	1.0184	2.0265
(2)	1.2003	1.1074	1.0269	1.1693	2.0568
(3)	1.2760	1.6068	1.4888	1.0122	1.8703
(4)	1.1617	1.1437	1.0614	1.1411	1.0553
(5)	1.1350	1.2497	1.1601	1.0246	1.7151
(6)	1.2760	1.4434	1.3375	1.0122	1.4962
(7)	1.2866	1.1048	1.0239	1.2970	1.6052
(8)	1.2490	1.0988	1.0188	1.0726	1.2000
(9)	1.2495	1.1044	1.0237	1.1175	1.6047

For most (T/T_{op})- and (f/f_{op})-ratios, either maximum ply-level strength or whirling seems to prevent further weight savings. Only for a ratio of (T/T_{op})=1.25 and (f/f_{op})=1.25, buckling is the most critical requirement. For a $(T/T_{op}) = 0.75$- and $(f/f_{op}) = 0.75$-ratio, a relatively high margin of safety is obtained for whirling. Since whirling is the main driving factor to determine the number of mid-span bearings, this is an indicator that three mid-span bearings would be sufficient if the rotational speed is lower by only a small amount. It can be seen that the margin of safety for maximum ply-level stresses is always lower than for maximum ply-level strains. As discussed in Subsection 3.4.4, this behavior could be expected. However, it is important to mention that configurations exist for which a maximum strain criterion is more restrictive. The margin of safety for overheating is relatively high compared to other requirements. Nevertheless, the maximum temperature requirement influences the layup stacking sequences for an optimum design significantly and is not to be neglected. In addition to this, the self-heating model affects the rest of the structural analysis by using the temperature- and frequency-dependent material properties.

Varying torque and rotational speed (constant power transmission)

.

In this study, torque and rotational speed are varies so that the power transmission is constant, 316 kW. If the (T/T_{op})-ratio is defined, the (f/f_{op})-ratio is determined by the inverse ratio and vise versa.

Table 5.5: Varying torque and rotational speed (constant power transmission, Blackhawk driveline)

Index:	(1)	(2)	(3)	(4)	(5)	(6)	(7)
T/T_{op}	0.40	0.60	0.80	1.00	1.25	1.67	2.50
f/f_{op}	2.50	1.67	1.25	1.00	0.80	0.60	0.40
# mid-span bearings	7	6	5	4	4	3	3
# $\pm$ layers	3	4	4	5	5	6	7
Driveline weight [kg]	32.2	30.0	26.2	24.1	24.1	21.9	23.5
Weight saving [%]	**-2.7 (!)**	**1.3**	**13.3**	**23.2**	**23.2**	**30.1**	**24.8**

In Figure 5.10, the weight savings in % are shown graphically for a constant power scenario. The T/T_{op} is equal to the inverse ratio of f/f_{op} which is shown on the x-axis.

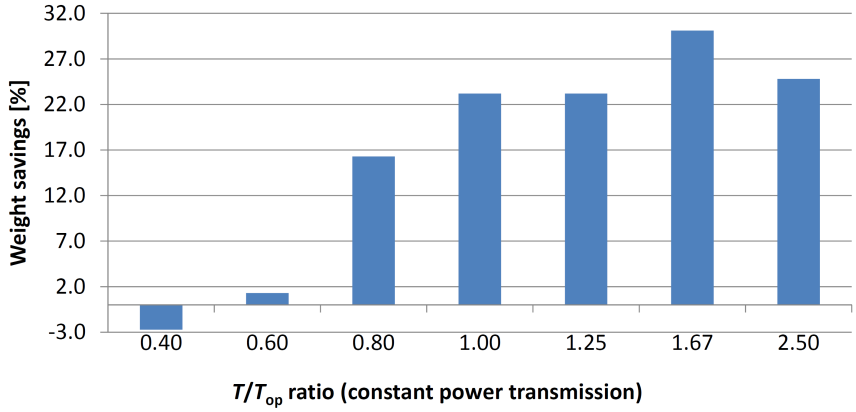

Figure 5.10: Parameter study - Varying torque and rotational speed (constant power transmission, Blackhawk driveline)

A minimum-weight driveshaft is obtained by using a ratio of $f/f_{op} = 0.6$ $(T/T_{op} = 1.67)$ for which three mid-span bearings are sufficient to prevent whirling. If the (f/f_{op}) is decreased to 0.4, driveshaft weight increases since the applied torque is very high and more plies are required. It is to be mentioned that seven is the maximum number of plies to be used so that a thin-walled driveshaft solution

is obtained. Moving on to higher (f/f_{op})-ratios, the number of mid-span bearings is to be increased to meet critical speed requirements. The number of layers can be reduced since the applied torque is lower. For a very high rotational speed of 2.5 times the operating speed, seven mid-span bearings are required. This leads to a driveshaft which is heavier than the current metallic shaft.

A detailed list which provides stacking sequence, number of layers (given by stacking sequence) and number of mid-span bearings is presented in Table 5.6.

Table 5.6: Stacking sequence for varying torque and rotational speed (Blackhawk driveline)

	Stacking sequence:	# $\pm\theta$-plies	# mid-span bearings
(1)	$[\pm 60/\pm 30/\pm 30]$	3	f
(2)	$[\pm 60/\pm 30/\pm 30/\pm 45]$	4	6
(3)	$[\pm 60/\pm 30/\pm 30/\pm 45]$	4	5
(4)	$[\pm 60/\pm 30/\pm 30/\pm 30/\pm 45]$	5	4
(5)	$[\pm 45/\pm 45/\pm 30/\pm 30/\pm 45]$	5	4
(6)	$[\pm 45/\pm 45/\pm 30/\pm 30/\pm 30/\pm 45]$	6	3
(7)	$[\pm 75/\pm 45/\pm 45/\pm 45/\pm 45/\pm 45/\pm 45]$	7	3

Compared to the first study, a fiber angle orientation of 75° is present in one minimum-weight design. Again, 45° fiber orientations are predominant when torque is high. Fiber orientations of 30° are prevailing where whirling is more critical.

The corresponding margins of safety are shown in Table 5.7.

As in the first study for varying loads, the stress criterion is more restrictive than the maximum strain criterion. Apart from a (f/f_{op})-ratio of 0.8, maximum stress or whirling requirements are driving the design. When varying rotational speed and torque for a constant power transmission of the shaft, significant weight differences occur. In the best case, more than 30% can be saved. The corresponding margins of safety are pretty low and indicate that not much more weight can be saved by choosing a different rotational speed and applied torque for a constant power transmission scenario.

5.3.3 Varying Misalignment

In this study, the effect of misalignment on a optimum driveshaft solution is investigated. A misalignment of the shaft results in a bent driveshaft shape. A constant curvature along the shaft is assumed which results in constant bending

Table 5.7: Margins of safety for varying torque and rotational speed (Blackhawk driveline)

	$MoS_{overh.}$	MoS_{strain}	MoS_{stress}	MoS_{whirl}	$MoS_{buckling}$
(1)	1.2316	1.1695	1.0835	1.0385	1.1558
(2)	1.2241	1.1851	1.0985	1.1367	2.0263
(3)	1.2492	1.0798	1.0009	1.1175	1.5044
(4)	1.2229	1.1076	1.0270	1.0184	2.0265
(5)	1.2118	1.1441	1.0617	1.2393	1.0604
(6)	1.1974	1.0986	1.0195	1.0939	1.2821
(7)	1.2908	1.1444	1.0585	1.2063	2.0510

strain (see Subsection 3.3.2). The rotational speed, $f = f_{op}$, and applied torque, $T = T_{op}$ are constant within this study. The bending strain applied within the model is equal to $F_{bend} \cdot 1500\mu\varepsilon$.

The results of the optimization model are shown in Table 5.8. By increasing the bending strain along the shaft, a heavier solution is obtained whereas when misalignment is reduced a lighter design can be realized. This trend correlates with expectations. Not only the amount of heat generation within the shaft is higher for a larger bending strain but also the resulting bending moment induced by misalignment increases.

Table 5.8: Varying misalignment (bending strain) of driveline (Blackhawk)

Index:	(1)	(2)	(3)	(4)	(5)	(6)	(7)
F_{bend}	0.40	0.60	0.80	1.00	1.20	1.40	1.60
# mid-span bearings	4	4	4	4	4	5	5
# ± layers	4	4	5	5	5	4	4
Driveline weight [kg]	22.4	22.4	24.1	24.1	24.1	26.2	26.2
Weight saving [%]	**26.6**	**26.6**	**23.2**	**23.2**	**23.2**	**16.3**	**16.3**

The layup stacking sequences are presented in Table 5.9 and the margins of safety are shown in Table 5.10. If bending strain is low (600 $\mu\varepsilon$), fiber angle orientations of 10° are used within an optimum layup for a shaft. Since, bending strain is lower, overheating of the shaft is less critical and this low fiber orientation enables to find a stacking sequence which is beneficial for whirling. A margin of safety for critical speed of 1.13 was found which is relatively high compared to the other margins of safety.

In Subsection 5.2.1, it was shown that fiber angle orientations around 20°C lead to a high maximum shaft temperature for an angle-ply laminate. Apparently, this trend is also observed for multi-angle laminates (see Section 5.2). Therefore, 45° fiber orientations for much bending strain and 10°, 15° for a low amount of misalignment are use within an optimum layup. Also, it can be observed that the fiber orientations used vary a lot for different amounts of bending strains. This is an indicator that bending strain and consequently overheating of the shaft has a large impact on the stacking sequence.

Table 5.9: Stacking sequence for varying bending strain (Blackhawk driveline)

	Stacking sequence:	# $\pm\theta$-plies	# mid-span bearings
(1)	$[\pm 60/\pm 10/\pm 10/\pm 60]$	4	4
(2)	$[\pm 60/\pm 15/\pm 30/\pm 45]$	4	4
(3)	$[\pm 75/\pm 30/\pm 30/\pm 30/\pm 45]$	5	4
(4)	$[\pm 60/\pm 30/\pm 30/\pm 30/\pm 45]$	5	4
(5)	$[\pm 75/\pm 30/\pm 30/\pm 30/\pm 45]$	5	4
(6)	$[\pm 75/\pm 45/\pm 45/\pm 45]$	4	5
(7)	$[\pm 60/\pm 45/\pm 45/\pm 45]$	4	5

Table 5.10: Margins of safety for varying bending strain (Blackhawk driveline)

	$MoS_{overh.}$	MoS_{strain}	MoS_{stress}	MoS_{whirl}	$MoS_{buckling}$
(1)	1.3740	1.2582	1.1692	1.1296	1.5069
(2)	1.3433	1.1679	1.0826	1.0641	1.2892
(3)	1.2983	1.1133	1.0316	1.0037	2.4436
(4)	1.2229	1.1076	1.0270	1.0184	2.0265
(5)	1.0707	1.1898	1.1050	1.0643	1.1864
(6)	1.2067	1.1694	1.0799	1.0345	1.4396
(7)	1.1568	1.1787	1.0927	1.0732	1.0838

To sum up, the amount of bending strain which is driving the maximum temperature calculation within the shaft influences the layup stacking sequence of the driveshaft a lot. However, the number of mid-span bearings and number of layers is less dominated by overheating rather than critical speed, buckling and maximum stresses.

5.4 Optimization of Chinook Driveline

5.4.1 Properties

Instead of a Blackhawk driveline, a driveline for a Chinook helicopter is optimized here. It is to be noted that computation time for this helicopter driveshaft increases by a factor of around seven compared to the Blackhawk driveshaft optimization problem. This is due to the fact that the outer diameter is larger than for a Blackhawk driveshaft which determines the maximum number of plies to be used within the optimization (see Section 4.2). In addition to this, the population size is increased from 40 to 60 since the design solution space is larger. This increases computation time of the optimization model significantly.

Loads and other properties such as length and outer radius for a Chinook driveline are presented in Table 4.2.

5.4.2 Spinning and Misaligned Shaft Subjected to Torque Loading

Results of the optimization model for a rotating, misaligned Chinook driveline under a torque loading are presented and discussed in this subsection. Again, the optimization model is executed five time to assure to obtain an optimum shaft design solution.

The minimum-weight design is obtained with a stacking sequence of $[\pm 60/\pm 60/\pm 45/\pm 45/\pm 45/\pm 45/\pm 45/\pm 45]$ and six mid-span bearings. A driveline weight of 49.0 kg is determined which leads to a weight saving of 18.6% (11.1 kg) compared to the current multi-segmented metallic design (60.1 kg). As for the Blackhawk optimization, the number of mid-span bearings is the same as for a multi-segmented metallic driveline. However, no flexible joints are required since a one-piece composite driveshaft design is realized. By omitting flexible couplings, 2.76 kg (=6·0.46 kg) of weight can be saved by using a one piece design. The remaining weight saving is due to the use of LF750D/AS4D instead of metal.

Table 5.11 shows the margins of safety for overheating, strain, stress, whirling and buckling. Buckling is least critical whereas maximum ply-level stress seems to be the driving factor. However, the whirling, maximum ply-level strain and overheating criteria are also fairly close to 1.

Table 5.11: Margin of safety factors (Chinook driveline)

	$MoS_{overh.}$	MoS_{strain}	MoS_{stress}	MoS_{whirl}	$MoS_{buckling}$
$f_{op} = 6912$ rpm $T_{op} = 4067$ Nm	1.1239	1.1054	1.0241	1.1048	1.3397

5.4.3 Varying Applied Torque and Rotational Speed

The applied torque and rotational speed are varied by keeping the transmitted power constant as this is done for a Blackhawk driveline in Subsection 5.3.2.

Minimum-weight designs with the highest overall margins of safety are shown in Table 5.12 for different (T/T_{op})-ratios.

Table 5.12: Varying torque and rotational speed applied (constant power transmission, Chinook driveline)

Index:	(1)	(2)	(3)	(4)	(5)
T/T_{op}	0.67	0.80	1.00	1.25	1.5
f/f_{op}	1.5	1.25	1.00	0.80	0.67
# mid-span bearings	8	7	6	5	No Solution
# ± layers	6	7	8	11	No Solution
Driveline weight [kg]	55.0	52.0	49.0	50.1	-
Weight saving [%]	**8.4**	**13.5**	**18.6**	**16.7**	-

If rotational speed is increased (f/f_{op}=1.5 and f/f_{op}=1.25), more mid-span bearings are required to avoid whirling and the number of layers can be reduced due to the lower torque load applied. If the applied torque is increased (T/T_{op}=1.25), three more (±)-layers are required but one mid-span bearing can be avoided. However, no additional weight savings can be obtained by changing the ratio between rotational speed and torque for a constant power transmission. It is to be noted that no solution can be found for a ratio of T/T_{op}=1.5 and f/f_{op}=0.67. Torsional loading is too high and cannot be carried by a thin-walled driveshaft solution. Maximum stresses due to torsion are too high. Buckling seems not to be the limiting factor, a margin of safety of more than two for buckling is obtained (see Table 5.14).

In Table 5.13, the layup stacking sequences, for the scenarios shown above, are presented. As for a Blackhawk driveline, 45° fiber angle orientation plies are predominantly used if the applied torque is high. However, in contrast to a Blackhawk driveshaft, 45° fiber orientations are also mainly used for a lower amount of torque. This is mainly due to overheating requirements since heat generation is typically higher for thicker laminates.

Table 5.13: Stacking sequence for varying torque and rotational speed (constant power transmission, Chinook driveline)

	Stacking sequence:	# $\pm\theta$-plies	# mid-span bearings
(1)	$[\pm 75/\pm 45/\pm 45/\pm 45/\pm 45/\pm 45]$	6	8
(2)	$[\pm 88/\pm 45/\pm 45/\pm 45/\pm 45/\pm 45/\pm 45]$	7	7
(3)	$[\pm 60/\pm 60/\pm 45/\pm 45/\pm 45/...$ $...\pm 45/\pm 45/\pm 45]$	8	6
(4)	$[\pm 60/\pm 75/\pm 45/\pm 45/\pm 45/\pm 45/...$ $... \pm 45/\pm 45/\pm 45/\pm 45/\pm 45]$	11	5

The margins of safety are presented in Table 5.14. The maximum ply-level stresses seem to driving the number of minimum plies to be used.

Table 5.14: Margins of safety for varying torque and rotational speed (Chinook driveline)

	$MoS_{overh.}$	MoS_{strain}	MoS_{stress}	MoS_{whirl}	$MoS_{buckling}$
(1)	1.1311	1.1353	1.0505	1.2193	1.1433
(2)	1.1252	1.0814	1.0007	1.1685	1.4718
(3)	1.1239	1.1054	1.0241	1.1048	1.3397
(4)	1.0931	1.1023	1.0203	1.0124	2.3784

To sum up, no additional weight savings are possible for a constant power transmission by varying the ratio between rotational speed and applied torque. A similar trend with respect to driving factors was found as for a Blackhawk driveshaft. The number of mid-span bearings is mainly driven by whirling. The number of plies is dominated by the maximum stress criterion and buckling requirements. Shaft overheating mainly affects the layup stacking sequence.

5.5 Comparison to Previous Work

Similar weight savings are reported by Mayrides (2005) for Blackhawk and Chinook drivelines. For a Blackhawk driveline, 29% (9 kg) could be reduced at most and for a Chinook, 26% (15.2 kg). Although, Mayrides (2005) used a softer polyurethane-carbon composite material system, Adiprene L100/Caytur 21 polyurethane resin and T700 carbon fibers, three and five mid-span bearings

for a Blackhawk and Chinook driveline, respectively, are sufficient to operate the driveshaft in a subcritical range. These findings are suprising to the author at first since a softer material should result in a larger number of mid-span bearings compared to a stiffer FMC since whirling is expected to be more critical.

It is to be mentioned again that Mayrides (2005) used quasi-static material properties within his model. The dynamic temperature- and frequency-dependent behavior, however, has a large impact on the final design solution since FMC materials are very sensitive to these two properties. As mentioned in Subsection 2.6, Y. Shan showed that the whirling model used by Mayrides (2005) overestimates critical speed by a factor of more than 2. Therefore, it is not surprising that Mayrides could omit one mid-span bearing more for a Blackhawk and Chinook driveline. Taking this factor of two into account within the whirling analysis, it is highly probable that an optimum solution for L100/T700 has four or more mid-span bearings for a Blackhawk driveline and six or more for a Chinook driveline. According to this, less weight can be saved by using a L100/T700 than L750D/AS4D.

Chapter 6

Conclusion

6.1 Conclusions

A multi physics structural model was developed which is capable of predicting maximum shaft temperature for a spinning, misaligned one-piece composite driveshaft due to self-heating. Also, a critical speed and buckling torque analysis are executed. In addition to this, ply-level stresses and strains are calculated. Quasi-static and dynamic temperature- and frequency dependent material properties for LF750D/AS4D are embedded within the structural model. The model was validated according to literature, experiments and/or FEM. Safety factors are applied within the structural model to take uncertainties into account.

A powerful optimization tool, using a genetic algorithm, which can predict the optimal layup stacking sequence, number of plies and number of mid-span bearings of a minimum-weight driveshaft design was built. This tool was applied to a Blackhawk and Chinook driveline design. This is the first time that a self-heating model using temperature- and frequency-dependent material properties is used in driveshaft designing.

The optimization model was first applied to a Blackhawk driveshaft. By tailoring the stacking sequence and number of mid-span bearings to structural as well as thermal requirements, the following design solution can be obtained. The minimum number of mid-span bearings is determined to be four. A stacking sequence of $[\pm 60/\pm 30/\pm 30/\pm 30/\pm 45]$ with six $\pm\theta$-plies results in a minimum driveline weight of 24.1 kg. The current multi-segmented metallic design also has four mid-span bearings and weights 31.3 kg. Applying a driveshaft made of FMCs enables a weight saving of 23.2% (=7.25 kg). This weight saving is mainly due to the use of LF750D/AS4D. By applying a one-piece driveshaft design, flexible joint couplings can be omitted. This reduces the driveshaft weight by a few kilograms and also helps minimizing service and maintenance requirements.

For a Chinook driveline, a weight saving of 18.6% (=11.1 kg) compared to the current metallic design (= 60.1 kg) can be realized. Roughly one fourth of the weight saving is achieved by avoiding the flexible couplings.

In different studies, the effect of varying torque, rotational speed and bending strain due to misalignment has been investigated. This gave some valuable insight into driveshaft designing. For a Blackhawk and Chinook driveline, whirling instability is the driving factor to determine the minimum number of mid-span bearings. The minimum number plies is dominated by maximum stresses and buckling requirements. The layup stacking sequence is greatly affected by overheating which typically prevents the use of fiber angle orientations around 20°. Also, by changing the ratio between rotational speed and applied torque for a constant power transmission, weight savings of more than 30% could be realized for a Blackhawk driveshaft.

6.2 Recommendations and Outlook

In the following, some recommendations for future investigations on driveshafts are listed.

- The polyurethane-carbon material LF750D/AS4D was characterized quasi-statically and dynamically by analytical models and experiments. However, good values for the quasi-static properties such as the E-modulus in 1-direction E_{11} for a filament-wound tube are still not available. Analytical models do not agree well with experimental data, especially for angle-ply laminates with a low fiber angle orientation. Also, failure strength and failure strains are extremely low for angle-ply laminates with a low fiber angle orientation. The specimen design and testing setup might need to be adjusted. For a $\pm 10°$ angle-ply laminate, a very high Poisson's ratio is obtained. This leads to a bad failure mode when testing this angle-ply tube in compression. The tube fails at the grips. The Poisson's ratio can dramatically be reduced by adding a 90°-ply to the laminate. This is already a planned future project which will be carried out by Mr. Steve Smith at Penn State.

- Filament-wound tubes typically have $\pm\theta$-layers and therefore, crossover of fibers and fiber undulation occurs. No analytical model is available so far which can predict this effect and its influence on material properties such as strength, failure strains and stiffness. The development of such a model is not straight-forward but would definitely help predicting better material properties. However, it could easily be integrated within the structural model and also within the optimization model if computation time is reasonable.

- The structural model developed within this work incorporated a buckling, whirling, self-heating, stress and strain analysis. Herein, a steady state operating condition was assumed. In helicopter maneuvers, however, non-constant loads and varying shaft misalignments may occur. During take-off

or landing, loads are changing a lot. The effect of varying loads on the driveshaft design should be investigated.

- There is a continuous demand in developing new composite material systems to build lighter and more efficient structures. Considering flexible matrix composites, the resin system to be employed is of highest importance. An almost infinite number of resins can be obtained by changing the molecular structure. In order to judge a fiber-resin system to be a viable candidate for a FMC driveshaft, the optimization tool presented can support the decision making process once lamina properties have been determined by experiments.

- Fatigue is not considered in this structural model. Compared to metallic materials, rigid composite material, typically, have superior properties regarding fatigue. Even though, it was shown by Hannibal and Avila (1984) that FMC show better fatigue behavior than RMC, more work in this area needs to be done. It is expected that different matrix systems can lead to quite different fatigue behaviors. For instance, the bonding between matrix and fibers is expected to play a crucial role. This not only affects static properties but also the fatigue behavior. After characterizing a specific material system such as LF750/AS4D, a knockdown factor in the structural model may be applied, if required, which takes fatigue into account.

- From a driveshaft design point of view, using composite materials instead of metals imposes some additional challenges. The development of midspan bearings which can be mounted on a one-piece driveshaft are to be developed. These bearings should be easily accessible for service and maintenance work. Forces perpendicular to longitudinal axis of the shaft which are unavoidable need special care in order to avoid a point-load failure of the composite shaft. Also, special provisions must be made to install midspan bearings at various places along the longitudinal axis of the driveshaft. It is not clear at this stage how this should be done best. In the current multi-segmented metallic driveshaft this design problem does not occur since supportive bearings can easily be mounted at the ends of each segment.

- An end-fitting design for both ends of a FMC shaft is to be developed. They need to be able to accommodate for axial expansion of the shaft, for instance due to thermal expansion. In addition to this, a robust design is required which can operate in a condition where shaft misalignment and loading is high. Axial forces in the driveshaft are to be avoided. Thermal expansion should be considered carefully during the design stage since large axial forces can occur assuming the rest of the supporting structure is still metallic.

- An effective optimization tool has been developed which can predict the optimum layup stacking sequence and minimum number of mid-span bearings for a minimum driveshaft weight design. Results obtained look reasonable and intuitive. Nevertheless, it is suggested to build a full-scale model of a LF759/AS4D driveshaft. Static and dynamic testing might be able to prove experimentally that the solution obtained is a good design for a practical driveline application.

Bibliography

Ambartsumyan, S. A. (1964). Theory of Anisotropic Shells. *NASA TT F-118*, pages 18–60.

Bauchau, O., Krafchack, T., and Hayes, J. (1988). Torsional Buckling Analysis and Damage Tolerance of Graphite/Epoxy Shafts. *Journal of Composite Materials*, 22:258–270.

Bert, C. W. and Kim, C.-D. (1995a). Analysis of Buckling of Hollow Laminated Composite Drive Shafts. *Composites Science and Technology*, 53(3):343–351.

Bert, C. W. and Kim, C.-D. (1995b). Dynamic Instability of Composite-Material Drive Shaft Subject to Fluctuating Torque and/or Rotational Speed. *Dynmaics and Stability of Systems*, 10(2):125–147.

Bert, C. W. and Kim, C.-D. (1995c). Whirling of Composite-Material Driveshafts including Bending-Twisting Coupling and Transverse Shear Deformation. *Journal of Vibration and Accoustics*, 117(1):17–21.

Bogetti, T. A., Gillespie, J. W., Jr., and Lamontia, M. A. (1992). Influence of Ply Waviness on the Stiffness and Strength Reduction on Composite Laminates. *Journal of Thermoplastic Composite Materials*, 5(4):344–369.

Boukhalfa, A., Hadjoui, A., and Cherif, S. M. H. (2008). Free Vibration Analysis of a Rotating Composite Shaft Using the p-Version of the Finite Element Method. *International Journal of Rotating Machinery*, 2008:1–10.

Chang, M.-Y., Chen, J.-K., and Chang, C.-Y. (2004). A Simple Spinning Laminated Composite Shaft Model. *International Journal of Solids and Structures*, 41(2-3):637–662.

Chemtura (2010). http://www.chemtura.com.

Cheng, S. and Ho, B. P. C. (1963). Stability of Heterogeneous Aelotropic Cylindrical Shells under Combined Loading. *AIAA Journal*, 1(4):892–898.

Daniel, I. M. and Ishai, O. (2006). *Engineering Mechanics of Composite Materials*. Oxford University Press, 2 edition.

Dharmarajan, S. and McCutchen, H. (1973). Shear Coefficients for Orthotropic Beams. *Journal of Composite Materials*, 7:530–535.

Dong, S. B., Pister, K. S., and Taylor, R. L. (1962). On the Theory of Laminated Anisotropic Shells and Plates. *Journal of Aerospace Science and Technology*, 29:969–975.

dos Reis, H. L. M., Goldmann, R. B., and Verstrate, P. H. (1987). Thin-Walled Laminated Composite Cylindrical Tubes: Part III - Critical Speed Analysis. *Journal of Composites Technology and Research*, 9(2):58–62.

Ferry, J. D. (1970). *Viscoelastic Properties of Polymers*. Weley, New York, 2 edition.

Gibson, R. F. (2007). *Principles of Composite Material Mechanics*. CRC Press, 2 edition.

Goldberg, D. E. (1989). *Genetic Algorithms in Search, Optimization and Machine Learning*. Addison-Wesley, Publishing Company, Inc.

Gubrana, H. B. H. and Guptab, K. (2004). The Effect of Stacking Sequence and Coupling Mechanisms on the Natural Frequencies of Composite Shafts. *Journal of Sound and Vibration*, 282(1-2):231–248.

Hannibal, A. J. and Avila, J. A. (1984). A Torsionally Stiff - Bending Soft Driveshaft. In *Proceedings of the 39th Annual Conference, Reinforced Plastic/Composite Institute*, Grapevine, Texas.

Hannibal, A. J., Gupta, B. P., Avila, J. A., and Parr, C. H. (1985). Flexible Matrix Composites Applied to Bearingless Rotor Systems. *Journal of the American Helicopter Society*, 30(1):21–27.

Hexcel (2010). http://www.hexcel.com.

Ho, B. P. C. and Cheng, S. (1963). Some Problems in Stability of Heterogeneous Aeolotropic Cylindrical Shells under Combined Loading. *AIAA Journal*, 1(7):1603–1607.

Hsiao, H. M. and Daniel, I. M. (1996). Effect of Fiber Waviness on Stiffness and Strength Reduction of Unidirectional Composites under Compressive Loading. *Composites Science and Technology*, 56(5):581–593.

Jolicoeur, C. and Cardou, A. (1994). Analytical Solution for Bending of Coaxial Orthotropic Cylinders. *Journal of Engineering Mechanics*, 120(12):2556–2574.

Kim, C.-D. and Bert, C. W. (1993). Critical Speed Analysis of Laminated Composite, Hollow Drive Shafts. *Composites Engineering*, 3:633–643.

Kollár, L. P. (1994). Buckling of Anisotropic Cylinders. *Journal of Reinforced Plastics and Composites*, 13:954–975.

Kress, G. (1985). Orthotropic Properties of Layered Fiber Composites. In *Proceedings of Workshop: Composite Design for Space Applications*, ESTEC, Noordwijk, Netherlands.

Kress, G. (1986). *Three-Dimensional Properties of a Generally Orthotropic Symmetric Laminate*. In W.A. Green and M. Micunovic, editors, Mechanical Behaviour of Composites and Laminates, chapter III, pages 185-191. Elsevier Applied Science, Kupari, Yugoslavia.

Kress, G. and Keller, D. (2007). *Structural Optimization*. Zentrum für Strukturtechnologien (IMES), Swiss Federal Institute of Technology Zurich.

Lim, J. W. and Darlow, M. S. (1986). Optimal Design of Composite Power Transmission Shafting. *Journal of American Helicopter Society*, 31(1):75–83.

MatWeb (2010). http://www.matweb.com.

Mayrides, B. (2005). Analysis and Synthesis of Highly Flexible Rotorcraft Drivelines with Flexible Matrix Composite Shafting. Master thesis, The Pennsylvania State University, University Park, PA.

Ocalan, M. (2002). High Flexibility Rotorcraft Driveshafts Using Flexible Matrix Composites and Active Bearing Control. Master thesis, The Pennsylvania State University, University Park, PA.

Pansart, S., Sinapius, M., and Gabbert, U. (2009). A Comprehensive Explanation of Compression Strength Differences Between Various CFRP Materials: Micro-Meso Model, Predictions, Parameter Studies. *Composites Part A: Applied Science and Manufacturing*, 40(4):376–387.

Shan, Y. (2006). *Flexible Matrix Composites: Dynamic Charachterization, Modeling, and Potential for Driveshaft Application*. PhD thesis, The Pennsylvania State University, University Park, PA.

Shan, Y. and Bakis, C. E. (2009). Viscoelastic Characterization and Self–Heating Behavior of a Flexible Matrix Composite Driveshaft. *Journal of Composite Materials*, 43(12):1335–26.

Singh, S. E., Gubran, H. B. H., and Gupta, K. (1997). Developments in Dynamics of Composite Material Shafts. *International Journal of Rotating Machinery*, 3(3):189–198.

Sollenberger, S. G. (2010). Characterization and Modeling of a Flexible Matrix Composite Material for Advanced Rotorcraft Drivelines. Master thesis, The Pennsylvania State University, State College, PA.

Stecenko, T. and Piggott, M. R. (1997). Fiber Waviness and Other Mesostructures in Filament Wound Materials. *Journal of Reinforced Plastics and Composites*, 16(18):1659–1974.

Sun, C. and Li, S. (1988). Three-Dimensional Effective Elastic Constants for Thick Laminates. *Journal of Composite Materials*, 22:629–639.

ter Wijlen, H. Z. and de Boer, E. (1984). Designing, Manufacturing and Testing of Sub- and Supercritical Composite Shafts for Helicopter Tail Drive Line Applications. In *Proceedings of the 20th European Rotorcraft Forum*, volume 4, pages 1–15, Amsterdam, Netherlands.

Zhang, Y., Xia, Z., and Ellyin, F. (2008). Two-Scale Analysis of a Filament-Wound Cylindrical Structure and Application of Periodic Boundary Conditions. *International Journal of Solids and Structures*, 45(20):5322–5336.

Zinberg, H. and Symonds, M. F. (1970). The Development of an Advanced Composite Tail Rotor Drive Shaft. In *Proceedings of the 26th Annual Forum, American Helicopter Society*, pages 1–14, Washington, DC.

Zindel, D. (2009). Mechanical Modeling of Filament Wound Flexible Matrix Composites. Master thesis, The Pennsylvania State University and Swiss Federal Institute of Technology, Zurich, ZH.

Appendix A

Declaration of primary authorship

Title: Multi Physics Design and Optimization of Flexible Matrix Composite (FMC) Driveshafts

Student: Christoph Roos

ETH-ID: 05-906-805

E-Mail: chroos@ethz.ch

Declaration:

I hereby declare that I have written this thesis without any illegal help from others and without the use of documents and aids other than those stated. I have mentioned all used sources and cited them correctly according to established academic citation rules.

University Park, Pennsylvania, September, 2010: _____

Christoph Roos

Appendix B

Stress and Strain Validation (FE, P=1000 N)

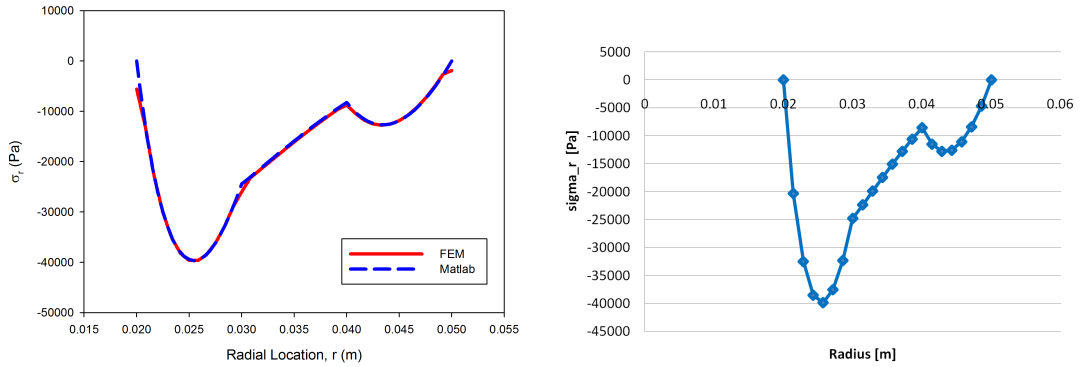

(a) Verification, to Y. Shan (unpublished)

(b) Structural Model

Figure B.1: Validation of stress and strain calculation - σ_r (FE)

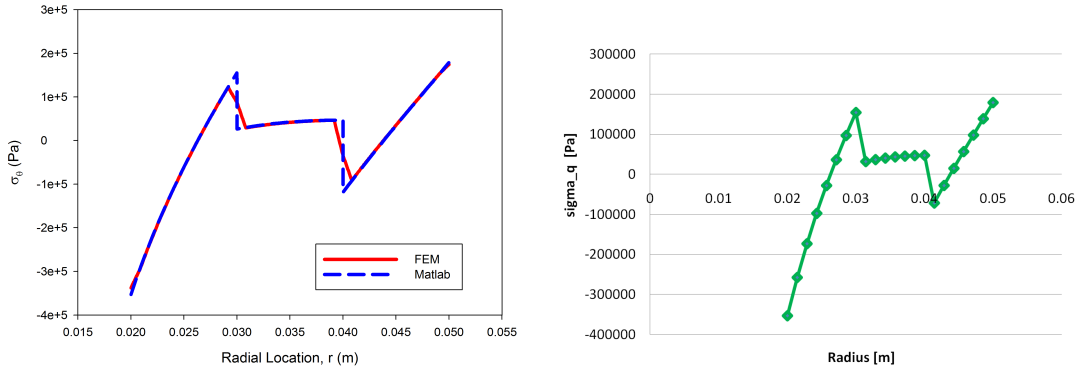

(a) Verification, to Y. Shan (unpublished) (b) Structural Model

Figure B.2: Validation of stress and strain calculation - σ_θ (FE)

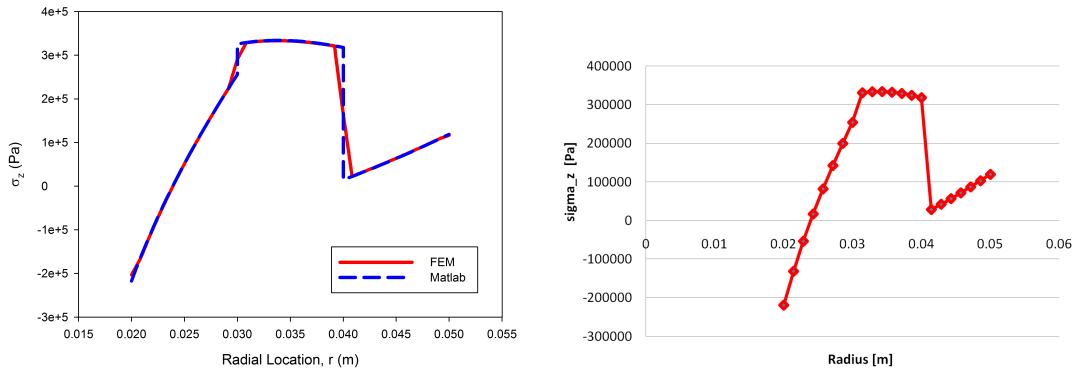

(a) Verification, to Y. Shan (unpublished) (b) Structural Model

Figure B.3: Validation of stress and strain calculation - σ_z (FE)

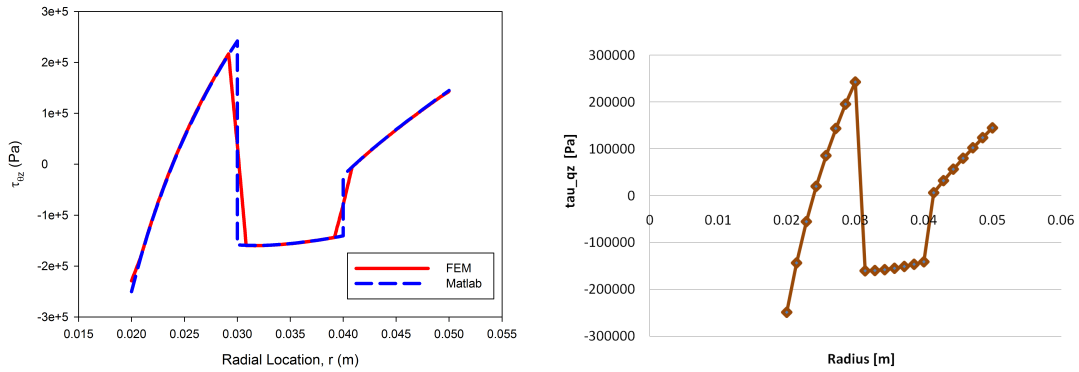

(a) Verification, to Y. Shan (unpublished) (b) Structural Model

Figure B.4: Validation of stress and strain calculation - $\tau_{\theta z}$ (FE)

Appendix C

Corrections of Critical Speed Calculation

In the following, critical speed calculations are executed for different factors C_S and K. Assumptions of the modeling and equations used are provided in Section 3.5. To sum up, the critical speed calculation is based on the theory presented by Bert and Kim (1995c). Two mistakes have been found in their work as explained in Subsection 3.5.2. The equations of the two factor C_S and K are not correct.

The corrected equations for the shear stiffness factor C_S and shear correction coefficient K are shown in Equations C.1 and C.2 (Equations 3.16 and 3.17).

$$C_S = K \cdot A \cdot \bar{G}_{xy} \tag{C.1}$$

$$K = \frac{\frac{6}{7} \cdot (1 - \bar{m}^4) \cdot (1 + \bar{m}^2)}{1 + \frac{27}{7} \cdot \bar{m}^2 \cdot (1 - \bar{m}^2) - \bar{m}^6 - 2 \cdot \left(\frac{\bar{\nu}_{xy} \cdot \bar{G}_{xy}}{7 \cdot \bar{E}_{xx}}\right) \cdot [1 + 9 \cdot \bar{m}^2 \cdot (1 - \bar{m}^2) - \bar{m}^6]} \tag{C.2}$$

If shear stiffness factor C_S (see Equation C.3) and the shear correction coefficient K (see Equation C.4) according to Bert and Kim (1995c) are used, then the results presented in Figures C.1 and C.2 are obtained.

If shear stiffness factor C_S (see Equation C.5) and the shear correction coefficient K (see Equation C.6) according to Bert and Kim (1995c) and in-plane material properties are used, then the results shown in Figures C.3 and C.4 are obtained.

In Figures C.1 and C.3, an off-axis laminate with 10 layers is examined. A laminate with the stacking sequence [90/45/-45/0/0/0/0/0/0/45] is used for the validation case shown in Figures C.2 and C.4.

$$C_S = K \cdot A \cdot \bar{G}_{xz} \tag{C.3}$$

$$K = \frac{\frac{6}{7} \cdot (1 - \bar{m}^4) \cdot (1 + \bar{m}^2)}{1 + \frac{27}{7} \cdot \bar{m}^2 \cdot (1 + \bar{m}^2) - \bar{m}^6 - 2 \cdot \left(\frac{\bar{\nu}_{xz} \cdot \bar{G}_{xz}}{7 \cdot \bar{E}_{zz}}\right) \cdot [1 + 9 \cdot \bar{m}^2 \cdot (1 - \bar{m}^2) - \bar{m}^6]} \tag{C.4}$$

$$C_S = K \cdot A \cdot \bar{G}_{xy} \tag{C.5}$$

$$K = \frac{\frac{6}{7} \cdot (1 - \bar{m}^4) \cdot (1 + \bar{m}^2)}{1 + \frac{27}{7} \cdot \bar{m}^2 \cdot (1 + \bar{m}^2) - \bar{m}^6 - 2 \cdot \left(\frac{\bar{\nu}_{xy} \cdot \bar{G}_{xy}}{7 \cdot \bar{E}_{xx}}\right) \cdot [1 + 9 \cdot \bar{m}^2 \cdot (1 - \bar{m}^2) - \bar{m}^6]} \tag{C.6}$$

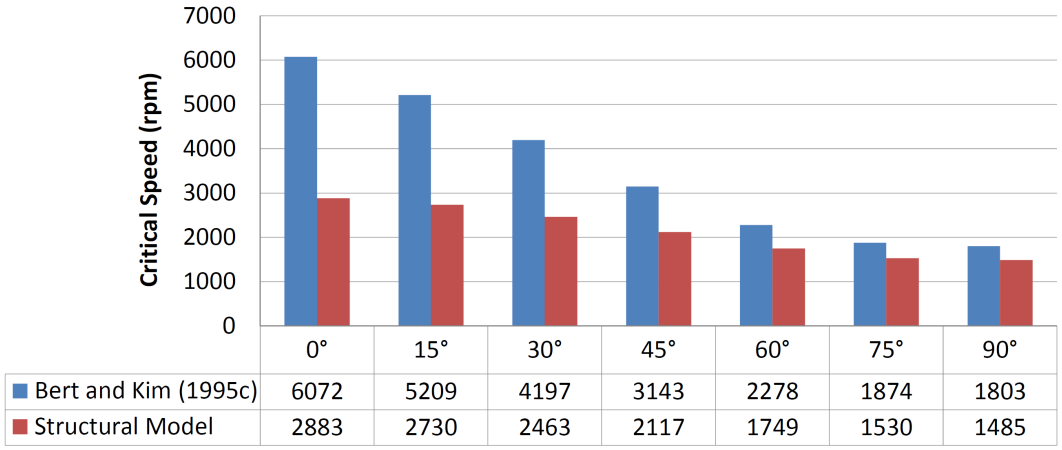

	0°	15°	30°	45°	60°	75°	90°
Bert and Kim (1995c)	6072	5209	4197	3143	2278	1874	1803
Structural Model	2883	2730	2463	2117	1749	1530	1485

Figure C.1: Validation of current structural model for critical speed vs. fiber angle orientations using K and out-of-plane material properties according to Bert and Kim (1995c)

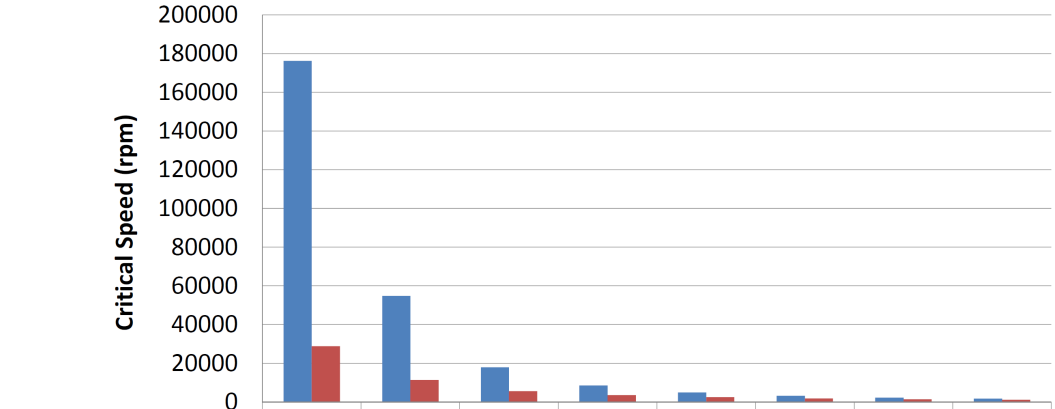

	2	5	10	15	20	25	30	35
Bert and Kim (1995c)	176300	54830	17880	8543	4945	3209	2246	1658
Structural Model	28733	11399	5540	3535	2508	1883	1466	1171

Figure C.2: Validation of current structural model for critical speed vs. L/D-ratio using K and out-of-plane material properties according to Bert and Kim (1995c)

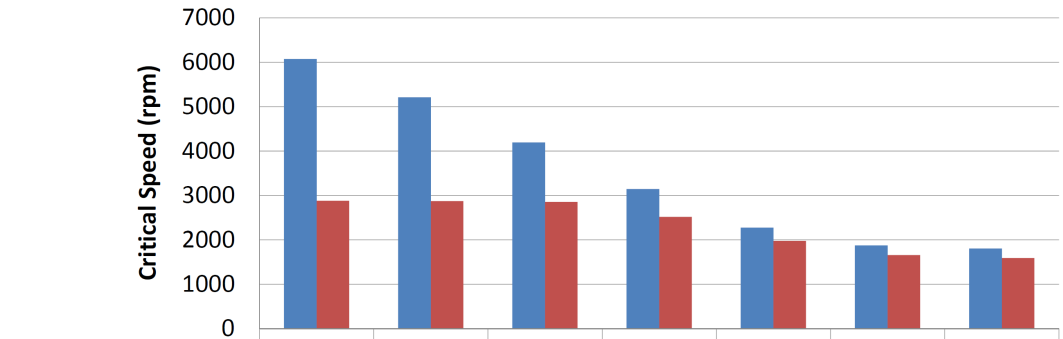

	0°	15°	30°	45°	60°	75°	90°
Bert and Kim (1995c)	6072	5209	4197	3143	2278	1874	1803
Structural Model	2880	2872	2853	2521	1977	1657	1590

Figure C.3: Validation of current structural model for critical speed vs. fiber angle orientations using K according to Bert and Kim (1995c) and in-plane material properties

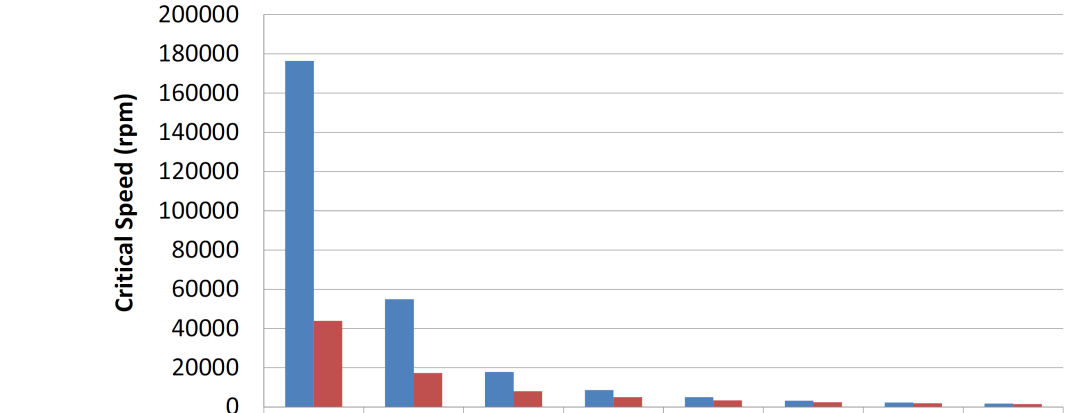

	2	5	10	15	20	25	30	35
Bert and Kim (1995c)	176300	54830	17880	8543	4945	3209	2246	1658
Structural Model	43887	17224	8089	4931	3336	2397	1796	1391

Figure C.4: Validation of current structural model for critical speed vs. L/D-ratio using K according to Bert and Kim (1995c) and in-plane material properties

Appendix D

Determination of Parameters for Optimization Algorithm

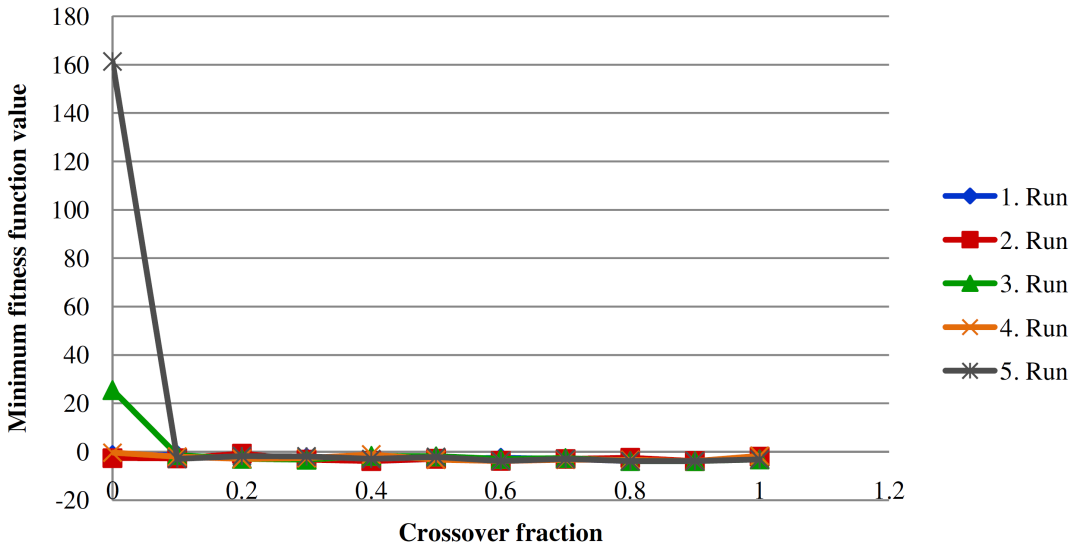

Figure D.1: Mutation rate of 0.9

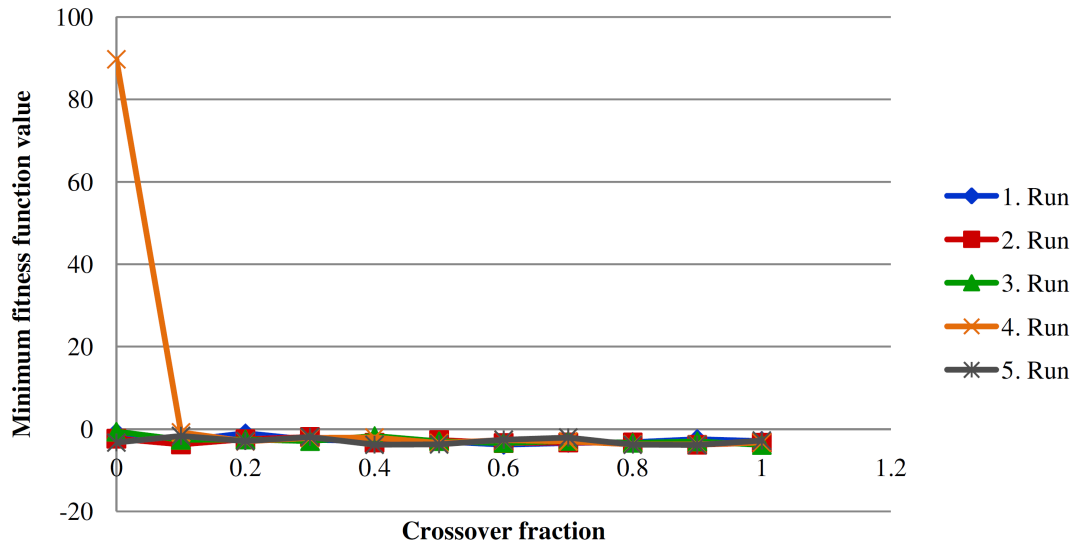

Figure D.2: Mutation rate of 0.7

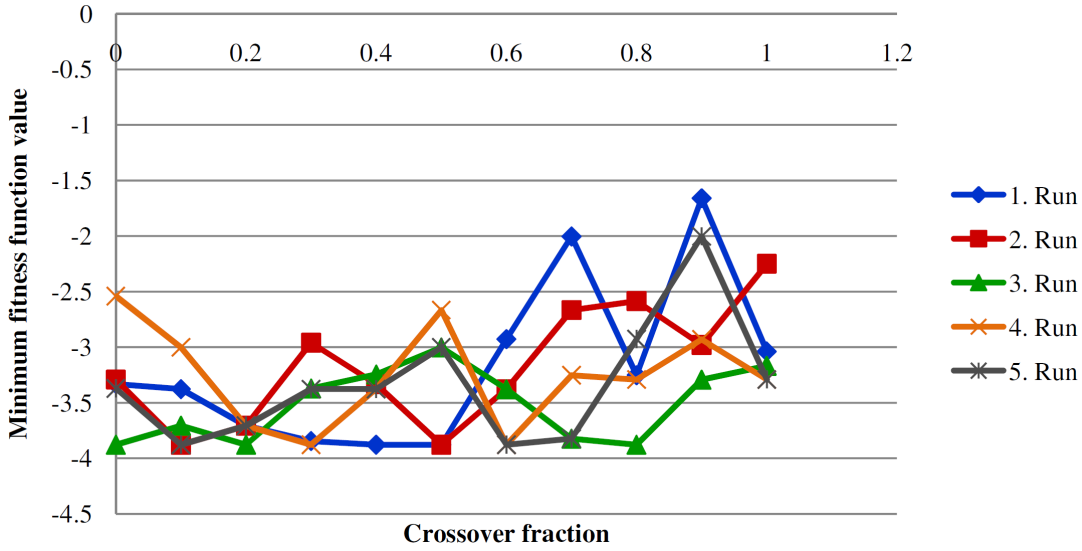

Figure D.3: Mutation rate of 0.3

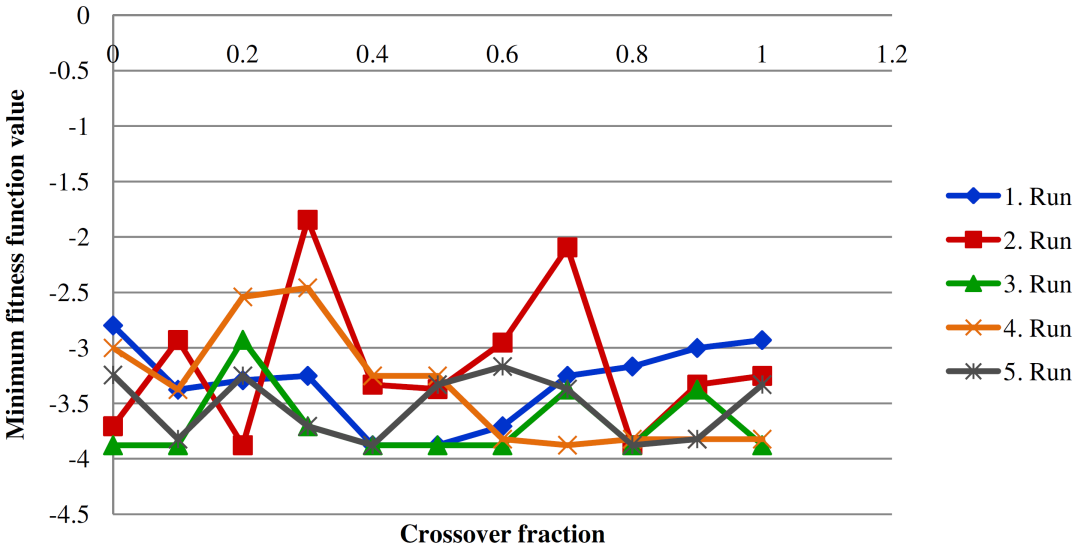

Figure D.4: Mutation rate of 0.1

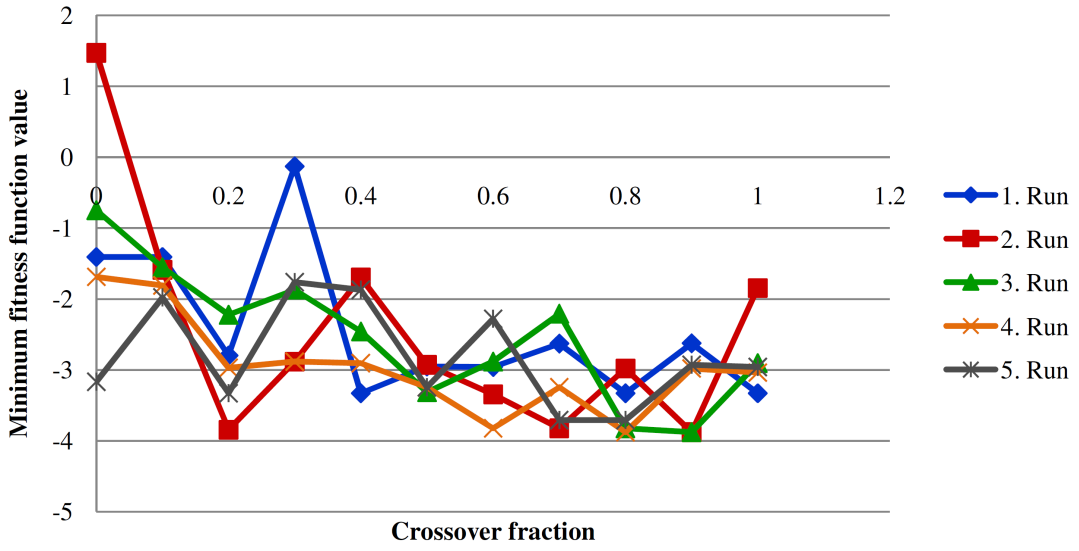

Figure D.5: Mutation rate of 0.9-0.7

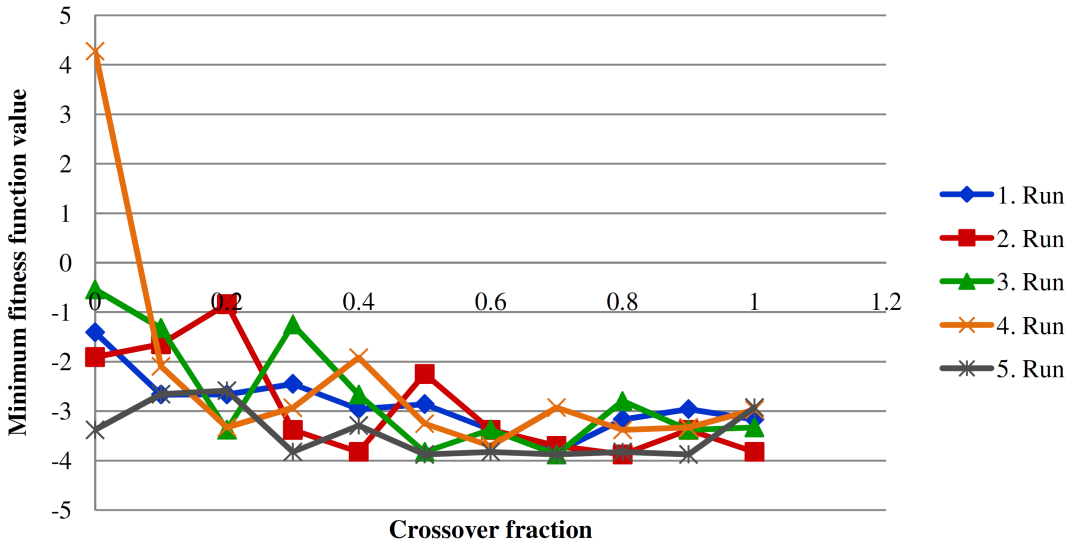

Figure D.6: Mutation rate of 0.9-0.5

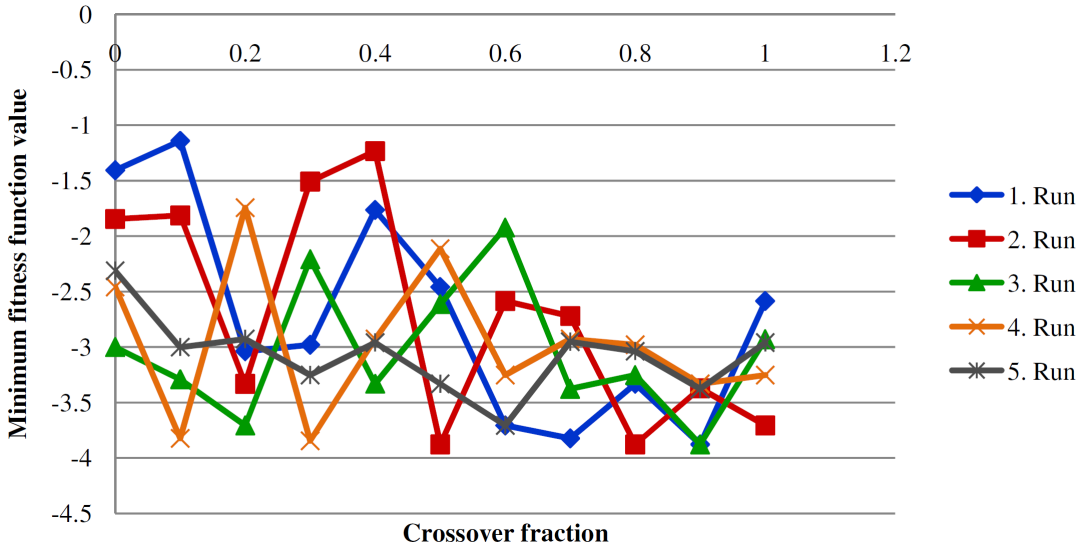

Figure D.7: Mutation rate of 0.9-0.3

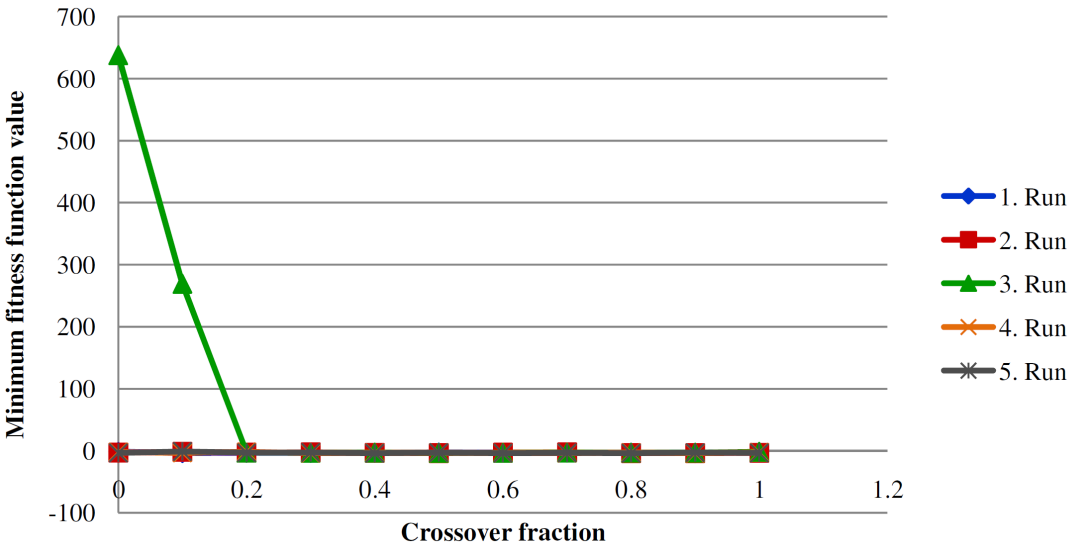

Figure D.8: Mutation rate of 0.9-0.1

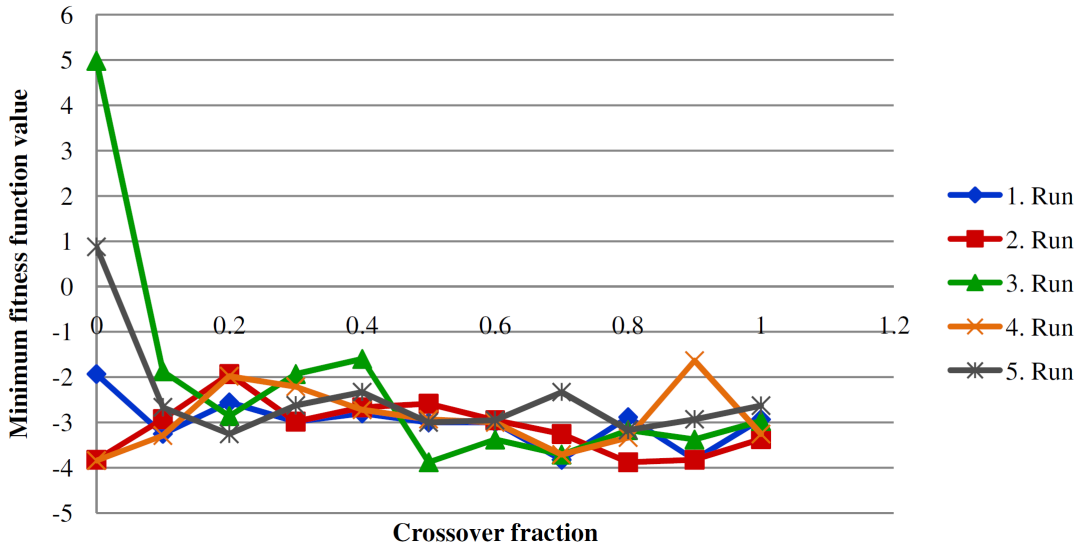

Figure D.9: Mutation rate of 0.7-0.5

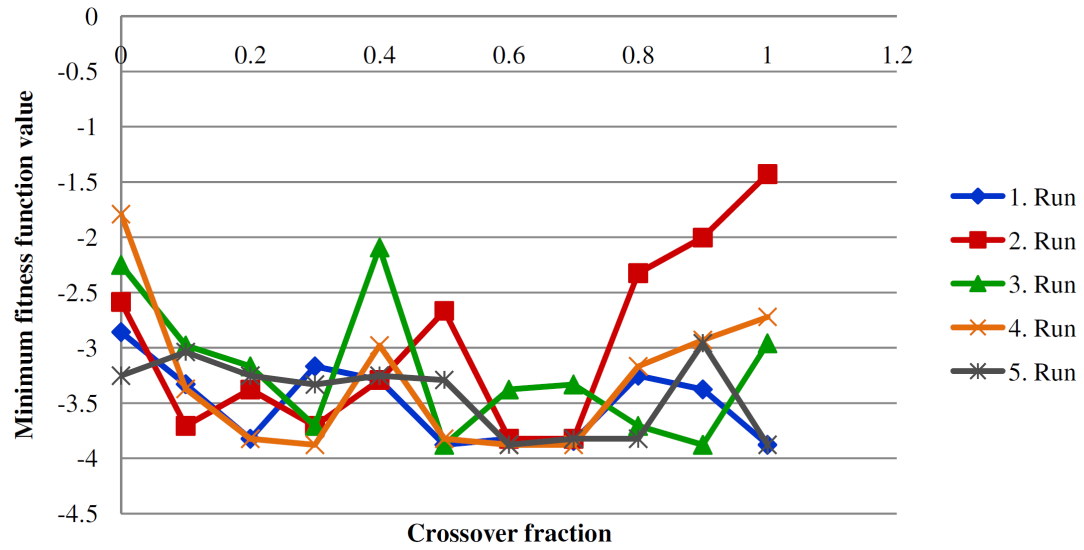

Figure D.10: Mutation rate of 0.5-0.3

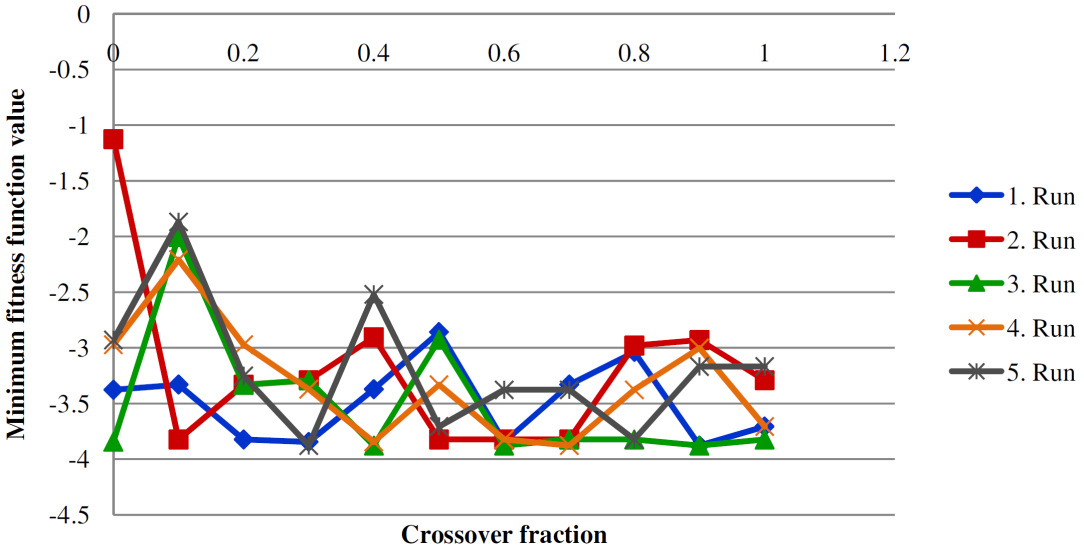

Figure D.11: Mutation rate of 0.5-0.1

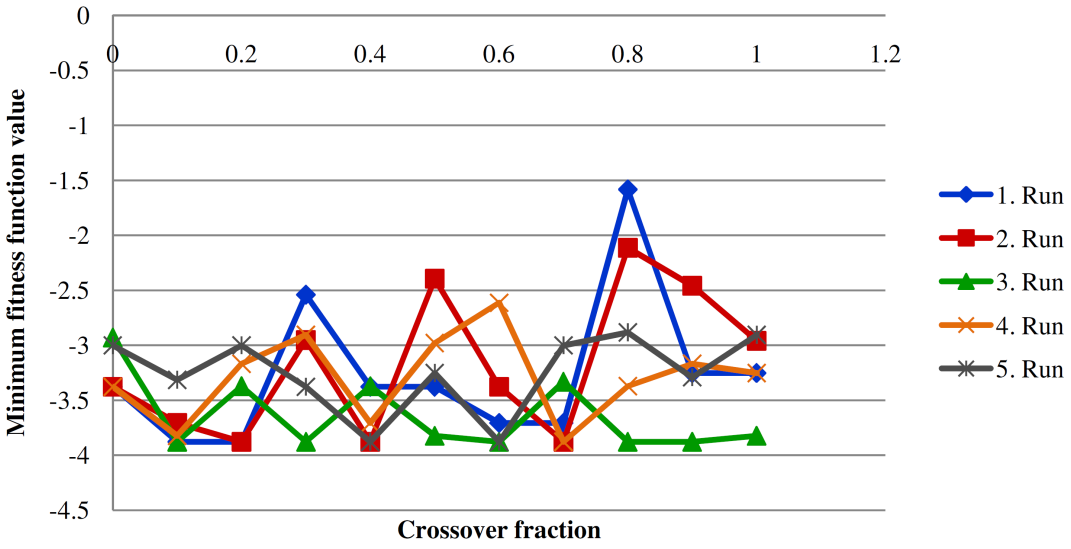

Figure D.12: Mutation rate of 0.3-0.1

Appendix E

Parameter Study - Strain due to Torque and Bending Moment

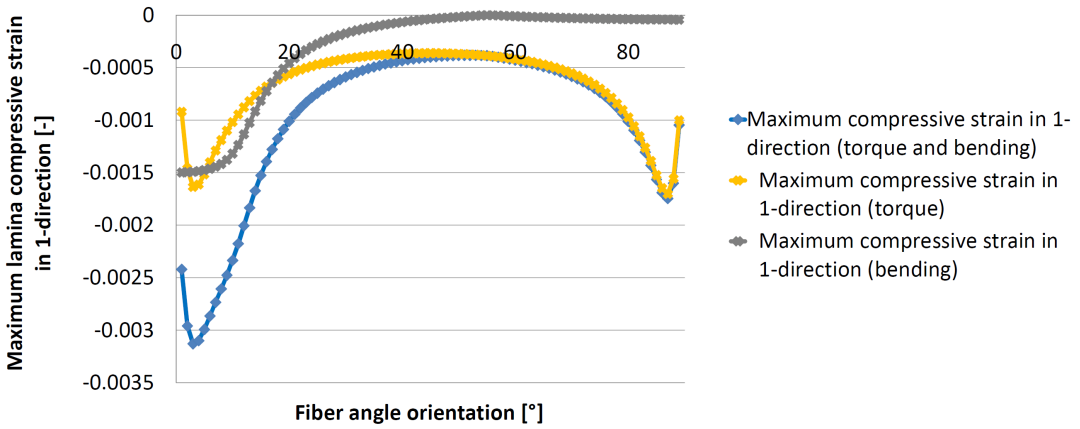

Figure E.1: Parameter study: maximum lamina compressive strain in 1-direction vs. angle of fibers in angle-ply shafts - torque and bending

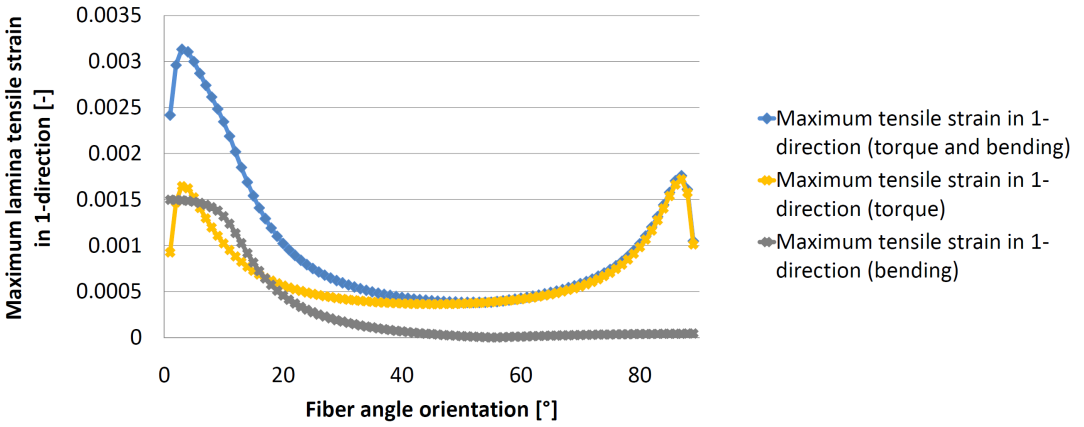

Figure E.2: Parameter study: maximum lamina tensile strain in 1-direction vs. angle of fibers in angle-ply shafts - torque and bending

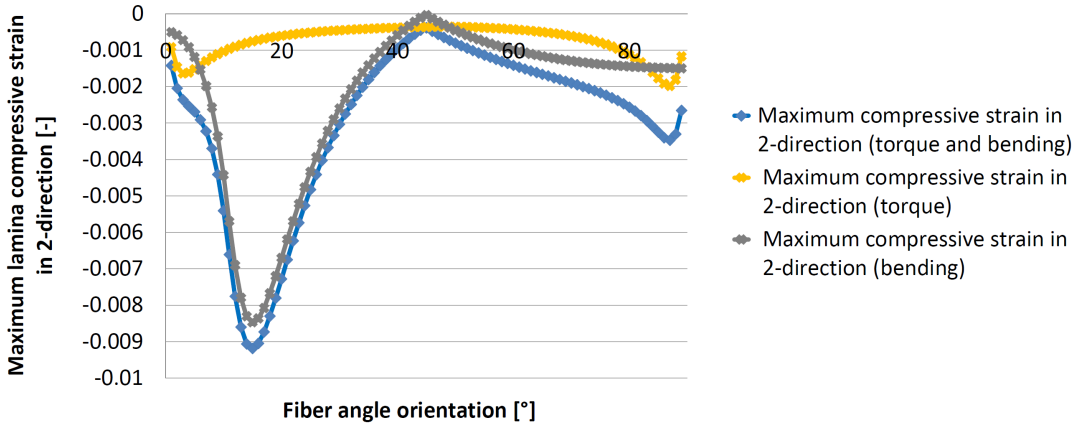

Figure E.3: Parameter study: maximum lamina compressive strain in 2-direction vs. angle of fibers in angle-ply shafts - torque and bending

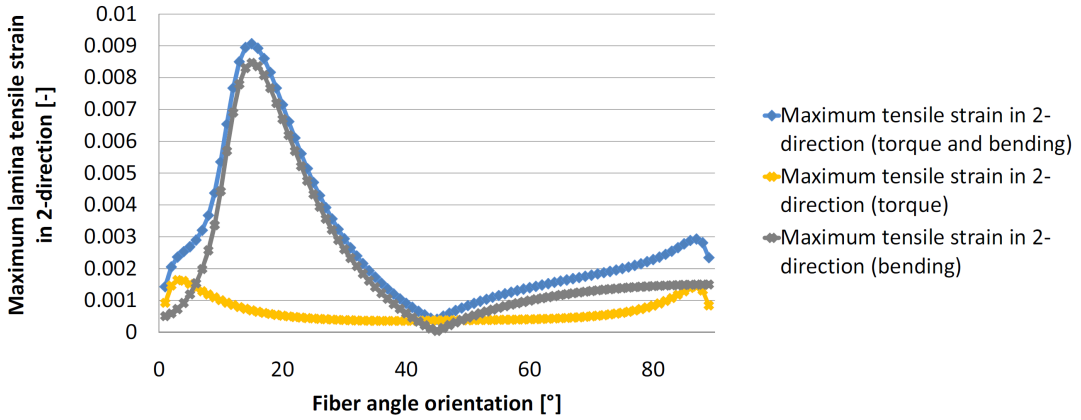

Figure E.4: Parameter study: maximum lamina tensile strain in 2-direction vs. angle of fibers in angle-ply shafts - torque and bending

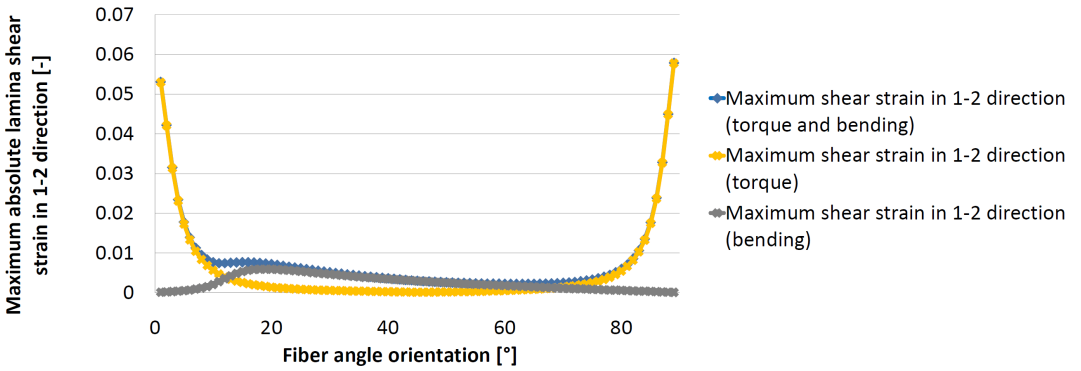

Figure E.5: Parameter study: maximum lamina shear strain in 1-2 direction vs. angle of fibers in angle-ply shafts - torque and bending